# Thermal Modelling of Offshore Floating Photovoltaics

MSc Thesis Project Report

Aryeshah Akbar | 5249198

Delft University of Technology

TU Delft

# Thermal Modelling of Offshore Floating Photovoltaics

## MSc Thesis Project Report

by

Aryeshah Akbar | 5249198

—

| | |
|---|---|
| Main Supervisor: | Dr.ir. Rudi Santbergen |
| Daily Supervisor: | Sathya S. Vasuki |
| Project Duration: | November, 2024 - July, 2025 |
| Faculty: | Faculty of Electrical Engineering Mathematics and Computer Science, TU Delft |

TU Delft

# Preface

This thesis report is submitted in fulfillment of the requirements for the degree of Master of Science in Sustainable Energy Technology at Delft University of Technology. The research presented in this report explores the thermal modelling and energy yield analysis of floating PV systems, aiming to improve PV module temperature prediction accuracy and its impact on energy yield simulation.

This work represents both the academic knowledge gained as well as the technical and personal growth experienced over the course of this research. Throughout this journey, I have encountered many challenges, both conceptual and practical, which have deepened my understanding of PV sytems and energy modelling, particularly in the context of floating solar technologies.

I would like to express my sincere gratitude to my daily supervisor, Sathya, for the continuous guidance throughout the research process. I am also thankful to Dr. Rudi Santbergen for the valuable discussions and constructive feedback in overseeing the progress of this project. Their support has been instrumental in shaping this thesis research works.

This research would not have been possible without the learning environment provided by TU Delft's PVMD Group, as well as the encouraging learning atmosphere among my peers and fellow students. With limited experimental data, I would also extent my thanks to the authors of all the reference study used as the foundation for thermal model validations, as well as the developers of PVMD Toolbox, ANSYS Fluent, and PVsyst, which served as core simulation tools in this study.

On a personal note, I am grateful for my family and partner, whose unwavering support and understanding have kept me grounded throughout this demanding period. In addition, I am also thanking myself to have pushed through and stay true to my goals. These encouragement reminded me on why I traveled halfway across the globe on this academic pursuit in the first place.

I hope that the findings in this thesis contribute meaningfully to the ongoing development of a more reliable and efficient PV system design and simulation methods. Furthermore, I hope it serves as a useful reference for future students and researchers who share an interest in advancing the sustainable energy transition for the better future of our dear (and only) planet.

*Aryeshah Akbar | 5249198*
*Delft, July 2025*

# Summary

Floating Photovoltaic (PV) system is an emerging and rapidly developing solar PV application that utilizes water surfaces, such as reservoirs and lakes, as the installation grounds for the PV arrays and its balance of systems. In addition to becoming a solution to land scarcity issues of solar PV installation, floating PV systems also benefit from an improved thermal performance due to its proximity to water that results in a cooling effect for the PV modules. Consequently, this cooling effect causes the PV module temperature to drop and leads to a higher electrical performance. However, the extent of this cooling effect is not yet well-understood and established. Conventional thermal modelling tools and approaches, which are mostly validated for land-based PV systems, might not be directly applicable to floating PV systems without proper adaptation.

The unique heat transfer characteristics in floating PV systems, especially the influence of water-induced cooling and different convective heat transfer interactions, require a specific thermal models to accurately simulate PV module temperatures. These thermal behaviours, directly affect the electrical performance and energy yield estimation of floating PV systems. Existing PV system energy yield simulation tools such as PVsyst and PVMD Toolbox rely on their respective default thermal assumptions developed for land-based PV, motivating the need for a more floating PV-specific thermal modelling frameworks.

This research aims to improve the accuracy of temperature and energy yield predictions for floating PV systems by evaluating and updating physics-based thermal models based using both analytical and computational methods. This study is driven by several research questions, which includes the analysis on how do existing thermal models perform in predicting floating PV module temperatures, how can Computational Fluid Dynamics (CFD) simulations be used to improve thermal models accuracy for floating PV applications, how does the improvement in thermal model accuracy impact energy yield estimation in PV system energy yield simulation tools, and how does practical installation scenario, specifically differing PV array row spacing, affect the thermal dynamics of floating PV systems. The report is structured systematically that each research question is addressed by each consequent chapters.

Chapter 2 aims to address the first research question. In this chapter evaluation of two analytical thermal modelling approaches for predicting floating PV module temperature is conducted. These thermal models are the existing Fuentes Thermal Model and the newly-developed Resistive Thermal Model. The models are first applied to a land-based PV configuration and then implemented for a floating PV setup. Their accuracy are assessed using measured temperature data from a reference floating PV installation. Results show that while the Fuentes Fluid Dynamics could predict land-based PV module temperatures with reasonably good accuracy, it exhibited significant deviations relative to the measured PV module temperature values when applied to floating PV systems. Resistive Thermal Model has been successfully developed for diverse floating PV configurations, namely Horizontal Pontoon with Truss (HPOT), Horizontal Pipe with Truss (HPIT), and Membrane Ring floating PV. The results of the newly-developed Resistive Thermal Model shows a notable increase in accuracy compared with the Fuentes Thermal Model, shown by the relatively lower root mean square error (RMSE) value calculated relative to the measured PV module temperatures across all assessed floating PV configurations.

Chapter 3 focuses on addressing the second research question. This chapter implements CFD as a refinement tool for the analytical thermal modelling, with the goal of combining CFD's ability to capture detailed solid-fluid interactions and the computational cost effectiveness of the Resistive Thermal Model. The CFD simulation setup using ANSYS Fluent has been successfully validated. These validated model that are used include the energy model, turbulence model, as well as the thermal boundary layer for air-water interface. The findings revealed that by incorporating the updated Nu values specific to floating PV application into the Resistive Thermal Model, the thermal model's accuracy can significantly be improved. The PV module temperature prediction accuracy is quantified by the RMSE value for

the CFD-Updated Resistive Thermal Model of $0.72^oC$, which shows significant improvement from the initial Resistive Thermal Model RMSE for the base case study of $1.70^oC$. This approach answers the second research question, showing that integrating the insights of CFD into analytical approach, in this case the Resistive Thermal Model results in a further improvement in PV module temperature prediction accuracy. This method effectively combines the computational-cost effectiveness of the Resistive Thermal Model and the robustness of computational fluid dynamics approaches.

Chapter 4 aims to address the third research question. This chapter analyzes how the improved thermal models affect energy yield prediction by using two simulation tools, namely PVsyst and the PVMD Toolbox. The energy yield results show that the CFD-updated Resistive Thermal Model achieves the closest match to the measured specific energy yield, with an error of just 0.10%, compared to 1.75% and 1.27% for the Fuentes FD Model and the initial Resistive Thermal Model, respectively. These findings are further reinforced by the results from energy yield simulation using PVMD Toolbox, that re-affirms that the CFD-Updated Resistive Thermal Model shows an significant increase in energy yield prediction accuracy, compared to Fuentes Thermal Model and the Initial Resistive Thermal Model. These results clearly show that the increase in thermal model accuracy is directly related to a higher accuracy in energy yield simulation, where the energy yield simulation based on the improved thermal model results in a very close agreement with measured values.

Chapter 5 focuses on addressing the fourth research question. This chapter analyzes how does practical installation scenario, specifically differing PV array row spacing, affect the thermal dynamics of floating PV systems. From the the base case study of 1 meter row-spacing, it is revealed that PV modules in Row 1 exhibit the lowest average temperature (around 25.8 to $25.9^oC$), while modules in Row 3 show the highest temperatures (up to $26.5^oC$). varying the row spacing to 1.5 meter and 0.5 meter revealed that when the row spacing is increased to 1.5 meters, the temperature of Row 2 is nearly the same as Row 1, indicating strong wind penetration and effective convective heat dissipation. In contrast, reducing the spacing to 0.5 meters leads to a substantial rise in temperature for both Row 2 and Row 3. These findings indicate that tighter spacing restricts airflow between rows, resulting in decreased convective cooling and higher operational temperatures for downstream modules. In conclusion, the results demonstrate that while close-proximity PV arrays with small row-spacing may offer higher power density per unit area, it comes at the cost of increased PV module temperatures and potentially reduced energy yield. On the contrary, large-proximity PV arrays with large row-spacing results in a lower overall PV module temperatures that potentially increase energy yield of the floating PV system.

Overall, this study successfully addresses the main research objective, which is to develop, validate, and apply improved thermal models that accurately capture the temperature behaviour of floating PV systems in comparison to land-based PV systems, thereby enabling more accurate energy yield simulations. The integration of CFD-derived parameters into Resistive Thermal Model leads to significantly improved accuracy in temperature and energy yield predictions. However, the findings are based on limited real-world measurement data and a single floating PV archetype. A more extensive validation across more configurations and climates, as well as the development of generalized Nusselt number correlations are recommended for future works.

# Contents

# Nomenclature

## Abbreviations

| Abbreviation | Definition |
|---|---|
| ANSYS | Analysis System Software |
| BIPV | Building-Integrated Photovoltaics |
| CFD | Computational Fluid Dynamics |
| FPV | Floating Photovoltaics |
| GMPV | Ground-Mounted Photovoltaics |
| ISA | International Standard Atmosphere |
| LCOE | Levelized Cost of Electricity |
| MAE | Mean Absolute Error |
| NOCT | Nominal Operating Cell Temperature |
| POA | Plane-of-Array |
| PV | Photovoltaic |
| PVMD | Photovoltaic Module Design (Toolbox at TU Delft) |
| RMSE | Root Mean Square Error |
| RTPV | Rooftop Photovoltaics |

## Symbols

| Symbol | Definition | Unit |
|---|---|---|
| $T_{mod}$ | PV module temperature | [°C] |
| $T_{amb}$ | Ambient temperature | [°C] |
| $T_{sky}$ | Sky temperature | [K] |
| $T_{gr}$ | Ground or water temperature | [K] |
| $T_{dew}$ | Dew point temperature | [°C] |
| $T_F$ | Front surface temperature (resistive model) | [K] |
| $T_B$ | Back surface temperature (resistive model) | [K] |
| $G_{POA}$ | Plane-of-array irradiance | [W/m²] |
| $Q_{in}$ | Absorbed irradiance power | [W] |
| $Q_{conv}$ | Convective heat loss | [W] |
| $Q_{rad}$ | Radiative heat loss | [W] |
| $Q_{cond}$ | Conductive heat transfer | [W] |
| $h$ | Convective heat transfer coefficient | [W/m²·K] |
| $U_0$, $U_1$ | Thermal loss coefficients in Faiman model | [W/m²·K] |
| $\epsilon$ | Emissivity | [-] |
| $\sigma$ | Stefan-Boltzmann constant | [W/m²·K□] |
| $\alpha$ | Absorptivity of PV module | [-] |
| $\eta$ | PV module efficiency | [-] |
| $\rho$ | Density of air or water | [kg/m³] |
| $c_p$ | Specific heat capacity | [J/kg·K] |
| $v$, $WS$ | Wind speed | [m/s] |
| $\lambda$ | Thermal conductivity | [W/m·K] |
| $\phi$ | View factor | [-] |
| $Nu$ | Nusselt number | [-] |
| $Re$ | Reynolds number | [-] |

| Symbol | Definition | Unit |
|---|---|---|
| $Pr$ | Prandtl number | [-] |
| $\theta_z$ | Solar zenith angle | [rad] |
| $\Delta T$ | Temperature difference | [K] |

# 1

# Introduction

## 1.1. Background

Solar photovoltaic (PV) systems have become one of the fastest-growing sustainable energy technologies worldwide, driven by policy support, declining costs and technological improvements [1]. In 2023, at the COP28 conference, the Intergovernmental Panel on Climate Change (IPCC) proposed a target for all member countries to reach Net-Zero Emissions (NZE) goal in 2030, in which it is imperative to increase the capacity of renewable energy sources (RES) from 4.7 TW in 2024 to approximately 11 TW by 2030 as shown in figure 1.1 [2]. This ambitious target has become a catalyst for governments to introduce supporting policies, such as subsidies, tax incentives, and renewable energy mandates, which have played a crucial role in accelerating the deployment and advancement of solar PV technologies.

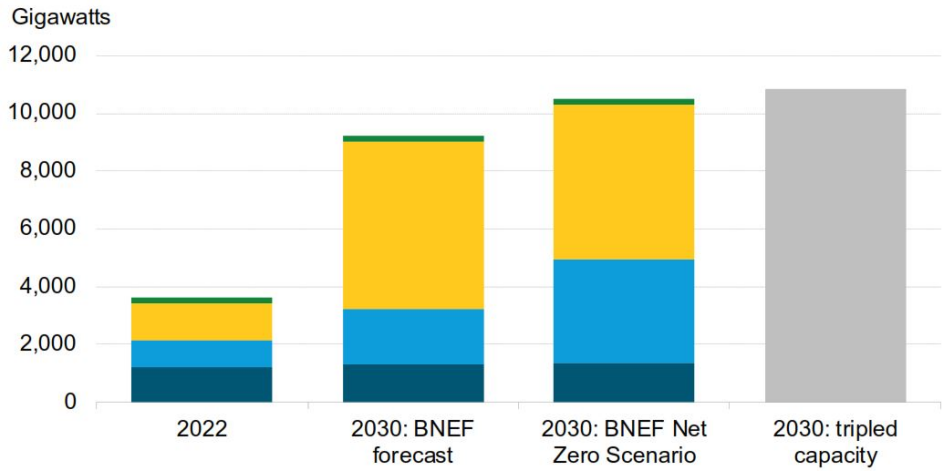


**Figure 1.1:** Renewable Energy Sources targets as proposed by BNEF in accordance with IPCC during COP28

As a result of these supportive policies, the solar PV industry has experienced rapid growth, further supported by significant declines in the costs of both PV modules and system installations. Between 2010 and 2022, the global weighted average levelized cost of electricity (LCOE) from utility-scale solar PV projects fell by 89%, from USD 0.417/kWh to USD 0.048/kWh, making solar PV one of the most cost-competitive sources of electricity [3]. The key factor that influences this cost reduction, in fact, is the advancements in the solar PV technology itself. Innovations in solar cell efficiency and manufacturing processes have contributed to this expansion, with the average efficiency of commercially available solar modules rising from 1% to over 22% during the period of 2010 to 2022 [4].

In line with these advancements, solar PV systems have diversified in their applications and installation methods, allowing them to be implemented in various configurations to maximize land use efficiency. Solar PV systems typically categorized based on their installation location, and generally classified into

ground-mounted PV (GMPV), rooftop PV (RTPV), and building-integrated PV (BIPV). The most basic and widely adopted type is GMPV, where PV modules are installed directly on the ground, often in expansive arrays. However, GMPV installations are land-intensive, requiring large amount of unshaded areas, which can limit their feasibility in regions where land is scarce or costly [5]. Studies have shown that a typical utility-scale solar PV project with a capacity of 100 MW requires a land area of 1 – 3 $km^2$ [6]. If we refer back to the NZE targets, this implies that in 2030, the total land area required for solar farm is approximately 0.18 million $km^2$.

While the Earth's total land area is approximately 148 million $km^2$ [7], the amount of land suitable for solar PV deployment is estimated to be a small percentage of that land area. Study suggests that around 1.47% to 2.04% of the Earth's land surface is potentially suitable for solar PV development, depending on factors like solar irradiance slope, and land-use restrictions [8], this translates to roughly 2.17 to 3.02 million $km^2$ being suitable for solar installations. However, actual deployment could be even lower due to competing land uses such as agriculture and urbanization, leading to an uncertainty for both now and in the future. This constraint is particularly significant in densely populated or land-scarce regions, where large bodies of land are either unavailable or too costly for solar farm development.

To address this limitation, RTPV and BIPV systems have been developed to maximize PV deployment without occupying additional land area. RTPV involves installing PV module on building rooftops, while BIPV integrates PV materials directly into the structural elements of buildings, such as facades and windows, allowing urban and rural areas to harness solar energy without occupying open land [9]. Although RTPV and BIPV have alleviated some land-use constraints, these alternatives alone may not be sufficient to address the land-intensive nature of PV installations, especially in densely populated areas. Floating PV (FPV), in which the PV modules are installed on bodies of water such as reservoirs, lakes, and even oceans, presents a promising solution to this challenge without putting additional pressure on valuable land resources. From the previously mentioned IPCC projection, over the next six years (2024 – 2030), FPV installations are expected to reach a maximum of 30 GW, accounting for 0.5% of the target total solar energy capacity of 6 TW. This relatively small percentage implies that while floating PV holds significant promise as a solution to land-use constraints, a more thorough, comprehensive, and in-depth research approach is essential to understand and optimize floating PV's unique technological advantages. In sub-chapter 1.2, a literature review is carried out to delve into more details on the theoretical and practical landscape of the research, development, and implementation of floating PV technologies.

## 1.2. Literature Review

Floating PV systems are an innovative approach to solar energy generation, utilizing water bodies such as lakes, reservoirs, and offshore areas to install photovoltaic modules. As illustrated in the figure 1.2, a typical floating PV system consists of PV modules mounted on bouyant platforms, which are stabilized using mooring and anchoring systems to withstand environmental forces such as wind and water currents. The generated electricity is collected through a combiner box and converted from DC to AC via a central inverter, before being fed into the grid through a transformer and transmission lines. Additionally, a lightning protection system is integrated by grounding the metal frames of the modules, ensuring system safety. Floating PV offers several advantages over traditional land-based solar farms, including optimized land use, reduced water evaporation, and potential improvements in energy yield due to the cooling effect of water.

Among these advantages, the cooling effect is particularly significant compared to land-based option, as it can reduce module temperatures and improve efficiency, leading to higher energy yields. However, the extent and mechanisms of this cooling effect vary depending on factors such as water temperature, wind speed, and system design, making it a crucial area of research. A deeper understanding of thermal behavior in floating PV systems is essential for optimizing performance, refining energy yield predictions, and ensuring long-term system reliability. Exploring this cooling effect further would enable PV design engineers to implement a better design strategies that maximize the benefits of floating PV, making it a more competitive and sustainable solar energy solution.

In existing scientific literature, FPV is often reported to have superior performance compared to land-based PV [10]. The typical explanation for the enhanced performance is that water cooling reduces

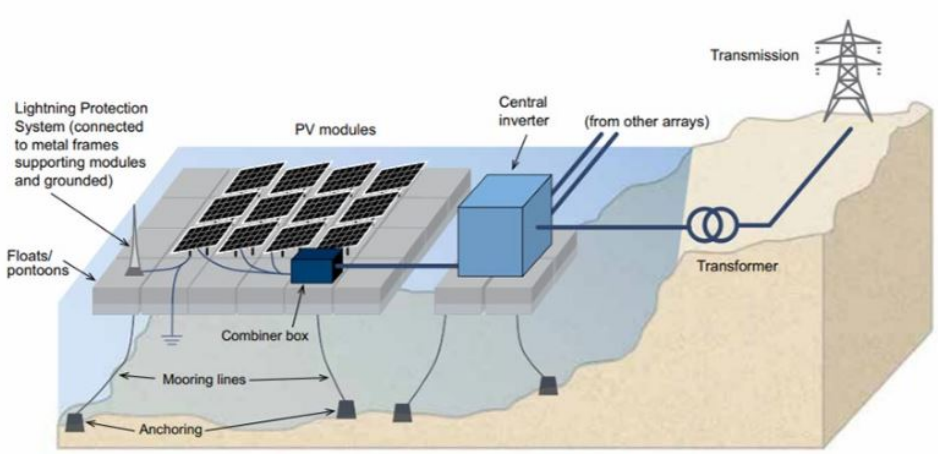


**Figure 1.2:** Schematic representation of a typical large scale floating PV system's key components

the cell operating temperature and therefore increases the efficiency of the PV modules. It has been observed that the power output of a PV module reduces by almost 0.4% - 0.5% for every 1oC cell temperature increase [11]. Furthermore, Liu et al. [12] demonstrated that the cooling effect of water on PV systems results in an approximately 3.5°C difference in operating temperature between an FPV system and a GMPV system. This temperature reduction is critical because, as mentioned, PV efficiency decreases with increasing module temperature. Thus, FPV's lower operating temperature directly translates to improved efficiency and energy output in most climates [13]. Further research indicates that FPV systems consistently show higher energy yields per installed capacity than GMPV systems in various environmental conditions. A study by Trapani and Santafé [14] evaluated FPV systems across several climates and found that FPV outperformed GMPV by 5% to 10% in annual energy yield, primarily due to the reduced temperature and the higher reflectivity of water surfaces. The water surface not only cools the system but also minimizes dust accumulation on the panels, thereby reducing cleaning costs and maintaining optimal energy output for extended periods [15]. Building on these performance comparisons, it becomes essential to model the thermal dynamics unique to FPV systems, as temperature management significantly influences energy output and system efficiency.

Modelling thermal behaviour for PV systems can be approached through various methods, with empirical modelling and physics-based analytical modelling being two widely applied methods. Empirical modelling is based on observed data and statistical relationships, providing straightforward temperature predictions through regression analysis or simplified equations derived from real-world measurements. This method is valuable for its ease of implementation and relatively low computational requirements. One of the foundational empirical models is the Nominal Operating Cell Temperature (NOCT) model, which estimates PV module temperature based on ambient temperature, irradiance, and wind speed [16]. The NOCT model, often employed in land-based PV systems, simplifies thermal behaviour through a single equation, depicted in equation (1.1), enabling a relatively easy integration into PV performance simulations.

$$T_m = T_{\text{amb}} + \frac{G_{\text{AOI}}}{G_{\text{NOCT}}} (\text{NOCT} - 20^\circ C) \tag{1.1}$$

The value of NOCT is dependent on the distance between the PV module and the base of where the PV module is mounted. However, while widely adopted, the model has limitations in accuracy, as it may not fully capture the effects of rapidly changing environmental factors, particularly in regions with extreme or variable weather [17]. To address these limitations, more refined empirical models have been developed. For instance, Duffie and Beckman [18] proposed an enhanced empirical model that incorporates additional parameters, such as convective heat transfer coefficients due to the presence of wind (WS), as depicted in equation (1.2).

$$T_m = T_{\text{amb}} + \frac{G_{\text{AOI}}}{G_{\text{NOCT}}} (\text{NOCT} - 20°C) \cdot \frac{9.5}{5.7 + 3.8 \cdot WS} \left(1 - \frac{\eta_{\text{STC}}}{\tau\alpha}\right) \tag{1.2}$$

This model better accounts for localized weather variations, in this instance, wind, which can have significant impacts on module temperature, especially in high-temperature climates where PV efficiency losses are predominantly affected by heat.

The Sandia model [19], developed by Sandia National Laboratories, and is widely adopted as an empirical approach for estimating PV module temperatures under various environmental conditions. This model incorporates irradiance corrected for the angle of incidence ($G_{AOI}$), and two empirical coefficients, a and b, which are specific to different module and mounting types. The Sandia model is represented by equation (1.3).

$$T_m = T_{\text{amb}} + G_{\text{AOI}} \cdot \exp(a + b \cdot w) \tag{1.3}$$

The inclusion of these coefficients allows the model to more accurately reflect real-world performance across various conditions, such as whether the module is installed on an open rack or insulated back. For example, an open rack installation typically has higher convective cooling, which is reflected in the more negative values of a and higher wind sensitivity b.

In addition to the Sandia model, another widely used empirical thermal model used in PV system temperature predictions is the Faiman model. The Faiman model simplifies the process by relying on fewer parameters, focusing more on ambient temperature and solar irradiance [20]. The Faiman model is represented by equation (1.4).

$$T_m = T_{\text{amb}} + \frac{G_{\text{AOI}}}{U_0 + U_1 \cdot WS} \tag{1.4}$$

U0 and U1 are empirical constants that account for heat loss. U0 represents heat loss due to natural convection and radiation, while U1 accounts for the effect of forced convection (primarily influenced by wind speed). These U-values provide a measure of how effectively the heat absorbed by the cell is dissipated. High U-values indicate a high level of heat exchange between PV cell and the ambient, resulting in lower operating module temperature. Similar to the Sandia model, these values are indirectly influenced by the type of mounting structure configuration. This model is applied in commercial-standard PV system energy yield simulation tool PVsyst.

To accurately utilize Sandia model, the U-values used in the model needs to be investigated, and numerous studies have been done to gather site-specific measured data in recent years. In these studies, the empirical correlation for PV module temperature is yielded through collecting the environmental data such as irradiance, ambient temperature, wind speed, and humidity and then using linear regression method to derive the corresponding empirical correlation.

Dorenkamper et al. [21] conducted an empirical study to quantify the cooling effect of floating PV systems by comparing the thermal behaviour with that of land-based and rooftop PV installations in two different climate zones, which are temperate and tropical. In this study, the U-values are defined as a function of incident irradiance, front glass absorptivity, PV module electrical efficiency, and temperature difference between the PV module and the ambient. In line with the Sandia model, the U-values were decomposed to constant and wind-dependent component. Ultimately, the derived U-values were used as input in PVsyst simulation to predict the energy yield, where a 6% increase is observed for floating PV systems compared to land-based system.

Kjeldstad et al. [22] studied the empirical thermal correlation for a floating PV systems in direct contact with water via a floating membrane, comparing it to air-cooled floating PV systems. The study finds that the water-cooled configuration achieved a higher U-values at approximately 80 W/$m^2$K and delivered a 7% higher energy yield. Furthermore, the study also emphasized the importance of incorporating water temperature, in addition to air temperature into U-values calculation for floating PV systems with direct water contact. The validation that has been done in this study suggests that PV module temperature

is more accurately predicted when water temperature, in addition to air temperature is considered, highlighting an important limitation in the Sandia model.

N. Elminshawy et al. [23] investigated the thermal behaviour of FPV systems using both experimental and computational approaches. Their study involved direct measurements of module temperature under varying environmental conditions. A significant contribution of their research was the development of regression equations that predict module temperature, providing a reliable empirical tool for evaluating the thermal performance of floating PV systems. The findings indicated that FPV systems benefit from the cooling effects of water, resulting in lower operating temperatures compared to traditional ground mounted PV systems.

While empirical models provide practical and relatively simple approaches to estimating PV module temperatures, they rely on predefined empirical coefficients and generalized assumptions, which are usually location-specific, and may not always reflect the dynamic nature of real-world conditions, particularly in systems with non-standard configurations such as floating PV. Moreover, they did not give insight into the underlying heat transfer mechanisms or how specific floating PV configuration affects the thermal behaviour. To address these limitations, several fluid dynamics-based analytical thermal models have been developed.

Analytical thermal models offer a structured and physics-based approach to understanding the temperature dynamics in PV systems. These models are essential for calculating the heat balance and predicting the module temperature based on interactions between environmental factors and heat transfer mechanisms. Unlike empirical models, analytical models rely on fundamental heat transfer principles, providing a more consistent and detailed understanding of the internal and external thermal processes within PV systems. One of the most established and widely used analytical model is the fluid dynamics model.

The analytical fluid dynamics model [24] is based on a steady-state energy balance between the PV module and its surrounding environment. This model accounts for absorbed irradiance, convective heat loss to ambient air, and radiative exchange with the sky and ground. Developed as an extension of the work by Fuentes et al. [25], it has been adopted in PV system simulations due to its physical interpretability and computational efficiency. Notably, this analytical fluid dynamics model is implemented in the PVMD toolbox developed at Delft University of Technology, making it a standard choice for simulating module temperature in academic and research-based energy yield assessments.

The existing literature on analytical thermal modelling for PV systems shows advancements in understanding and predicting PV module temperature under various environmental conditions. However, most of these studies have been developed and validated primarily for land-based PV systems such as ground-mounted and rooftop installations. Floating PV systems, on the other hand, has different convective and radiative cooling characteristics due to its proximity to water and typically lower ambient temperatures, and have not yet received a thorough thermal modelling efforts. While studies such as those by Liu et al. and Elminshawy et al. emphasize the cooling benefit of water in floating PV applications, few have directly compared the thermal behaviour of floating PV modules against land-based systems using consistent modelling approaches. This lack of comparative insight limits our ability to generalize thermal model accuracy across installation types and assess the extent of the cooling effect offered by floating PV.

Moreover, although empirical models, as the few mentioned previously, offer valuable data-driven estimates of PV module temperature and U-values, they often lack the physical approach to capture heat transfer effects or simulate performance under untested environmental conditions. To address this, analytical approaches, such as resistive thermal model, can provide a more robust and generalizable framework. Furthermore, limited work has been done to evaluate and update these models specifically for floating PV applications using numerical techniques such as computational fluid dynamics (CFD). CFD offers the capability to simulate detailed solid-fluid interactions and thermal flows, which are especially relevant in floating PV context where water cooling and flow dynamics differ significantly from land-based PV systems.

Lastly, there is a notable gap in research linking thermal modelling outcomes directly to energy yield simulations and optimization efforts. While Alharbi et al. [26] underscored the importance of thermal management for PV efficiency, studies generally fall short of conducting comprehensive energy yield

simulations that incorporate thermal modelling results. Without this integration, it is challenging to understand how temperature reductions achieved through optimized FPV designs affect long-term energy yield and economic viability. Addressing this gap could enable the development of FPV-specific energy yield optimization strategies that leverage thermal model outputs. This study aims to address these gaps by systematically comparing thermal modelling approaches between land-based and floating PV systems, validating and updating them through CFD, and assessing the resulting imact on energy yield.

## 1.3. Research Questions and Research Objective

Based on the research gaps identified in the previous sub-chapter, the objective of this thesis research project is **to develop, validate, and apply improved thermal models that accurately capture the temperature behaviour of floating PV systems in comparison to land-based PV systems, thereby enabling more accurate energy yield simulations**.

To achieve this objective, the following three main research questions have been formulated:

1. **How do analytical thermal models perform in predicting PV module temperatures for both floating and land-based PV systems?** This question aims to evaluate the accuracy and limitations of existing thermal models when applied across different deployment types, and to explore potential initial improvements to enhance their predictive performance.
2. **How can analytical thermal models be improved to better represent heat transfer mechanisms specific to floating PV systems?** This question focuses on investigating the role of Computational Fluid Dynamics (CFD) in capturing detailed convective, conductive, and radiative effects influenced by water proximity and ambient cooling.
3. **How does the CFD-Updated Resistive Thermal Model affect the accuracy of energy yield simulations?** This question aims to bridge thermal modelling with practical energy yield forecasting, allowing for a more insightful comparison of the advantages offered by floating PV deployment.
4. **How does practical installation scenario, specifically differing PV array row spacing, affect the thermal dynamics of floating PV systems?** This question extends the CFD study that was done to represent a more practical floating PV scenario with multiple-module PV array, focusing on the effect of row spacing to PV module temperature distribution.

The following chapters of this thesis are structured to systematically address the research questions and provide a comprehensive evaluation of thermal modeling for floating PV systems in comparison to land-based PV installations. Chapter 2 analyzes analytical thermal models, including the existing Fuentes Model and the newly-developed model in this study, the Resistive Thermal Model, and evaluates their performance in predicting module temperature for both land-based and floating PV systems. The analysis highlights how these models capture the differing thermal behaviors between the two installation types and identifies key influencing parameters such as wind exposure, convective cooling, and proximity to water surfaces. Chapter 3 aims to enhance the Resistive Thermal Model using Computational Fluid Dynamics (CFD) simulations conducted in ANSYS Fluent. This chapter investigates how CFD can improve the accuracy of thermal predictions by simulating detailed convective heat transfer mechanisms, especially those unique to floating PV environments. Chapter 4 integrates the validated thermal models into energy yield simulations using tools such as the PVsyst and PVMD Toolbox. This chapter aims to integrate the results of the updated thermal model into practical energy yield simulation, providing insights into how thermal differences translate into electrical output. Chapter 5 concludes the thesis by summarizing the main findings, reflecting on methodological limitations, and proposing future research directions for enhancing the accuracy and applicability of thermal and energy yield modeling in floating PV systems.

# 2

# Analysis on Analytical Thermal Models Accuracy for Floating PV Module Temperature Prediction

Understanding the thermal behaviour of PV systems is critical for accurately estimating their performance and energy yield. Floating PV, in particular, has different thermal characteristics compared to conventional land-based PV systems due to their exposure to water-induced cooling and different convective conditions. This chapter's objective is to address the first research question, namely to analyse how analytical thermal models perform in predicting PV module temperatures for both floating PV and land-based PV systems. In this chapter, an assessment is done for the existing Fuentes thermal model, which has been widely applied to land-based PV systems, where the model's applicability for both land-based and floating PV configurations is evaluated. The model's accuracy in predicting PV module temperature under varying environmental conditions is assessed through comparisons with measured data.

Next, this chapter introduces and develops an alternative analytical approach named the Resistive Thermal Model, specifically derived to capture the heat transfer dynamics of floating PV systems. The model structure is derived based on an equivalent thermal circuit analogy that incorporates conductive, convective, and radiative heat exchanges. Its performance is also evaluated for both land-based and floating PV systems to assess its predictive accuracy.

Finally, this chapter identifies and analyses the key thermal parameters that influence PV module temperature. A sensitivity analysis is performed to determine the relative impact of these parameters, laying a basis for model improvement and integration into energy yield simulations in the subsequent chapters.

## 2.1. Fuentes Fuentes Thermal Model

### 2.1.1. Introduction to Fuentes Thermal Model

The analytical fluid dynamics model [24] is based on Fuentes Thermal Model [25], where three main heat transfer mechanisms between the PV module and its environment are considered, which are conduction, convection, and radiation, as illustrated in Figure 2.1. This steady-state thermal model is derived from a simplified energy balance approach assuming a uniform module temperature $T_M$, and it forms the basis of temperature estimation in many simulation tools, including TU Delft-developed PV system simulation software, the PVMD Toolbox. Further in this study, this model is referred to as the Fuentes Thermal Model.

To assess the thermal behaviour of the PV system, a basis of energy balance must be established. In the energy balance of PV system in general, the incoming energy is primarily originated from the absorbed solar irradiance by the surface of the PV module. The absorbed energy $Q_{in}$ is given by:

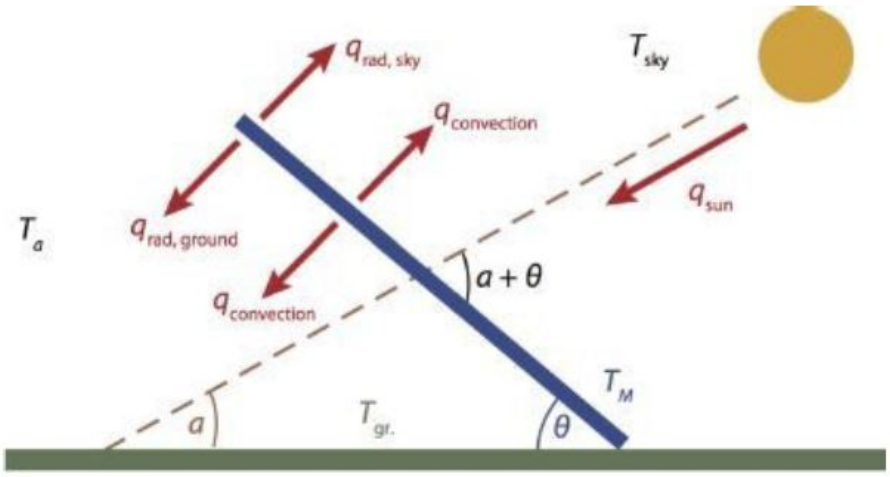


**Figure 2.1:** Heat Transfer Mechanisms Illustration for Fuentes FD Thermal Model

$$Q_{\text{in}} = \alpha G_{\text{POA}}, \tag{2.1}$$

where $\alpha$ is the absorptivity of the module and $G_{\text{POA}}$ is the plane-of-array irradiance. This absorbed energy is partially converted into electrical energy and the remainder is dissipated through thermal losses.

Convective heat loss from both the front and rear surfaces of the module to the ambient air is modeled as:

$$Q_{\text{conv}} = h_{\text{tot}}(T_M - T_a), \tag{2.2}$$

where $T_a$ is the ambient air temperature and $h_{\text{tot}}$ is the total convective heat transfer coefficient (sum of front and back convection coefficients, $h_{\text{front}} + h_{\text{back}}$).

Radiative losses to the sky and the ground are calculated as:

$$Q_{\text{rad,sky}} = \epsilon_{\text{top}}\sigma\left(T_M^4 - T_{\text{sky}}^4\right), \tag{2.3}$$

$$Q_{\text{rad,ground}} = \epsilon_{\text{back}}\sigma\left(T_M^4 - T_{\text{gr}}^4\right), \tag{2.4}$$

where $\epsilon_{\text{top}}$ and $\epsilon_{\text{back}}$ are the emissivities of the front and back surfaces of the module, respectively, and $\sigma$ is the Stefan–Boltzmann constant. The sky temperature $T_{\text{sky}}$ is commonly approximated using:

$$T_{\text{sky}} = T_a \cdot \left(0.711 + 0.0056T_d + 0.000073T_d^2 + 0.013\cos(\theta_z)\right)^{0.25}, \tag{2.5}$$

where $T_d$ is the dew point temperature and $\theta_z$ is the solar zenith angle.

Assuming negligible heat conduction through the mounting structure (due to minimal contact area), the thermal energy balance for the PV module in steady state becomes:

$$mc\frac{dT_M}{dt} = \alpha G_M - h_c(T_M - T_a) - \epsilon_{\text{back}}\sigma\phi\left(T_M^4 - T_{\text{gr}}^4\right) - \epsilon_{\text{top}}\sigma\phi\left(T_M^4 - T_{\text{sky}}^4\right). \tag{2.6}$$

This equation is solved iteratively to determine $T_M$ under given environmental conditions. In the context of floating PV, parameters such as wind speed, water-cooled air layers, and adjusted sky or ground temperatures play a significant role in the accuracy of this model.

### 2.1.2. Implementation of Fuentes Thermal Model for Land-Based PV Systems

Before applying the Fuentes Thermal Model to floating PV systems, it is important to first validate its performance in conventional land-based PV systems, where the model has been widely applied on. This sub-chapter aims to assess the accuracy of the model in two typical land-based scenarios, which are ground mounted PV (GMPV) and rooftop PV (RTPV) installations. These configurations have well established case studies and supported by extensive measurement data, allowing a good benchmark for the model's PV module temperature prediction accuracy.

**(a)** Ground Mounted PV System Site

**(b)** Rooftop PV System Site

**Figure 2.2:** Land-based PV systems sites used for model validation

The Fuentes Thermal Model, as derived in the previous section, is implemented and compared to site data collection that has been done by Dörenkämper et al. [21]. The first system is a ground mounted PV installation located in a rural area with open surroundings, allowing a relatively unobstructed airflow and radiative cooling. The second system is a rooftop PV installation in an urban environment, where heat exchange might be influenced by nearby structures as well as relatively limited airflow under the PV module compared to ground-mounted system's case. Both systems environmental and system's data are monitored using thermal sensors and weather stations to record PV module backsheet temperatures, ambient temperature, irradiance, and wind speed. The environmental input data for this PV system are given in Appendix A.

First, the Fuentes Thermal Model is applied to the ground-mounted PV system. In ground-mounted system, the PV module is mounted and elevated by several centimeters above the ground on a tilted metal rack, allowing airflow on both above and below the PV module, as shown by the picture in figure 2.2a. By solving the energy balance equation 2.6 using MATLAB's $ode45$ solver, PV module temperature profile was generated, shown in Figure 2.3. In the graph, the black line represents the measured on-site data and the blue plus signs represents the Fuentes Thermal Model result. From the graph, it can be observed that the model demonstrates a strong agreement with the measurement-derived data. The model is able to capture the temperature rise from early morning to mid-day, followed by temperature decline in the afternoon. To quantify the accuracy of the model, two statistical metrics are used, which are the root mean square error (RMSE) and mean absolute error (MAE). For this PV system configuration, the RMSE was calculated to be $1.03^oC$ and the MAE was $0.93^oC$, indicating a fairly high temperature prediction accuracy. Eventhough there are some discrepancies during peak irradiance hours, where the model tends to slightly overestimate the temperature, the low error values validate the suitability of the Fuentes Thermal Model for predicting PV module temperature for ground-mounted PV systems.

Next, the Fuentes FD Thermal model is implemented on a rooftop PV system. In a rooftop installation, as depicted in figure 2.2b, the PV module is mounted above the roof on a mounting system, typically without any additional truss. Consequently, in this configuration, the PV module's tilt angle is the same as the roof's tilt angle. The PV module receives airflow primarily from the top surface, while the back of the PV module has limited air gap due to the way the PV module is mounted. The system is then

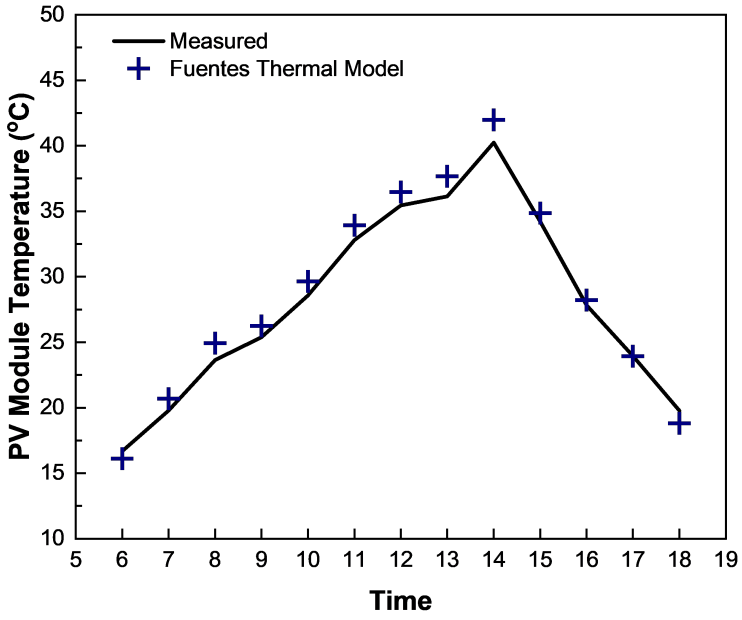


**Figure 2.3:** Temperature Comparison for Ground-Mounted PV System Using Fuentes Thermal Model

assessed using the same analytical fluid dynamics modelling approach and MATLAB solver, resulting in a PV module temperature comparison graph in figure 2.4.

From the graph, it is depicted that the modeled PV module temperature once again closely follows the measured temperatures with good overall accuracy throughout the day. The calculated RMSE is $1.06^oC$ and the MAE is $0.96^oC$, which demonstrates that the model remains robust even in rooftop PV installation conditions. However, unlike in the ground-mounted case, for rooftop PV configuration, the model consistently shows a slight underestimation of the PV module temperature, particularly during peak sun hour time range. This underestimation is likely due to the relatively limited convective heat dissipation beneath the PV module in rooftop installations, where smaller air gaps and mounting directly above warmer roof surfaces reduce airflow and cooling effectiveness. Nevertheless, the low error values confirm that the model still provides a reliable approximation for rooftop thermal behaviour [27].

Having demonstrated good agreement between modeled and measured PV module temperatures in land-based systems, the analytical fluid dynamics model is now evaluated for floating PV configurations. Unlike ground-mounted or rooftop systems, floating PV systems operate in close proximity to water surfaces, introducing distinct thermal behaviour due to enhanced cooling effects and changes in convective heat transfer. The following subsection implements the Fuentes Thermal Model to diverse floating PV configurations to assess its accuracy and limitations under different floating system and environmental conditions.

### 2.1.3. Implementation of Fuentes FD Thermal Model for Floating PV Systems

This section presents the implementation of the Fuentes Thermal Model for floating PV system. The objective is to assess the model's ability to predict PV module temperature under floating installation conditions, where enhanced cooling effects due to proximity to water and modified airflow influence thermal behaviour. The implementation uses several meteorological inputs such as ambient temperature, wind speed, solar irradiance, and relative humidity. The results are then compared against measured data to evaluate the accuracy and limitations of this model in floating PV applications.

For the base study case of the implementation of Fuentes Thermal Model for floating PV, the thermal model is implemented for an existing floating PV system located in Passauna region in Brazil, based

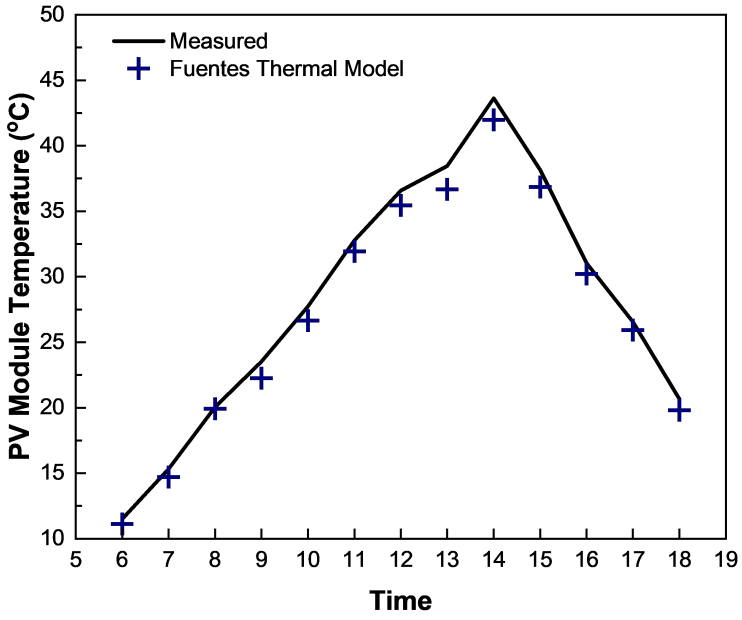


**Figure 2.4:** Temperature Comparison for Rooftop PV System Using Analytical Fluid Dynamics Model

on the study of Rahaman et al. [28]. This study was chosen as base case because in this study, an on-site measurement is done for both the weather data and the PV system's production data which includes PV module temperatures as well as the system's electrical production data. The measured environmental data is given in Appendix A. In this section, The Fuentes Thermal Model is implemented in this system, and the simulated PV module temperature results are compared to the measured data to assess its accuracy. Running the Fuentes fluid dynamics model for the given environmental input, results in the PV module temperature as depicted in figure 2.5.

From the comparison between the Fuentes FD modelled PV module temperature against measured PV module temperatures, it is apparent that the Fuentes FD model consistently overestimates the PV module temperatures. The extent of the deviation between the modelled and measured PV module temperature is noticably bigger than the Fuentes FD model's implementation for land-based system, as discussed in the previous sub-chapter. For this base study case, the RMSE is calculated to be $2.03^oC$ and the MAE is $1.82^oC$. These error values are significantly higher, compared to the error values of implementing Fuentes FD model for land-based PV systems. This indicates that applying the Fuentes FD model to floating PV system results in a lower PV module temperature prediction accuracy.

In order to have a more comprehensive understanding of how does the Fuentes FD model performs in predicting PV module temperatures, additional case study is done for several different floating PV configurations. According to a review on floating PV configurations [29], floating PV systems can be classified into several archetypes based on several categories. These categories include the type and material of the floater, the proximity of the PV module to the water surface, and the amount of PV module's area that is exposed to the water, or water footprint. This section aims to apply the Fuentes Thermal Model to different floating PV archetypes and analyze these model's applicability, in terms of PV module temperature prediction accuracy.

The Fuentes Thermal Model is implemented across multiple floating PV configurations to evaluate its predictive capability in diverse mounting scenarios. Although the broader focus of this thesis is comparing floating PV with land-based systems, investigating various floating PV archetypes remains valuable. In accordance with technical review by Sathya et al. [29], three of the most common floating PV configurations are considered, which are Horizontal Pontoon with Truss (HPOT), Horizontal Pipe

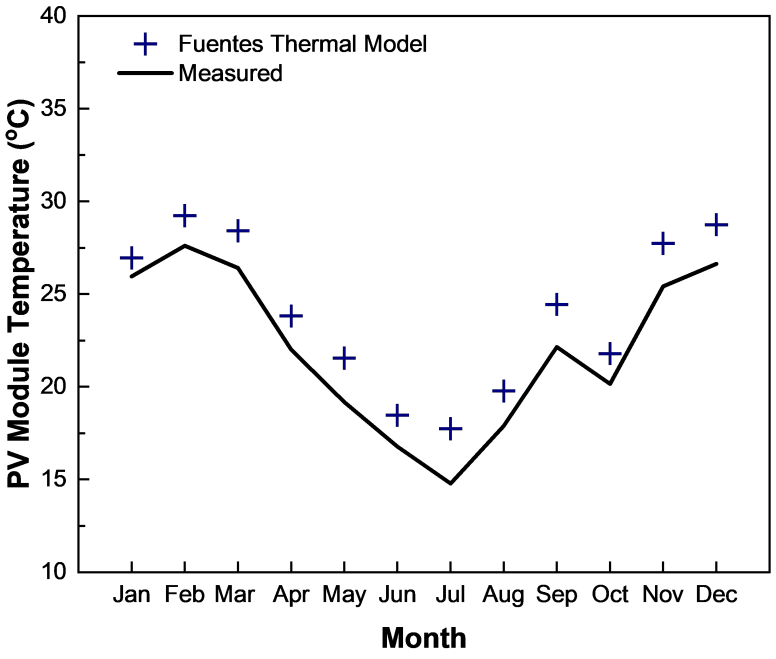


**Figure 2.5:** PV Module Temperature Result Comparison for Rahaman et al. Base Case Study using Fuentes Thermal Model

with Truss (HPIT), and the Membrane Ring structure. These archetypes are chosen to represent a range of water footprints and airflow characteristics, as summarized in table 2.1.

In addition to diverse floater configuration, floating PV systems are also commonly classified based on the water exposure relative to the PV module's backside, this term is referred to as **floater exposure**. Large floater footprint indicates that a large portion of the water surface area is covered by the floating structure under the PV module. Consequently, for large floater footprint, the PV module experiences a small water exposure. In contrary, small floater footprint indicates that a small portion of the water surface area is covered by the floating structure under the PV module. Consequently, for small floater footprint, the PV module experiences a large water exposure.

**Table 2.1:** Floating PV Floater Types and Water Footprint

| Location | Floater Type | Floater Footprint |
|---|---|---|
| The Netherlands | Horizontal Pontoon with Truss (HPOT) | Large Floater Footprint |
| South Africa | Horizontal Pontoon with Truss (HPOT) | Medium Floater Footprint |
| Singapore | Horizontal Pontoon with Truss (HPOT) | Small Floater Footprint |
| The Netherlands | Horizontal Pipe with Truss (HPIT) | Small Floater Footprint |
| Norway | Membrane Ring | - |

Figure 2.6a illustrates the HPOT configuration, where a flat rectangular pontoon structure supports the PV module. The HPIT configuration, shown in figure 2.6b uses cylindrical pipe floaters instead of solid pontoons. Lastly, the membrane ring design in figure 2.6c features a flexible circular thin membrane supporting the PV module with with minimal structural support beneath it, effectively negating any airflow under the PV module.

It is important to note that in this sub-chapter, a single Fuentes Thermal Model, as derived in sub-chapter 2.1 will be applied to different floating PV archetypes without adjusting any parameters to incorporate different thermal behaviour for each floating PV configuration. By doing so, the goal of this sub-chapter

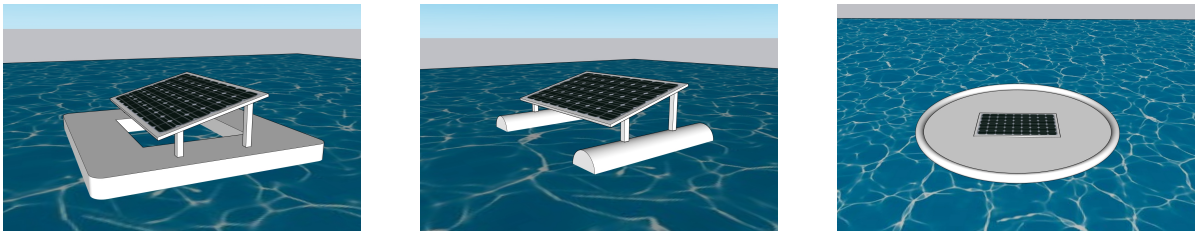

**(a)** HPOT **(b)** HPIT **(c)** Membrane Ring

**Figure 2.6:** Floating PV mounting structures: (a) HPOT, (b) HPIT, (c) Membrane Ring

is to see how well does the single referred analytical fluid dynamics model represent various floating PV archetype, as well as to conclude the necessity of adjusting key parameters to incorporate different floating PV archetypes.

The first floating PV system is horizontal pontoon with truss (HPOT) with large floater footprint. In this classification, the floater is a pontoon made of High Density Polyethylene (HDPE). The PV module is mounted on the pontoon using aluminum mounting structure, and tilted to a specific tilt angle and azimuth direction using truss structure. To re-emphasize, floater footprint can be defined as the amount of water covered by the floater, relative to the area of the PV module. Large water footprint indicates that a large portion of the water is covered by the floating structure, hence the water exposure to the backside of the PV module is low.

For this archetype, a study case by Dörenkämper et al. [21] is used, where an onsite measurement was done to measure the environmental inputs such as plane-of-array irradiance, ambient temperature, water temperature, and wind speed for a floating PV system in the Netherlands. The environmental data is given by Appendix A. These data for these environmental input is given as an hourly value during daytime for the specific site location.

These environmental conditions are used as inputs to the Fuentes Thermal Model. Running the two models using MATLAB as a numerical solver yields the results as depicted in figure 2.7.

Figure 2.7 shows the comparison between the modeled PV module temperature and measurement-derived temperature values throughout the day for HPOT with large water footprint. The black line represents the measurement-derived PV module temperature values and the blue plus signs represent the modeled PV module temperature values. From the result, it can be seen that the model captures the diurnal trend relatively accurately, with module temperatures rising steadily from morning, peaking between 13:00 to 14:00, and decreasing in the late afternoon. However, while the pattern of the temperature curve aligns well with observed data, the model consistently **overestimates** the PV module temperature during peak solar hours, with the highest deviation occuring between 11:00 and 15:00. This overestimation may be caused by the model's simplified assumptions, such as convective heat transfer coefficients and does not reflect the enhanced cooling effects present over water during high-irradiance conditions [30].

To quantify the accuracy of the model, the root mean square error (RMSE) was calculated as $4.7^oC$, and the mean absolute error (MAE) was found to be $3.97^oC$. While these values indicate moderate agreement between modeled and measured temperatures, the amount of deviation, particularly during peak sun hours suggests that the analytical fluid dynamics model may not fully capture the thermal behaviour in floating PV environments. Therefore, although the model provides a useful first-order estimate, its limitations show the need for a more detailed thermal model.

The second archetype is horizontal pontoon with truss (HPOT) with medium floater footprint. In this classification, the floater is a pontoon made of High Density Polyethylene (HDPE). The PV module is mounted on the pontoon using aluminum mounting structure, and tilted to a specific tilt angle and azimuth direction using truss structure. Medium floater footprint indicates that a approximately half of the water is covered by the floating structure, relative to the PV module area, hence the water exposure to the backside of the PV module is moderate.

For this archetype, a study case by Willemse et al. [31] is used, where an on-site measurement was

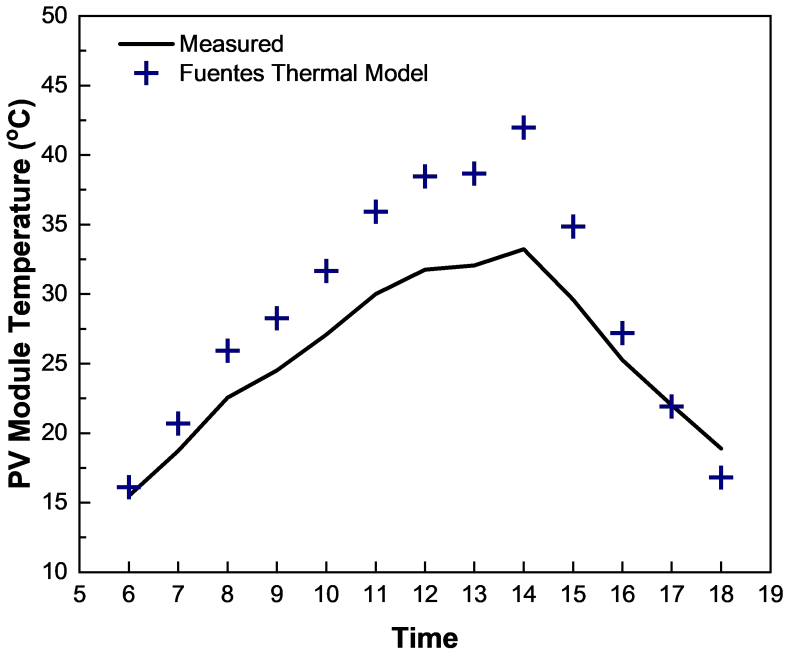


**Figure 2.7:** PV Module Temperature Result Comparison for HPOT Large Floater Footprint

done to record key environmental input data such as plane-of-array irradiance, ambient temperature, water temperature, and wind speed for a floating PV system in South Africa. The measurement data is given in Appendix A. These data for these environmental input is given as an hourly value during daytime for the specific site location.

These environmental conditions are used as inputs to the analytical fluid dynamics model. Running the two models using MATLAB as a numerical solver yields the results as depicted in figure 2.8.

Figure 2.8 shows the comparison between the modeled PV module temperature using the Fuentes Fluid Dynamics Model and the measurement-derived values for the HPOT configuration with a medium water footprint, located in South Africa. As in the previous case, the black line represents the measured PV module temperature data, while the blue plus signs denote the Fuentes Thermal Model predictions. The overall trend of the measured temperature is well captured by the model, showing a steady rise between 10:00 and 13:00. However, the Fuentes Fluid Dynamics Model shows a clear and consistent **overestimation** of the PV module temperature across all time points, with the gap increasing in the later part of the observation period. This overestimation is likely due to the same limitations observed in the large water footprint case, which is the model's inaccurate assumptions of convective and radiative heat exchange with the surrounding environment that is unable to represent the cooling effect due to the presence of water.

Similar to the previous case, the RMSE was calculated to quantify the model's accuracy for this floating PV configuration. The RMSE was calculated was $6.52^{v}C$ and the MAE was found to be $6.48^{o}C$. These error values are substantially higher than those observed in the large water footprint case, indicating that the Fuentes Thermal Model perform less reliably under medium floater footprint conditions. The consistent overestimation suggests that the model's heat transfer assumptions fail to fully represent the thermal behaviour of this specific configuration. Therefore, while Fuentes Thermal Model remains useful for generating initial predictions, its limitations are more apparent in configurations with more water-induced cooling. This further reinforces the need for a more physically detailed approach, motivating the development of alternative thermal model in the following sub-chapter to enhance the model's accuracy and applicability.

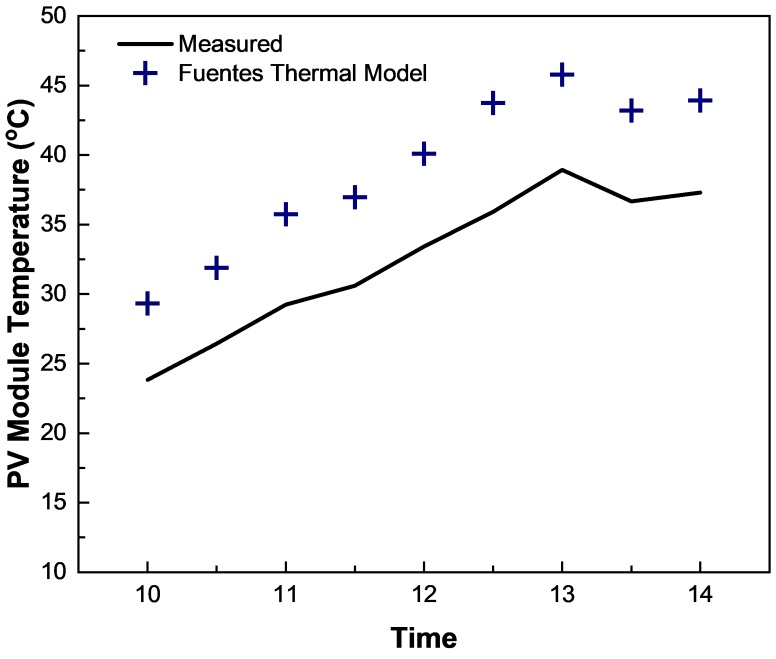


**Figure 2.8:** PV Module Temperature Result Comparison for HPOT Medium Floater Footprint

The third archetype is horizontal pontoon with truss (HPOT) with small floater footprint. In this classification, the floater is a pontoon made of High Density Polyethylene (HDPE). The PV module is mounted on the pontoon using aluminum mounting structure, and tilted to a specific tilt angle and azimuth direction using truss structure. Small floater footprint indicates that a small portion of the water is covered by the floating structure, relative to the PV module area, hence the water exposure to the backside of the PV module is high.

For this archetype, a study case by Dörenkämper et al. [21] is used, where an onsite measurement was done to measure the environmental inputs such as plane-of-array irradiance, ambient temperature, water temperature, and wind speed for a floating PV system in Singapore. The measured environmental data is given in Appendix A. These data for these environmental input is given as an hourly value during daytime for the specific site location.

These environmental conditions are used as inputs to the Fuentes Thermal Model. Running the model using MATLAB as a numerical solver yields the results as depicted in figure 2.9.

Figure 2.9 presents the comparison between the analytical fluid dynamics model prediction and measurement-derived PV module temperatures for HPOT configuration with small floater footprint, located in Singapore. In this configuration, a smaller floater coverage allows for more direct water exposure beneath the PV module, which is expected to enhance convective and evaporative cooling. However, the analytical fluid dynamics model fails to capture this cooling effect adequately. As shown in the figure, the model substantially **overestimates** PV module temperature, particularly between 11:00 and 15:00, with a peak deviation observed around midday. While the general pattern is somewhat similar to measured values, the model predicts significantly higher temperatures throughout most of the day.

This discrepancy is also reflected in the error metrics. The RMSE is calculated as $6.53^oC$ and the MAE is $5.56^oC$, These results indicate poor agreement between modeled and observed values, further reinforcing the argument that the model is lacking the ability to capture water-cooling effects, particularly for systems with a large water exposure where greater air-water interactions are expected due to minimal floater obstruction. This reinforces the conclusion that an improved modelling approach is necessary

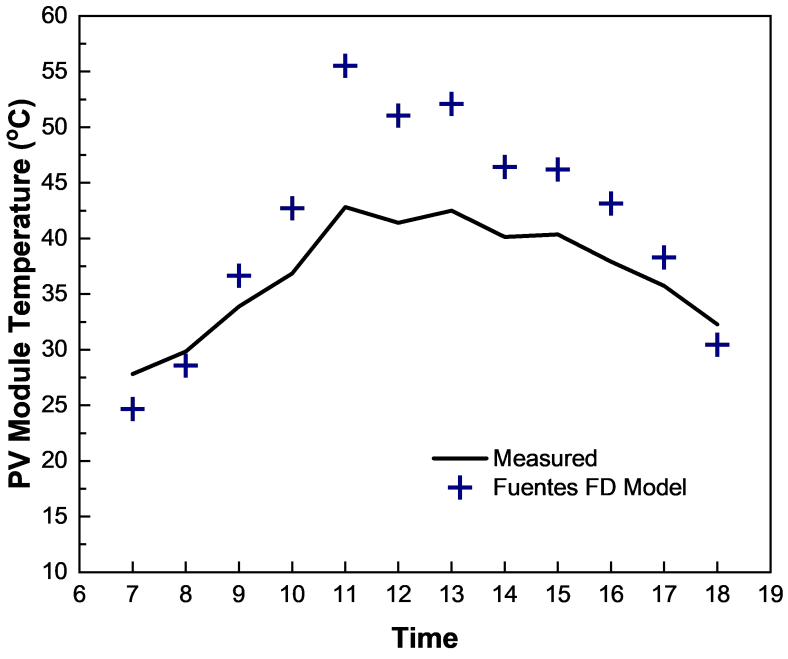


**Figure 2.9:** PV Module Temperature Result Comparison for HPOT Small Floater Footprint

to more accurately account for the distinct thermal behaviour of floating PV systems.

The next archetype is horizontal pipe with truss (HPIT) with small floater footprint. In this classification, the floater is a cylindrical pipe made of High Density Polyethylene (HDPE). The PV module is mounted on the cylindrical pipe using aluminum mounting structure, and tilted to a specific tilt angle and azimuth direction using truss structure. Small floater footprint indicates that a small portion of the water is covered by the floating structure, relative to the PV module area, hence the water exposure to the backside of the PV module is high.

For this archetype, a study case by Dörenkämper et al. [21] is used, where an onsite measurement was done to measure the environmental inputs such as plane-of-array irradiance, ambient temperature, water temperature, and wind speed for a floating PV system in the Netherlands. The measured environmental data is given in Appendix A. These data for these environmental input is given as an hourly value during daytime for the specific site location.

These environmental conditions are used as inputs to the Fuentes Thermal Model. Running the two models using MATLAB as a numerical solver yields the results as depicted in figure 2.10.

Figure 2.10 illustrates the comparison between the modeled PV module temperature using the Fuentes Thermal Model and the measurement-derived values for the HPIT configuration with small floater footprint. In this design, cylindrical pipe floaters support the PV module while a relatively large portion of the water surface exposed beneath it, enabling stronger convective cooling effects than structures with a larger water footprint. However, similar with HPOT with small floater footprint, the simulated PV module temperature results of Fuentes Thermal Model is once again unable to represent these thermal behaviour accurately. As shown in the graph, the model consistently **overestimates** the PV module temperature throughout the day with the largest discrepancies occuring between 10:00 and 14:00, during peak sun hours.

The error metrics reflect this mismatch, with a RMSE of $7.05^oC$ and a MAE of $6.17^oC$. These values indicate that Fuentes Thermal Model has the lowest accuracy for this configuration compared to previous cases. The likely cause lies in the model's inaccurate assumptions for convective heat transfer coeffi-

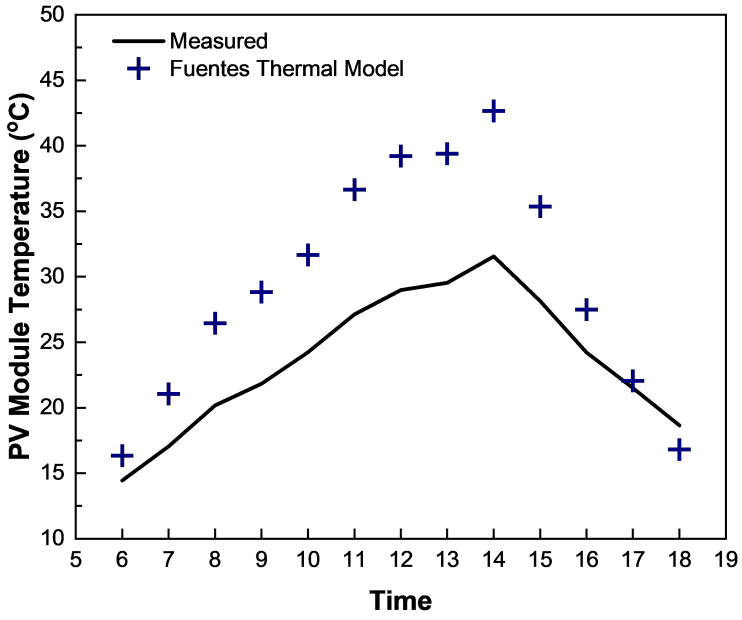


**Figure 2.10:** PV Module Temperature Result Comparison for HPIT Small Floater Footprint

cients, which do not account for the air-water interaction or airflow patterns around the PV module and exposed water surfaces [32]. This result also shows the limitation of the implementation of the Fuentes Thermal Model in floating PV application, and emphasizes the importance of updating the model with another alternative analytical model to incorporate floating PV thermal behaviour.

The next archetype is membrane ring floating PV. This is a floating solar PV system design that utilizes a flexible membrane structure supported by a ring-shaped buoyant frame. This design allows the PV modules to rest on a thin, water-permeable or airtight membrane, which can enhance cooling through direct water contact or evaporative effects. The ring provides structural integrity while enabling the system to adapt to water surface movements, reducing mechanical stress. This archetype is particularly advantageous for minimizing material usage, improving thermal regulation, and enhancing system stability in moderate wave conditions [33].

For this archetype, a study case by Kjeldstad et al. [22] is used, where an onsite measurement was done to measure the environmental inputs such as plane-of-array irradiance, ambient temperature, water temperature, and wind speed for a floating PV system in the Norway. The measured data is given in Appendix A. These data for these environmental input is given as an hourly value during daytime for the specific site location.

These environmental conditions are used as inputs to the Fuentes Thermal Model. Running the two models using MATLAB as a numerical solver yields the results as depicted in figure 2.11.

Figure 2.11 shows the comparison between the analytical fluid dynamics model prediction and measurement-derived PV module temperatures for the membrane ring floating PV configuration, located in Norway. In this configuration, instead of utilizing a floater like previous archetypes, a thin, flexible membrane is used to keep the PV modules afloat. The PV module is mounted directly above the flexible membrane with minimal gap so that the PV module directly touches the membrane with no air gap underneath the PV module. As shown in the result graph, the analytical fluid dynamics model significantly **overestimates** the PV module temperature throughout the day, particularly in the midday and afternoon periods, with the largest deviation occurring between 12:00 and 16:00. The analytical fluid dynamics model consistently predicts higher temperatures than both the measured data and the resistive model, indicating that it may be overestimating heat absorption or underestimating convective and evaporative

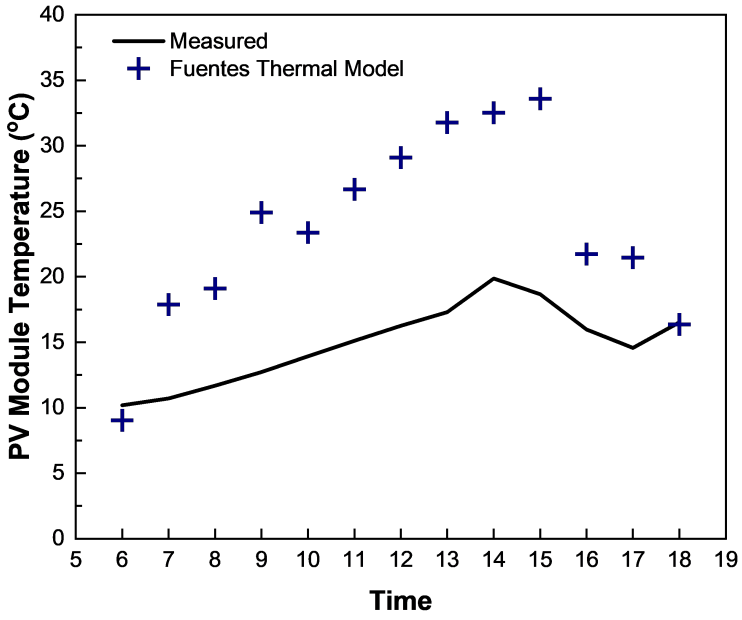


**Figure 2.11:** PV Module Temperature Result Comparison for Membrane Ring

cooling effects provided by the membrane structure.

Quantitatively, the amount of deviation is represented again with RMSE and MAE, with the RMSE value of $10.07^oC$ and MAE of $8.97^oC$, the highest among all evaluated configurations. These significant discrepancies is likely caused by the model's inability to account for the distinct heat dissipation due to the absence of airflow beneath the PV module. Instead, the heat for the PV module is mostly dissipated conductively through the flexible membrane, then to the water. The membrane ring archetype is expected to have a strong cooling effect due to direct water contact and evaporative cooling [34]. Refinements in convective and radiative heat transfer assumptions, along with better representation of membrane-specific thermal characteristics, could improve model accuracy.

### 2.1.4. Summary of Comparison Between the Measured and Predicted PV Module Temperature

The summary of comparison between the measured and modelled PV module temperature is depicted by figure 2.12

From the figure, the lowest RMSE can be observed for HPOT with large floater footprint. This indicates that for large floater footprint and small water exposure, the heat dissipation is smaller, and more likely to represent land-based system. It can also be observed that with lower floater footprint and higher water exposure to the backside of the PV module, the RMSE increases, indicating higher cooling effect from the heat dissipation due to the exposure to the water surface.

For HPOT systems with a large water footprint, the models exhibit the highest accuracy, with the Fuentes Thermal Model showing an RMSE of 4.07°C. The relatively small error indicates that heat transfer mechanisms in floating PV systems with minimal water exposure are more predictable, making it easier for the models to approximate module temperatures. However, because less water reaches the module's backside, the system experiences reduced evaporative and convective cooling, leading to higher module temperatures overall.

As the floater footprint decreases (more water exposure to the module), the models become less accurate. For HPOT systems with medium and small floater footprint, the Fuentes Thermal Model's RMSE rises from 4.07°C to around 6.53°C. The increasing error suggests that higher water exposure

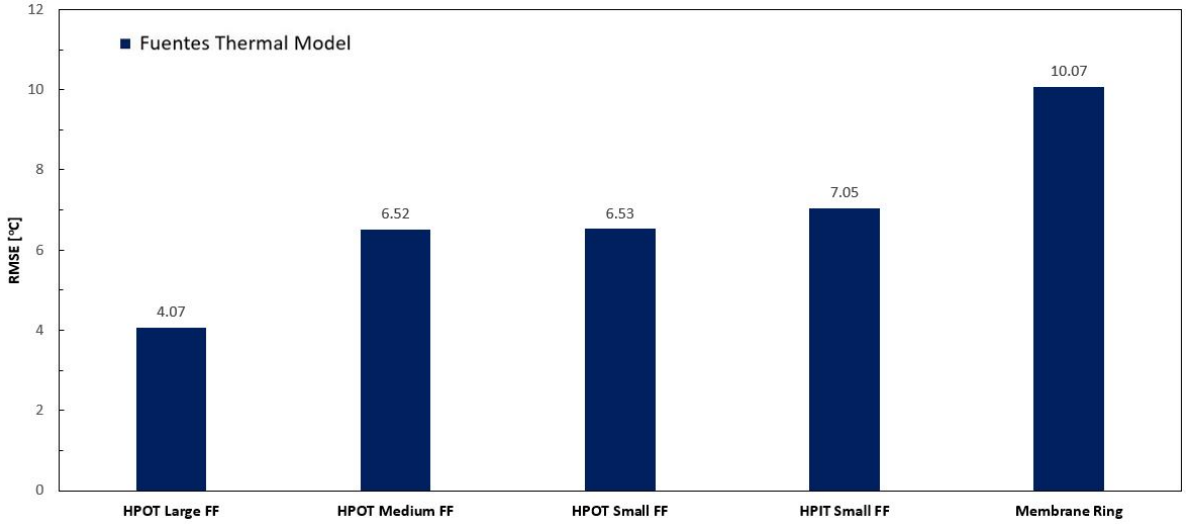


**Figure 2.12:** PV Module Temperature Result Comparison using Fuentes Thermal Model

enhances cooling effects that are not fully captured by the model. In particular, evaporative cooling and convective heat transfer along the module's backside become more significant with smaller floater footprints, likely introducing nonlinear cooling effects that the models fail to represent accurately [35]. For HPIT systems with a small water footprint, the RMSE values are moderately high, with 7.05°C for the Fluid Dynamics Model. This suggests that HPIT systems experience a similar increase in cooling efficiency due to enhanced water exposure, making heat dissipation more complex than what the models account for.

The Membrane Ring floating PV archetype exhibits the highest RMSE values, with 10.07°C for the Fuentes Thermal Model. Unlike HPOT and HPIT, the membrane ring archetype allows direct water contact with the module's lower surface, enhancing evaporative and convective cooling effects beyond what is seen in conventional floating PV designs. The overestimation of module temperature in both models indicates that these additional cooling effects are not properly captured, leading to higher error in the PV module temperature predictions.

From the results of applying the Fuentes Thermal Model for floating PV systems, it can be concluded that while the model performs reasonably well in capturing general temperature trends, it consistently overestimates the PV module temperatures, especially in configurations with small floater water footprint (large water exposure). As mentioned, these discrepancies is likely caused by the model's limited assumption on key heat transfer coefficients, such as the convective heat transfer coefficent that is largely affected by the airflow beneath the module, affected by air-water interaction. To overcome these limitations and improve prediction accuracy, alternative modelling approach is required that can better represent heat transfer mechanisms through distinct thermal interfaces. The following section introduces a resistive thermal model, developed to address this need by incorporating a network of thermal resistances that represents heat dissipation path, derived specifically for floating PV installations.

## 2.2. Resistive Thermal Model

Fuentes Thermal Model is an established model that has been widely used as a validated analytical thermal model. As discussed in the previous sub-chapter, this model has been proved to have good accuracy for land-based PV system. However, for floating PV installations, applying Fuentes Thermal Model and comparing the modelled PV module temperatures with measured data revealed that it results in a low prediction accuracy. These findings indicate that it is necessary to develop an alternative model that is capable of accurately predicting PV module temperatures for floating PV applications.

In this sub-chapter, an alternative physics-based analytical thermal model is developed, namely the Resistive Thermal Model. The Resistive Thermal Model will first be derived specific to floating PV

installation environment. Next, its performance in predicting PV module temperatures will be evaluated for the same installation sites as done in previous chapter. This approach would enable a consistent comparison of PV module temperature results between the newly-developed Resistive Thermal Model and the existing Fuentes Thermal Model.

### 2.2.1. Derivation of the Resistive Thermal Model for Floating PV Application

The Resistive Thermal Model is one of the simplest ways to illustrate and quantify heat transfer processes. It represents heat transfer as a network of thermal resistances, similar to an electrical circuit analogy. The basis of the resistive thermal model is the concept of thermal resistance, which quantifies heat transfer mechanisms, represented by conduction resistance, convection resistance, and radiative resistance. By assigning specific resistance values to each pathway, the model quantifies how much heat is transferred and where losses occur under various environmental conditions. Thermal resistances in the model are based on material properties such as layer thickness, density, and thermal conductivity. This approach offers a simplified but effective method for calculating the PV module temperature under practical operational conditions. Resistive thermal modelling serves as the foundational framework for energy balance equation by establishing the concept of thermal resistance to represent heat transfer across different layers of a PV module.

To accurately capture the distinct thermal behaviour of floating PV systems, it is essential to develop specific resistive thermal models for different floating PV configurations. Similar to land-based systems, such as rooftop PV systems and land based systems that experiences different airflow that differently affects heat dissipation from the PV module, different floating PV configurations also exhibits varying heat transfer mechanisms. To be consistent with the discussion in previous sub-chapter, the resistive thermal model in this section will be developed for Horizontal Pontoon with Truss (HPOT), Horizontal Pipe with Truss (HPIT), and membrane ring. By constructing configuration-specific equivalent thermal circuits, conduction, convection, and radiation can be explicitly represented through thermal resistances. These circuits provide the foundation for deriving detailed energy balance equations, enabling a more accurate temperature prediction of PV module under varying environmental conditions.

For HPOT configuration, the key mechanisms of heat transfer are conduction through the PV module layers, convection to the ambient air, radiation to the sky and water, and conduction through the mounting structure into the floating platform. Figure 2.13 illustrates the heat dissipation mechanisms for the HPOT configuration. The PV module receives energy input from the incident irradiance and the energy absorbed as heat within the PV module, denoted as $G_{POA}$ and $Pheat, abs$ consecutively. Heat dissipates through the top surface of the PV module ($Q_{conv,up}$) by convection with the ambient air $T_{amb}$ and radiation to the sky ($Q_{rad,up}$) with its sky temperature $T_{sky}$. Similarly, at the back surface, heat loss occurs by convection with the air below the PV module ($Q_{conv,down}$) and radiation ($Q_{rad,down}$) to the water surface with a certain water temperature $T_w$. Additionally, conduction heat transfer also occurs from the PV module back surface to the floating structure to finally be dissipated in the water ($Q_{cond,float}$).

These mechanisms are translated into the equivalent thermal circuit shown in figure 2.14, where each resistance represents a heat transfer path. The node $T_F$ corresponds to the front surface of the PV module, and $T_B$ corresponds to the back surface.

With respect to node $T_F$, the incident energy from the sun irradiation $P_{\text{sun}}$ is received. $P_{\text{sun}}$ is directly dependent on the incoming plane-of-array irradiance $G_{\text{POA}}$, the PV module's area $A$, and the transmissivity and absorptivity of the PV module's front glass $\tau\alpha$, as depicted in Equation (2.7).

$$P_{\text{sun}} = \tau \times \alpha \times A_{\text{PV}} \times G_{\text{POA}} \tag{2.7}$$

This heat is dissipated through multiple pathways. Firstly, the heat is transferred radiatively to the sky with thermal resistance $R_{\text{rad,up}}$. The radiative heat transfer coefficient is affected by the front glass emissivity, Stefan-Boltzmann constant, ambient temperature $T_{\text{amb}}$, and sky temperature $T_{\text{sky}}$, as given by Equation (2.8).

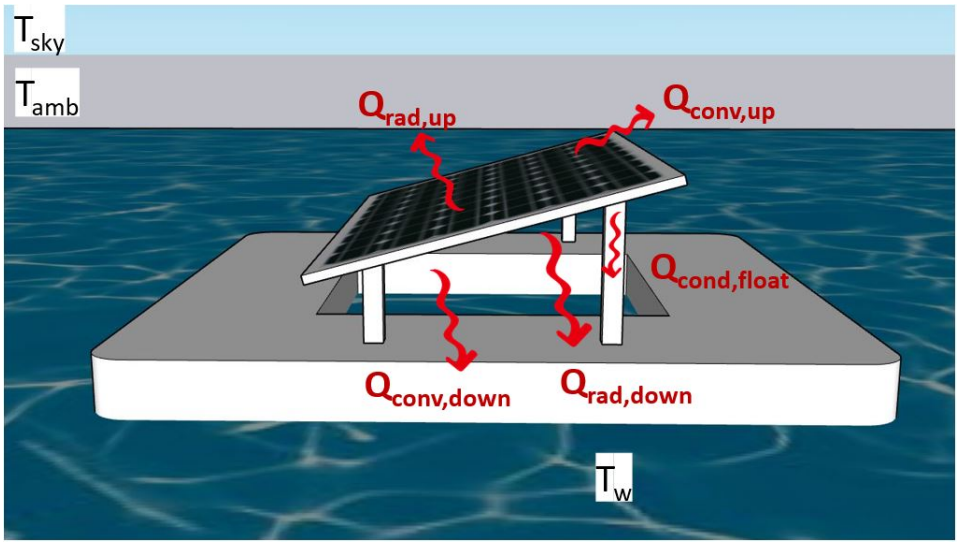


**Figure 2.13:** Heat Transfer Mechanisms for Floating PV HPOT Configuration

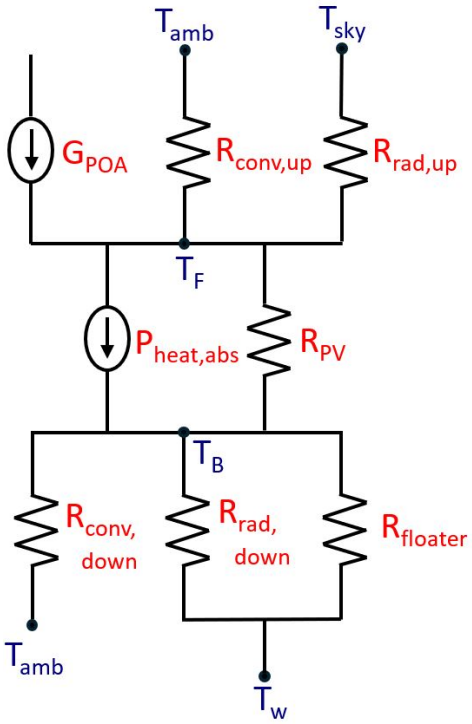


**Figure 2.14:** Equivalent Thermal Circuit for Floating PV HPOT Configuration

$$R_{\text{rad,up}} = \frac{1}{\epsilon_g \sigma \times (T_{\text{amb}}^4 + T_{\text{sky}}^3) \times (T_{\text{up}} + T_{\text{sky}})} \tag{2.8}$$

where

$$T_{\text{sky}} = 0.0052 \times T_{\text{amb}}^{1.5} \tag{2.9}$$

Secondly, the heat is dissipated through convection due to ambient temperature and airflow from wind from the upper side of the PV modules. The convection heat transfer caused by ambient temperature is the free convection heat transfer, while the convection heat transfer caused by the presence of airflow is the forced heat transfer. Both free and forced heat transfer coefficients affect the overall convection heat transfer coefficient through a correlation depicted in Equation (2.10).

$$h_{\text{conv}} = \sqrt[3]{h_{\text{conv,free}}^3 + h_{\text{conv,forced}}^3} \tag{2.10}$$

The free convective heat transfer coefficient is affected by the free Nusselt number $Nu_{\text{free}}$, air conductivity $k_{\text{air}}$, and the PV module's length $L_{\text{PV}}$, given by Equation (2.11).

$$h_{\text{conv,free}} = \frac{Nu_{\text{free}} \times k_{\text{air}}}{L_{\text{PV}}} \tag{2.11}$$

For free convection, the Nusselt number equation is dependent on the Rayleigh number $Ra$:

$$Nu_{\text{free}} = \begin{cases} 0.54(Ra \times \cos\beta)^{1/4}, & 10^4 \leq Ra \times \cos\beta \leq 10^7 \\ 0.15(Ra \times \cos\beta)^{1/3}, & 10^7 \leq Ra \times \cos\beta \leq 10^{11} \end{cases} \tag{2.12}$$

The forced convective heat transfer coefficient is affected by the forced Nusselt number $Nu_{\text{forced}}$, as given by Equation (2.13).

$$h_{\text{conv,forced}} = \frac{Nu_{\text{forced}} \times k_{\text{air}}}{L_{\text{PV}}} \tag{2.13}$$

For forced convection, if $Re \leq 5 \times 10^5$:

$$Nu_{\text{forced}} = 2 \times \frac{0.3387 \times Re^{1/2} \times Pr^{1/3}}{\left(1 + (0.0468/Pr)^{2/3}\right)^{1/5}} \tag{2.14}$$

If $Re > 5 \times 10^5$:

$$Nu_{\text{forced}} = 2 \times Pr^{1/3} \times \left(Re^{4/5} - 871\right) \tag{2.15}$$

The heat is also dissipated conductively through the PV module layers with thermal resistance $R_{\text{cond,layer}}$, which is affected by the conductivity of each layer within the PV module.

$$R_{\text{cond,layer}} = \frac{L_{\text{layer}}}{k_{\text{layer}} \times A_{\text{PV}}} \tag{2.16}$$

$$R_{\text{cond,float}} = \frac{L_{\text{float}}}{k_{\text{float}} \times A_{\text{float}}} \tag{2.17}$$

The amount of incident energy absorbed as heat in the PV module layer is denoted as $P_{\text{heat,absorbed}}$:

$$P_{\text{heat,absorbed}} = A_{\text{PV}} \times G_{\text{POA}} \times Ab \tag{2.18}$$

Using Kirchhoff's Current Law (KCL), the ordinary differential equation (ODE) for the front surface temperature $T_F$ is:

$$\frac{dT_F}{dt} = \frac{2}{m \times C_p} \left( P_{sun} + P_{heat,abs} - \frac{T_F - T_{amb}}{R_{conv,up}} - \frac{T_F - T_{sky}}{R_{rad,up}} - \frac{T_F - T_B}{R_{cond,PV}} \right) \tag{2.19}$$

where:

- $m$ is the mass of the module
- $C_p$ is the specific heat capacity of the PV module material
- $T_F$ and $T_B$ are the front are back surface temperatures of the PV module
- $T_{amb}$, $T_{sky}$, and $T_W$ are the ambient, sky, and water temperatures, respectively

Similarly, solving for the back surface temperature $T_B$:

$$\frac{dT_B}{dt} = \frac{2}{m \times C_p} \left( \frac{T_B - T_F}{R_{cond,layer}} + P_{heat,abs} - \frac{T_B - T_w}{R_{conv,down}} - \frac{T_B - T_w}{R_{rad,down}} - \frac{T_B - T_w}{R_{cond,float}} \right) \tag{2.20}$$

This equation allows an accurate representation of the PV module temperature, taking into account multiple parallel and series heat transfer paths. It also enables the model to be customized for different floating configurations by adapting the resistance path and values based on structural and environmental characteristics.

The next floating PV configuration, HPIT (Horizontal Pipe with Truss) features cylindrical pipe floaters that provide only partial coverage of the water surface beneath the PV module. As a result, the module is more exposed to ambient air and water, which introduces different thermal behaviour compared to the HPOT configuration. The key heat transfer pathways for this archetype are illustrated in figure 2.15, which include convective and radiative heat dissipation at both the top and bottom surfaces of the PV module, as well as conductive heat transfer through the mounting structure to the floater surface.

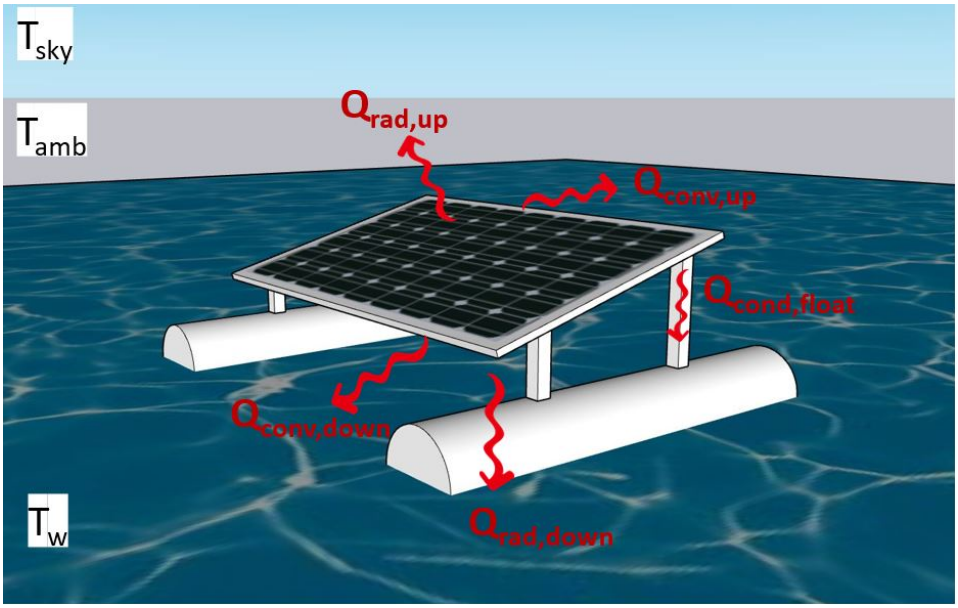


**Figure 2.15:** Heat Transfer Mechanisms for Floating PV with HPIT Configuration

The corresponding equivalent thermal circuit for this configuration is shown in figure 2.16. This thermal circuit builds upon the same heat dissipation pathways as introduced in the HPOT model but includes

two separate conductive resistances, namely $R_{float,1}$ and $R_{float,2}$ to represent the two-point contact between the module and the cylindrical pipe floateres. This change reflects that the heat conduction path in HPIT is distributes across two different contact lines rather than just one contact point.

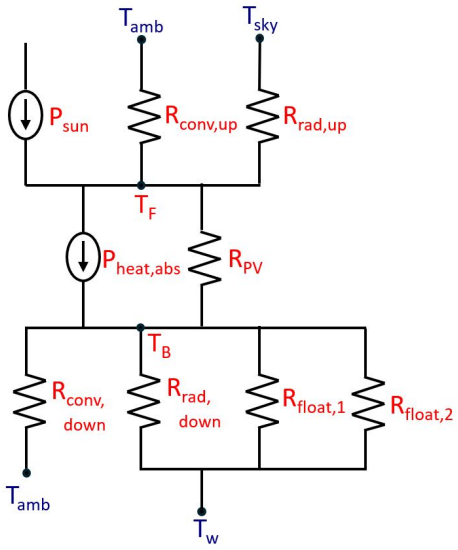


**Figure 2.16:** Heat Transfer Mechanisms for Floating PV with HPIT Configuration

The resulting energy balance equations for the HPIT configuration are as follows:

$$\frac{dT_F}{dt} = \frac{2}{mC_p}\left(P_{\text{sun}} + P_{\text{heat,abs}} - \frac{T_F - T_{\text{amb}}}{R_{\text{conv,up}}} - \frac{T_F - T_{\text{sky}}}{R_{\text{rad,up}}} - \frac{T_F - T_B}{R_{\text{cond,PV}}}\right) \tag{2.21}$$

$$\frac{dT_B}{dt} = \frac{2}{mC_p}\left(\frac{T_B - T_F}{R_{\text{cond,layer}}} + P_{\text{heat,abs}} - \frac{T_B - T_w}{R_{\text{conv,down}}} - \frac{T_B - T_w}{R_{\text{rad,down}}} - \frac{T_B - T_w}{R_{\text{cond,float,1}}} - \frac{T_B - T_w}{R_{\text{cond,float,2}}}\right) \tag{2.22}$$

These updated equations allow the model to more accurately represent the influence of reduced structural contact and increased water exposure on PV module temperature behaviour in HPIT configuration.

The third floating PV configuration, the membrane ring, introduces a unique thermal dynamics due to the direct contact between the PV module and a flexible membrane, eliminating any air gap beneath the PV module. This design significantly limits convective cooling on the underside of the PV module, while increasing conductive heat transfer through the membrane finally convective to the water surface. The key heat transfer mechanisms in this configuration are shown in figure 2.17. These includes upward convection and radiation losses, as well as downward heat conduction into the membrane and convection into the water surface.

The corresponding equivalent thermal circuit for membrane ring floating PV is shown in figure 2.18. The key difference between this archetype and HPOT and HPIT is that due to the limited and relatively non-existent convective cooling beneath the module, the convective resistance is now replaced by a conductive resistance of the thin flexible membrane. This conductive resistance is then connected in series to a convective resistance, representing the convective heat dissipation from the bottom of the membrane floater to the water below. The resulting energy balance equations are expressed as:

$$\frac{dT_F}{dt} = \frac{2}{mC_p}\left(P_{\text{sun}} + P_{\text{heat,abs}} - \frac{T_F - T_{\text{amb}}}{R_{\text{conv,up}}} - \frac{T_F - T_{\text{sky}}}{R_{\text{rad,up}}} - \frac{T_F - T_B}{R_{\text{cond,PV}}}\right) \tag{2.23}$$

$$\frac{dT_B}{dt} = \frac{2}{mC_p}\left(\frac{T_B - T_F}{R_{\text{cond,layer}}} + P_{\text{heat,abs}} - \frac{T_B - T_w}{R_{\text{cond,float}} + R_{\text{conv,water}}}\right) \tag{2.24}$$

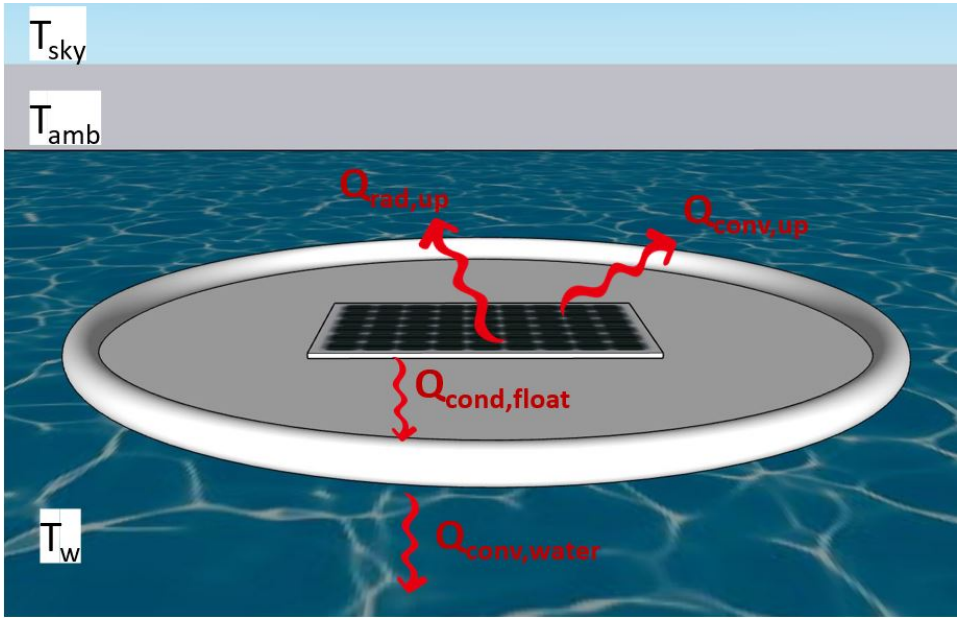


**Figure 2.17:** Heat Transfer Mechanisms for Floating PV with HPIT Configuration

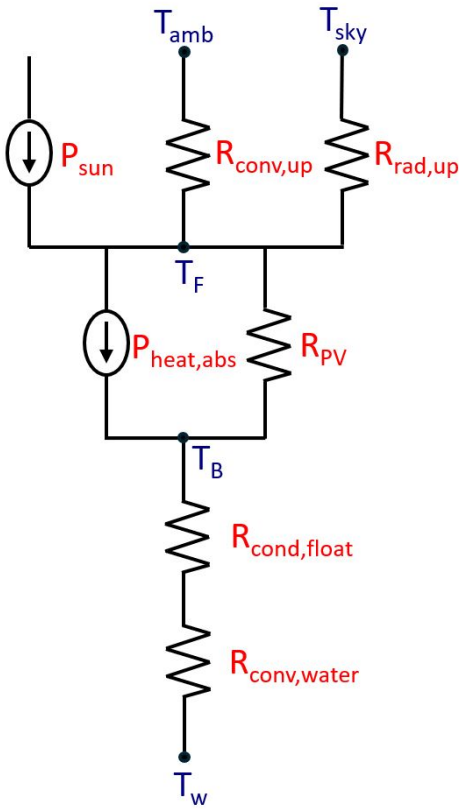


**Figure 2.18:** Heat Transfer Mechanisms for Floating PV with Membrane Ring Configuration

In summary, the resistive thermal model was developed for three representative floating PV configurations: HPOT, HPIT, and membrane ring by constructing equivalent thermal circuits and deriving their corresponding energy balance equations. These equations capture heat transfer mechanisms specific to the physical structure and water exposure characteristics of each archetype. The resulting ordinary differential equations (ODEs) represents the thermal response of the PV module's front and back surfaces, represented by $T_F$ and $T_B$.

To compute the values of $T_F$ and $T_B$, the energy balance equations were numerically solved using the $ode45$ solver in MATLAB. This solver is based on a Runge-Kutta method with adaptive step sizing, and was selected because of its robustness in solving ODEs. The simulations were based on environmental input parameters, which include ambient temperature, water temperature, irradiance, and wind speed, collected from measurement datasets across several regions. Through this approach, the model can be tested under realistic weather conditions to finally evaluate the model's PV module temperature prediction accuracy.

### 2.2.2. Applying Resistive Thermal Model and Fuentes Thermal Model to Floating PV Systems

In this section, the Resistive Thermal Model developed in sub-chapter 2.2.1 is implemented across the same set of floating PV configurations previously evaluated using the Fuentes Thermal Model. These configurations include HPOT systems with varying floater footprints, HPIT, and the membrane ring floating structure. The purpose of this implementation is to assess whether the resistive thermal model can improve the accuracy of PV module temperature predictions in floating PV systems. By applying the model consistently across different mounting archetypes, it is possible to evaluate a direct comparison with previous results from Fuentes Thermal Model presented in sub-chapter 2.1.3.

Before proceeding to the implementation for different floating PV archetypes, the Resistive Thermal Model is implemented for the base case study of Rahaman et al. [28]. The results of applying Resistive Thermal Model for the base case study is given in figure 2.19. The measured PV module temperatures are denoted by the black line, while the computed PV module temperatures from Fuentes Thermal Model and Resistive Thermal model are denoted by blue plus points and orange cross points, respectively.

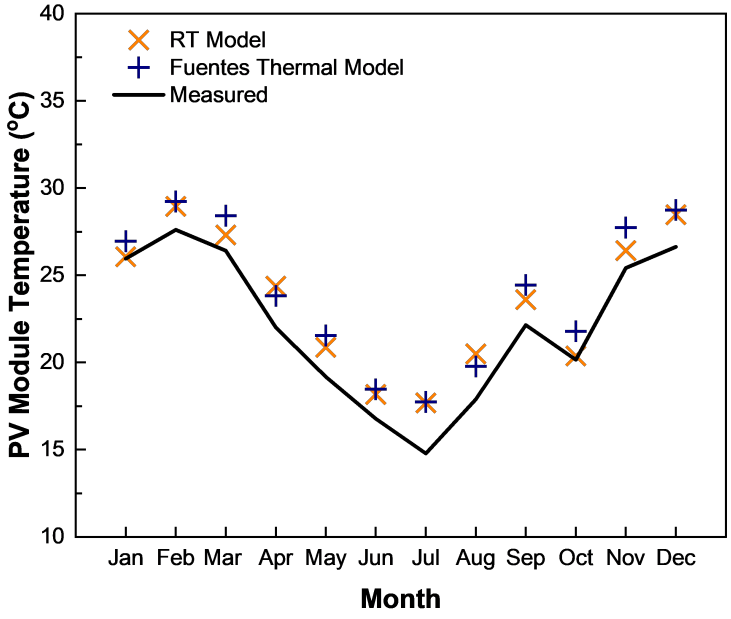


**Figure 2.19:** Resistive vs Fuentes Thermal Model PV Module Temperature Comparison for Base Case Study

From the comparison graph in fig 2.19, it can be observed that in general for the most data points in the year, the Resistive Thermal Model results in a lower PV module temperature compared to the results from Fuentes FD Model. The Resistive Thermal Model results are also showing less deviation from the measured PV module temperatures. The accuracy is quantified by the RMSE value of $1.70^oC$ and MAE of $1.37^oC$. For comparison, findings from the previous sub-chapter revealed that using the Fuentes Thermal Model, the RMSE is found to be $2.03^oC$ and the MAE is $1.82^oC$. These results shows an accuracy improvement compared to the error values from Fuentes Thermal Model, which clearly indicates that the Resistive Thermal Model more accurately represents the physical and thermal behaviour of the floating PV system. By tailoring the heat transfer path, specific to the floating PV configuration, each heat dissipation mechanism can be incorporated in more detail, compared to the approach in Fuentes FD Model.

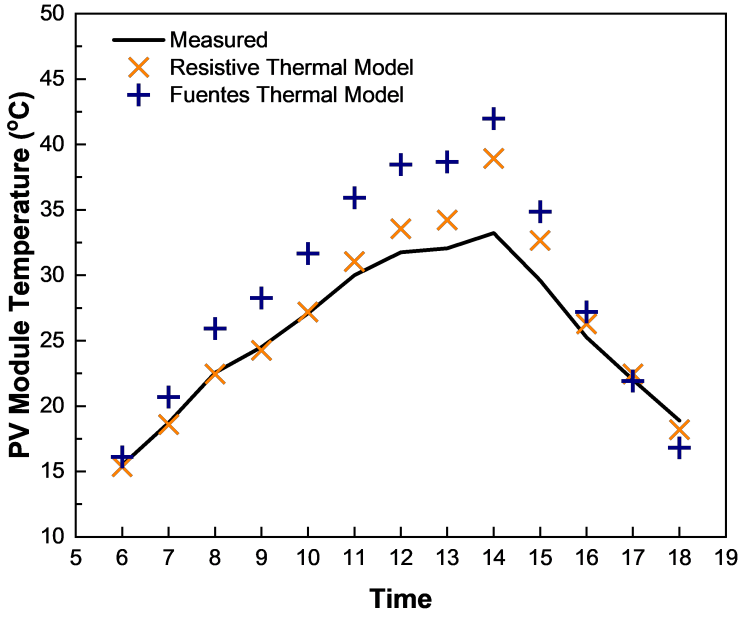


**Figure 2.20:** Fuentes vs Resistive Thermal Model PV Module Temperature Comparison for HPOT with Large Floater Footprint

Next, in line with the approach in the previous sub-chapter, an extended study for the other floating PV archetypes is done to have a more comprehensive analysis of how the Resistive Thermal Model performs in different floating PV applications. Figure 2.20 presents the comparison of PV module temperature result for the HPOT configuration with large floater footprint between Resistive Thermal Model and the Fuentes Thermal model. The resistive thermal model results, shown as orange cross signs, closely follow the measured PV module temperature trend throughout the day. The model captures the temperature increase in the morning, peaking during the midday between 13:00 and 14:00 and decreasing during afternoon hours. Not only capturing the general trend of the PV module temperature, the Resistive Thermal <odel shows smaller deviations with respect to the measured PV module temperature values compared to the Fuentes Thermal Model.

Quantitatively, the Resistive Thermal Model achieves a RMSE of $2.01^oC$ and a MAE of $1.28^oC$, significantly lower than Fuentes Thermal Model results with $4.70^oC$ and $3.97^oC$ of RMSE and MAE, respectively for the same configuration. The Fuentes Thermal Model results, shown in blue plus signs, consistently overestimates PV module temperatures, especially from late morning to early afternoon. In contrast, the Resistive Thermal Model benefits from its layered thermal resistance approach, allowing for a more realistic representation of heat transfer pathways, including front and back-side convection, radiative heat dissipation, and internal PV module conduction. This result shows that the Resistive Thermal Model has higher accuracy in capturing thermal behaviour of floating PV systems with large

floater footprints and highlights its potential as a more accurate and flexible thermal model for diverse floating PV configurations.

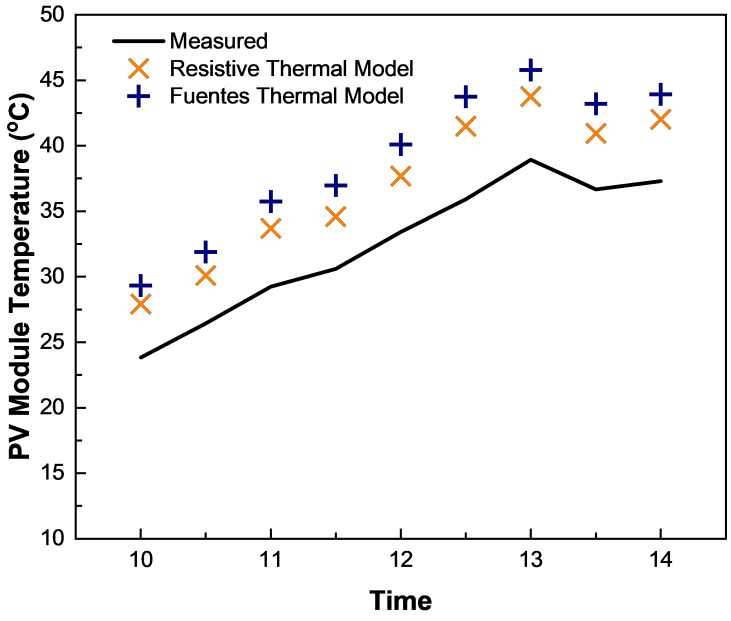


**Figure 2.21:** Fuentes vs Resistive Thermal Model PV Module Temperature Comparison for HPOT with Medium Floater Footprint

The second archetype is HPOT with medium floater footprint. Here, the floater covers a less amount of area under the PV module, hence allowing more water exposure on the backside of the PV module. Figure 2.21 presents the comparison of PV module temperatures predicted by the Resistive Thermal Model and the Fuentes Thermal Model against measured values for the HPOT configuration with a medium floater footprint, located in South Africa. The Resistive Thermal Model predictions, shown as orange cross signs, capture the overall trend of the measured temperatures reasonably well, including the steady increase throughout the day and the peak near 13:00. However, while the curve pattern is accurate, similar to the analytical fluid dynamics model, the resistive thermal model results in a consistent overestimation of the PV module temperature values with deviation reaching up to $5^oC$ during peak sun hours.

The overall deviation can be quantified by the error metrics RMSE of $4.46^oC$ and MAE of $4.43^oC$. Desite these moderate amount of error values, Resistive Thermal Model still outperforms the Fuentes Thermal Model for this configuration, which previously showed and RMSE of $6.52^oC$ and MAE of $6.48^oC$. The improvement suggests that the resistive thermal model gives a more realistic representation of the heat transfer processes, mainly by incorporating relevant convective heat transfer and conduction effects from the PV module, affected by the water surface. Nonetheless, the error is still relatively high, this may be caused still by some inaccurate assumptions for several heat transfer coefficients. Overall, while not as accurate as in the large floater footprint case, the Resistive Thermal Model still provides a notable improvement over the Fuentes Model in predicting PV module temperature values.

The third archetype is the HPOT with a small floater footprint. In this configuration, the floater covers an even lesser amount of area under the PV module, hence allowing a large water exposure on the backside of the PV module. Figure 2.22 displays the comparison between PV module temperatures predicted by the resistive thermal model, the Fuentes Thermal Model, and the measured values for the HPOT configuraton with a small floater fooptrint, located in Singapore. Consistent with previous findings, the Resistive Thermal Model results, shown as orange cross signs, follow the trend of the measured data fairly well. The model captures the temperature rise in the morning, the midday peak, and

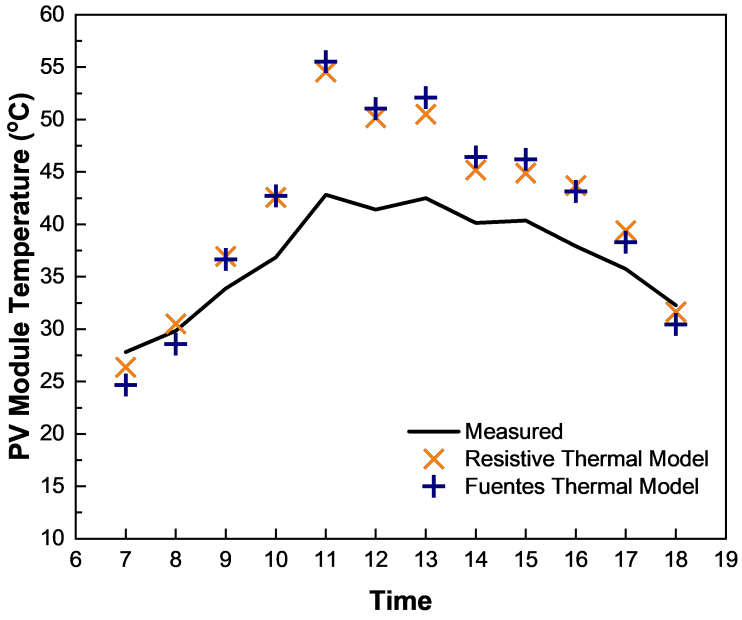


**Figure 2.22:** Fuentes vs Resistive Thermal Model PV Module Temperature Comparison for HPOT with Small Floater Footprint

the afternoon decreasing phase. However, during peak irradiance hours, especially between 11:00 and 15:00, the Resistive Thermal Model still tends to overestimate the PV module temperature, although to a lesser extent compared to the Fuentes Thermal Model.

For this floating PV configuration, the Resistive Thermal Model yields a RMSE of $5.89^oC$ and a MAE of $4.92^oC$, which represent a notable improvement compared to the Fuentes Thermal Model with the RMSE of $6.53^oC$ and MAE of $5.56^oC$. Similar to the previous configuration, while benefitting from the more detailed thermal resistance framework, the relatively high error suggests that additional factors such as the assumption of heat transfer coefficients due to high water exposure may still be inadequately incorporated. Unlike in the larger floater footprint case, where the floater limits convective cooling, this configuration presents a greater modelling distinction do to its open underside and higher interaction with ambient airflow that is affected by the presence of water surface. Although the Resistive Thermal Model improves upon the Fuentes Thermal Model in terms of accuracy, it still shows limitations in capturing thermal behaviour, especially for high water-exposure floating PV systems. These results highlight the need for further refinements of relevant heat transfer coefficients that is used in the model.

The next archetype is the HPIT with small floater footprint. As discussed in the previous section, in this configuration, instead of using rectangular pontoons, cylindrical pipes are used as floaters to keep the PV module bouyant above the water surface. Figure 2.23 compares the PV module temperatures predicted by the Resistive Thermal model and the Fuentes Thermal Model against measured values for the HPOT configuration with a small floater footprint, located in the Netherlands. The Resistive Thermal Model results, shown as orange cross signs, demonstrate an observable improvement over the Fuentes Thermal Model denoted by blue plus signs. The Resistive Thermal Model results closely follow the measured curve's shape and better align with measured PV module temperature values, though some overestimation can still be observed around peak irradiance hours.

The Resistive Thermal Model yields a RMSE of $5.48^oC$ and a MAE of $3.83^oC$, outperforming the Fuentes Thermal Model which had an RMSE of $7.05^oC$ and MAE of $6.17^oC$. Again, while the Resistive Thermal Model notably improves the PV module temperature predictions over the Fuentes Thermal Model for HPIT configuration, it still does not represent some of the dynamic cooling mechanisms in small floater

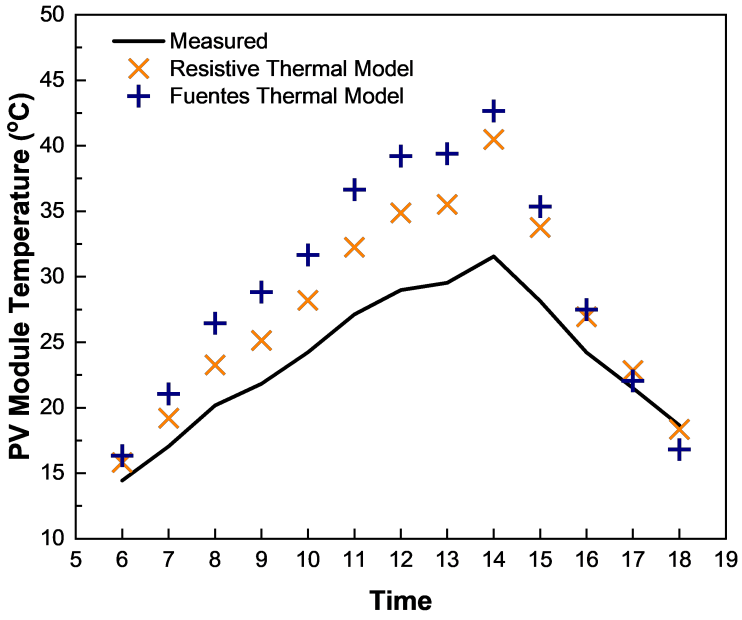


**Figure 2.23:** Fuentes vs Resistive Thermal Model PV Module Temperature Comparison for HPIT with Small Floater Footprint

footprint systems. These results reinforce the importance of including detailed modelling approach for distinct water and airlow-induced convective heat transfer coefficients that might be able to be solved using a more advanced computational fluid dynamics method.

Lastly, the Resistive Thermal Model is applied for membrane ring floating PV configuration. Figure 2.24 presents the comparison between the Resistive Thermal Model, Fuentes Thermal Model, and the measured PV module temperatures for the membrane ring configuration, for a floating PV installation located in Norway. In this unique floating PV structure, the PV module is mounted directly above a thin and flexible membrane with minimal to no air gap under the backside of the module, significantly limiting backside convective cooling. The Resistive Thermal Model, shown in orange cross signs, demonstrates a notable improvement in capturing the temperature profile compared to the results of Fuentes Thermal Model denoted by blue plus signs. The Resistive Thermal Model captures the diurnal pattern of the temperature curve and more closely aligns with the measured values, particularly during high irradiance conditions.

Quantitatively, the Resistive Thermal Model achieves a RMSE of $3.49^oC$ and a MAE of $3.19^oC$. These results show a significant improvement over the analytical fluid dynamics model which previously showed an RMSE of $10.07^oC$ and MAE of $8.97^oC$. These findings highlights the benefit of explicitly modelling heat transfer resistances in scenarios where conventional convective assumptions are not applicable, such as in the membrane ring system where airflow beneath the PV module is effectively absent. By accounting for limited convection and the dominant role of conduction through the mounting surface, the Resistive Thermal model is better suited to represent the thermal behaviour of this configuration.

Figure 2.25 summarizes the RMSE values obtained from both the Resistive Thermal Model and the Fuentes Thermal Model across six floating PV configurations analyzed in this chapter. The comparative results clearly demonstrate the improvement of PV module temperature prediction offered by the resistive thermal model with lower RMSE values across all cases. For the HPOT configuration with large floater footprint, the Resistive Thermal Model achieves the lowest error of $2.01^oC$, outperforming the Fuentes Thermal Model which yields an RMSE of $4.07^oC$. These results shows the Resistive Thermal Model's effectiveness in conditions where convective and radiative assumptions have more

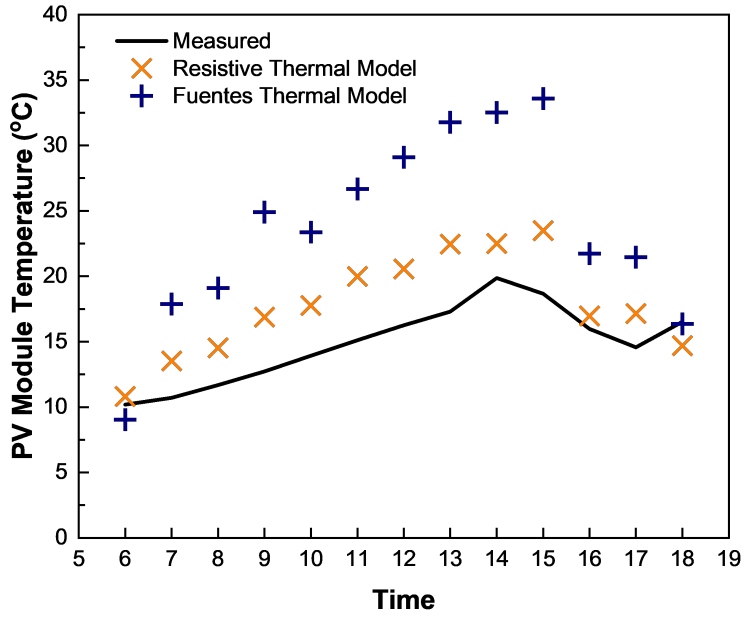


**Figure 2.24:** Fuentes vs Resistive Thermal Model PV Module Temperature Comparison for Membrane Ring Floating PV

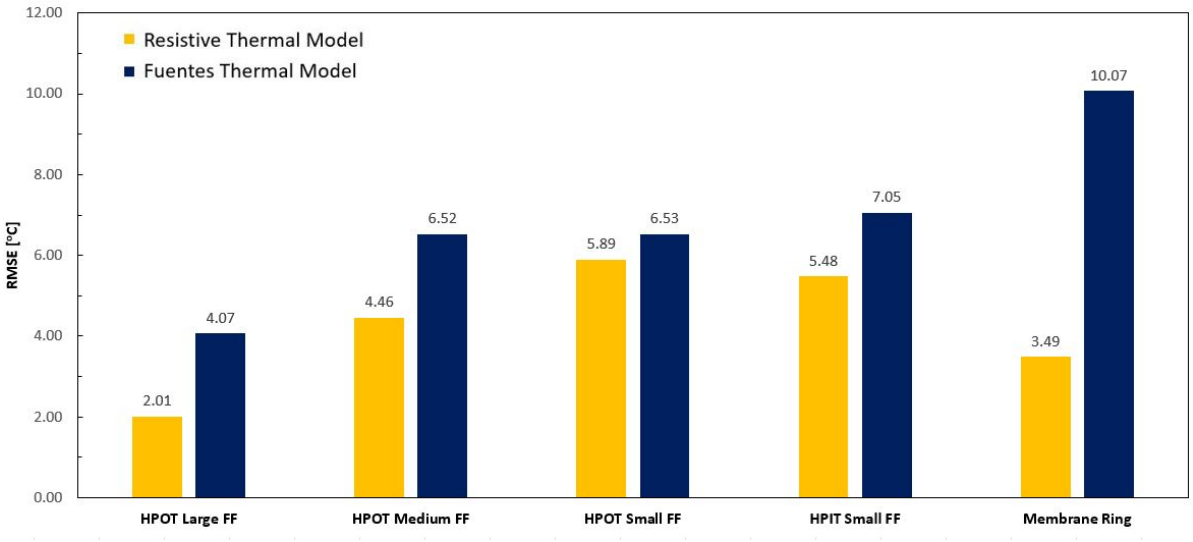


**Figure 2.25:** Summary of PV Module Temperature Comparison between Resistive Thermal Model and Fuentes Thermal Model

similarity to land-based systems, with large portion of the water covered by the floating structure that leads to minimal water exposure.

In configurations with medium and small floater footprints such as HPOT medium FF (Floater Footprint), HPOT small FF, and HPIT small FF, the Resistive Thermal Model also shows consistent improvement over the Fuentes Thermal Model, reducing the RMSE by approximately $1$ to $2^oC$ in each case. However, the RMSE values are generally higher in these systems, indicating larger thermal modelling complexity due to stronger air-water interactions, posing a more distinct convective cooling behaviour. For membrane ring configuration, though, the Resistive Thermal Model significantly reduces the RMSE from $10.07^oC$ to $3.49^oC$. This reinforces the importance of explicitly modelling conductive heat dissipation pathways when conventional convective cooling is severely limited, as in the case for membrane ring where lack of air gap beneath the module occurs.

The trend across all cases suggests that while the Resistive Thermal Model is more robust and adaptable than the Fuentes Thermal odel, its accuracy is still influenced by configuration-specific thermal behaviour. These discrepancies highlight the need to further refine thermal modelling inputs based on the physical characteristics of the floating system being analyzed.

## 2.3. Analysis on Key Thermal Modelling Parameters for Floating PV

To further improve the predictive accuracy of the Resistive Thermal Model, it is essential to first identify and refine key parameters that differentiate thermal behavior across floating PV archetypes. Parameters such as conductive, convective, and radiative heat transfer coefficients, need to be carefully adjusted for each floating PV configuration. Identifying and adjusting the key heat transfer coefficient is extremely important, and directly affects the thermal model's prediction accuracy. This is an essential step in addressing the main research objective, which is to develop an improved thermal model specific to floating PV applications.

To address this, this sub-chapter explores the key parameters that differentiate floating PV systems from land-based systems and the extent of how much it contributes to the observed PV module temperature. By identifying and performing a sensitivity analysis on these parameters, the aim is to quantify their individual influence on temperature prediction accuracy and provide a basis for model refinement using computational fluid dynamics method in chapter 3.

### 2.3.1. Identifying Key Parameters

As discussed previously, the governing equation for Resistive Thermal Model is given by (2.19) and (2.20), while the Fuentes Thermal Model is governed by equation (2.6). From these equations, it is found that both the Resistive Thermal Model and Fuentes Thermal Model are based on the same three heat transfer mechanisms: conduction, convection, and radiation. In addition to these, incident power from the sun's irradiance is also taken into account in both models. The Fuentes Thermal Model, however, does not take into account the conduction through the floating structure to the water, while the Resistive Thermal Model does. To identify which parameter should be modified to incorporate different archetype to the model, each heat transfer component will be analyzed in this section.

Firstly, the incident power from the sun's irradiance is expressed as shown in Equation (2.7). This power is influenced by the plane-of-array irradiance $G_{POA}$ and the optical properties of the PV module's front surface, specifically its transmissivity and absorptivity $\alpha$. he transmissivity and absorptivity are inherent material properties of the PV module's front surface, while $G_{POA}$ is an environmental parameter that varies with solar conditions. Since these factors are independent of the floating PV archetype, their values remain unchanged across different system configurations.

Next, convective heat transfer occurs on both the upper and backside surfaces of the PV module. The convective heat transfer coefficient is a key factor governing this process, as it directly influences the rate of heat dissipation from the module to its surroundings. As described in Equation (2.13), the convective heat transfer coefficient is a function of the Nusselt number, air thermal conductivity, and PV module length. Among these parameters, **the Nusselt number is the key variable that can be adjusted to account for different floating PV archetypes.**

Nusselt number is a dimensionless quantity that describes the relative importance of convective heat transfer compared to conductive heat transfer in a fluid. A higher Nusselt number indicates stronger convection relative to conduction, meaning heat is more effectively transferred away from the PV module surface. The Nusselt number is typically determined using empirical correlations derived from experimental data and theoretical analysis. These correlations depend on the fluid flow regime (laminar or turbulent), geometry of the heated surface, and type of convection (natural or forced) [36].

In floating PV systems, the Nusselt number formulation must be modified to account for differences in system configurations. These variations arise due to the mounting structure design, where modules may be fully floating, partially submerged, or elevated, each affecting airflow patterns. Additionally, water proximity effects play a role, as floating PV modules are closer to the water surface, altering the convective cooling mechanisms due to heat exchange with both air and water. Furthermore, wind conditions and orientation impact the heat transfer mechanism by influencing whether forced or mixed convection dominates.

The radiative heat transfer, as described in Equation (2.8), depends on the emissivity of the PV module's front and back surface $\epsilon_{back}$, the Stefan-Boltzmann constant $\sigma$, and the view factor $\psi$ of the PV module relative to its surroundings. Specifically, the upper surface view factor represents the module's exposure to the sky, while the backside view factor accounts for its exposure to the water surface.

The emissivity is an intrinsic material property of the PV module's front and back surfaces, meaning it remains constant regardless of the floating PV archetype. Similarly, the Stefan-Boltzmann constant $\sigma$ is a universal physical constant that defines the total energy radiated by a black body and is independent of system configuration. Since these two parameters are fundamental physical properties, they do not vary across different floating PV designs.

However, the backside view factor does change depending on the water exposure at the rear surface of the PV module. This factor is directly influenced by the floating system's water footprint, which determines the fraction of the water surface that remains uncovered by the floating structure. A large floater footprint corresponds to a greater portion of the water surface being covered by the floater, reducing the amount of exposed water and thereby lowering the backside view factor. In this case, radiative heat exchange with the water is limited due to obstructed exposure. On the other hand, a small floater footprint means that only a small portion of the water surface is covered by the floater, allowing for greater exposure of the PV module's backside to the water. This results in a higher backside view factor, meaning that a larger portion of the module's thermal radiation interacts with the water surface.

Since different floating PV archetypes vary in their structural design and floater coverage, their corresponding **backside view factors must be adjusted accordingly to accurately model the radiative heat exchange process.**

Lastly, the conduction heat transfer through the floating structure also varies across different floating PV archetypes. As defined in Equation (2.16), the conductive resistance is primarily influenced by two factors: the distance between the PV module and the water surface ($L$) and the contact area between the module and the floater ($A$).

The distance between the PV module and the water surface ($L$) plays a crucial role in determining conductive heat transfer, as it affects the thermal pathway between the module and the water. According to [29], the proximity of the PV module relative to the water surface can be classified into three categories. Low elevation ($L < 1m$) refers to PV modules positioned close to the water surface, resulting in strong conductive dissipation and lower conductive resistance. Moderate elevation ($1m \leq L < 2m$) represents a balanced configuration where conduction still occurs, but its effect is less significant than at lower elevations. High elevation ($2m \leq L \leq 3m$) places the modules farther from the water, leading to high conductive resistance, which significantly reduces conduction-driven heat dissipation.

In summary, incorporating different floating PV archetypes into the model requires adjusting key parameters, which are the Nusselt number for convective heat transfer, the back-side view factor for radiative heat transfer, and the distance between the PV module and the water surface for conductive heat transfer through the floating structure. To assess the impact of each parameter on the overall thermal behavior, a sensitivity analysis is conducted in this sub-chapter, providing insights into their relative influence on the PV module temperature deviations.

### 2.3.2. Sensitivity Analysis for Key Parameters

To evaluate the influence of the identified parameters on floating PV thermal behavior, a sensitivity analysis is conducted using the one-at-a-time (OAT) method. This approach involves varying one parameter at a time while keeping the others constant, allowing for a clear assessment of each parameter's individual impact on PV module temperature. The OAT method is chosen due to its simplicity and effectiveness in isolating the effects of specific variables without introducing interactions between them [37], making it particularly suitable for analyzing systems with well-defined parameter dependencies. The base line scenario of the sensitivity analysis is given by table 2.2.

To further quantify the relative impact of each identified heat transfer parameter on the PV module temperature predictions, a normalized sensitivity index is used. The normalized sensitivity index is a dimensionless metric that expresses the change in model output (PV module temperature) per unit change in a given input parameter, normalized by the range or nominal value of that parameter. Mathematically, it can be expressed as:

$$\text{NSI} = \frac{\Delta T_{\text{mod}}/T_{\text{mod,ref}}}{\Delta X/X_{\text{ref}}} \tag{2.25}$$

In this equation, $\Delta T_{\text{mod}}$ represents the change in predicted PV module temperature resulting from a variation $\Delta X$ in the input parameter $X$. The terms $T_{\text{mod,ref}}$ and $X_{\text{ref}}$ are the reference (baseline) values of the PV module temperature and the input parameter, respectively. By normalizing both the input variation and the corresponding output response, the normalized sensitivity index enables a direct comparison of sensitivities across different parameters, regardless of their physical units or magnitudes [38]. This makes it a useful metric for identifying which parameters have the most significant influence on thermal behavior. In this study, the normalized sensitivity index is calculated for each of the key parameters identified in the previous sub-section, using the baseline scenario defined in Table 2.2.

**Table 2.2:** Base Case Parameters

| Parameter | Value | Unit |
|---|---|---|
| Plane-of-Array Irradiance ($G_{POA}$) | 800 | W/m$^2$ |
| Ambient Temperature ($T_{amb}$) | 25 | °C |
| Water Temperature ($T_w$) | 25 | °C |
| Forced Convection Nusselt Number | 600 | - |
| Free Convection Nusselt Number | 57 | - |
| PV Back Side View Factor ($\phi$) | 1 | - |
| PV to Water Distance ($L$) | 0.1 | m |

The first parameter adjusted in the sensitivity analysis is the forced convection Nusselt number, which is varied within the range of 200 to 3000 in increments of 200. This range is chosen to encompass both low and high convective heat transfer scenarios, capturing the effects of weak to strong forced convection on PV module cooling. The lower bound (Nu=200) represents conditions with minimal forced convection, where heat dissipation primarily relies on natural convection and radiation. The upper bound (Nu=3000) corresponds to high-wind conditions or strong airflows, significantly enhancing convective cooling. The step size of 200 ensures a sufficient resolution for observing trends in PV module temperature without excessive computational effort. The resulting effect of varying the forced convection Nusselt number on PV module temperature is presented in Figure 2.26.

The sensitivity analysis results, presented in Figure 2.26, illustrate the relationship between the forced convection Nusselt number and the PV module temperature for both the resistive thermal model and the fluid dynamics model. As the Nusselt number increases, the PV module temperature decreases, highlighting the enhanced cooling effect with higher convective heat transfer. Initially, at low Nusselt numbers, a sharp decline in temperature is observed, indicating that forced convection significantly improves cooling in this regime. However, as the Nusselt number continues to rise beyond approximately 1000, the rate of temperature reduction slows down, suggesting less significant cooling effect from increased convection.

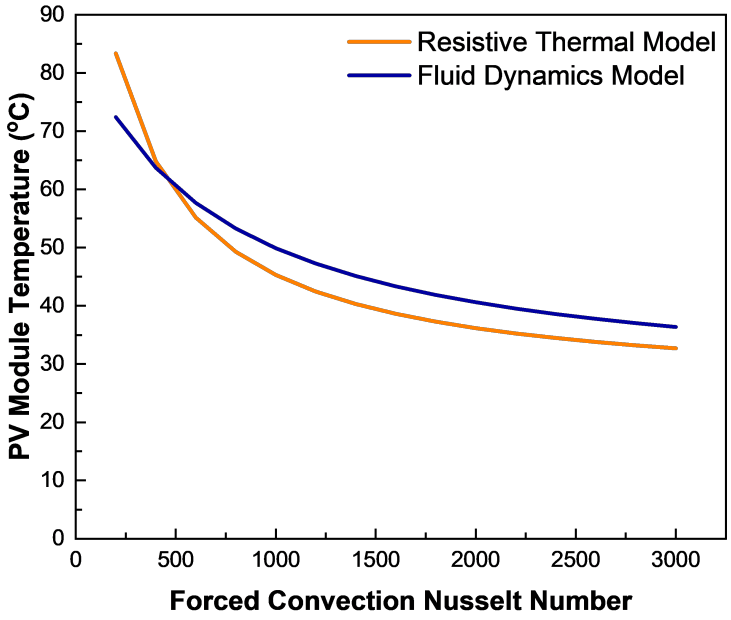


**Figure 2.26:** Sensitivity Analysis Result for Forced Convection Nusselt Number on PV Module temperature

As mentioned, to quantify the extent to which the forced convection Nusselt number affects PV module temperature, the normalized sensitivity index is used. The average sensitivity index for the resistive thermal model is found to be 0.271, with a peak sensitivity index of 0.322. Similarly, for the fluid dynamics model, the average sensitivity index is also 0.271, but with a slightly lower peak value of 0.274. These values indicate that while both models exhibit a comparable overall sensitivity to forced convection, the resistive thermal model demonstrates a slightly stronger peak response to changes in the Nusselt number.

The next parameter adjusted in the sensitivity analysis is the backside view factor ($\phi$), which is varied from 1.0 to 0.1 in increments of 0.1 A view factor of 1.0 represents a condition where the PV module has maximum exposure to the water surface, corresponding to a small water footprint with minimal floater coverage. In contrast, a view factor of 0.1 indicates minimal exposure to the water surface representing a large water footprint where a significant portion of the water is covered by the floating structure. This range is selected to capture both extreme and intermediate configurations of floating PV systems, ensuring that the analysis consider the full spectrum of potential thermal interactions. The step size of 0.1 provides a sufficiently detailed resolution to observe trends in temperature variation.

The sensitivity analysis results for the PV module backside view factor, as shown in Figure 2.27, illustrate the relationship between the view factor and PV module temperature for both the resistive thermal model and the fluid dynamics model. Unlike the forced convection Nusselt number, which exhibited a strong inverse relationship with temperature, the backside view factor demonstrates a positive correlation with PV module temperature. As the view factor decreases from 1.0 to 0.1, meaning the floater covers more of the water surface and reduces radiative heat exchange with the water, the PV module temperature gradually increases.

This trend highlights the role of radiative cooling from the water surface in the thermal behaviour of floating PV systems. When the backside view factor is high ($\phi = 1.0$), a large portion of the PV module's backside is exposed to the water, allowing for greater radiative heat dissipation, which helps lower the module temperature. Conversely, when the backside view factor is low ($\phi = 0.1$), a large water footprint (floater coverage) reduces water exposure, limiting radiative heat loss and causing the module to retain more heat, resulting in a higher operating temperature.

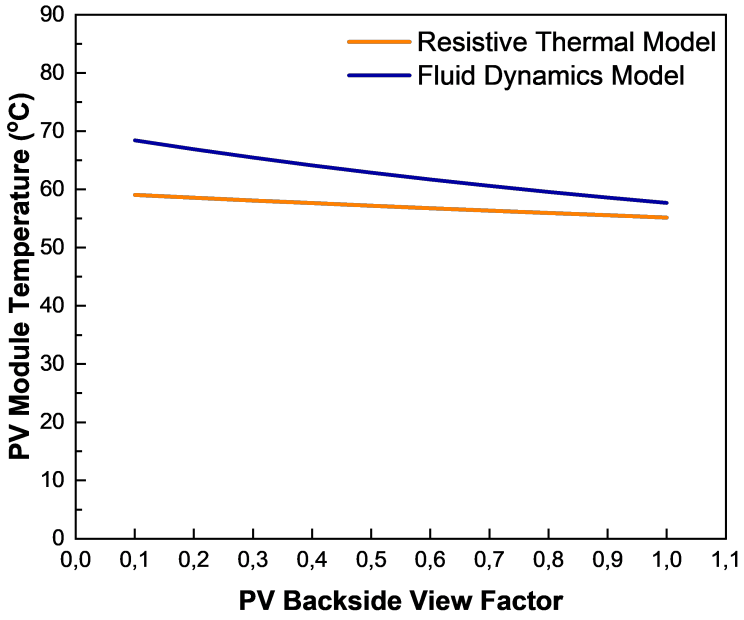


**Figure 2.27:** Sensitivity Analysis Result for Back Side View Factor on PV Module temperature

To quantify the influence of this parameter, the normalized sensitivity index is used. For the resistive thermal model, the average sensitivity index is 0.044, with a peak sensitivity of 0.071, indicating a relatively minor impact on temperature variation. In contrast, the fluid dynamics model exhibits a higher sensitivity, with an average sensitivity index of 0.109 and a peak of 0.160, demonstrating that radiative interactions with the water surface are more significant in this model.

Lastly, the distance between the PV module and the water surface ($L$) is adjusted as part of the sensitivity analysis. This parameter plays a crucial role in defining the conductive heat transfer pathway between the PV module and the floating structure. It is important to note, though, the effect of the water proximity only captured by the resistive thermal model as conduction heat dissipation through the mounting structure. In reality, water proximity also influence the convective and radiative interactions with the surrounding environment. This effect will be incorporated in the model through the adjusment of the Nusselt number.

The range of $L$ is varied from 0.25 m to 3 m in increments of 0.25 m, allowing for a detailed evaluation of different floating PV elevation scenarios. A small elevation ($L \approx 0.25m$) represents close proximity to the water, where conduction through the floater and radiative exchange with the water surface are dominant. A moderate elevation ($L \approx 1 - 2m$) provides a balance between conductive and convective heat transfer, with reduced direct heat dissipation to the water. Meanwhile, a high elevation ($L \approx 3m$) significantly reduces conductive cooling effects, making convection the primary heat dissipation mechanism.

The sensitivity analysis results for PV module proximity to the water surface (L), as shown in Figure 2.28, reveal a minimal impact of this parameter on module temperature. In the resistive thermal model, a slight increase in module temperature is observed as L increases, while in the fluid dynamics model, the temperature remains constant regardless of L.

This trend can be explained by the role of conductive heat transfer in the thermal regulation of floating PV systems. In the RT model, conductive heat dissipation occurs between the PV module, the floating structure, and the water, meaning that a shorter distance enhances conduction and helps lower module temperature. However, as the distance increases, conduction becomes less effective, and module temperature rises slightly. The impact, however, is very small compared to other heat transfer

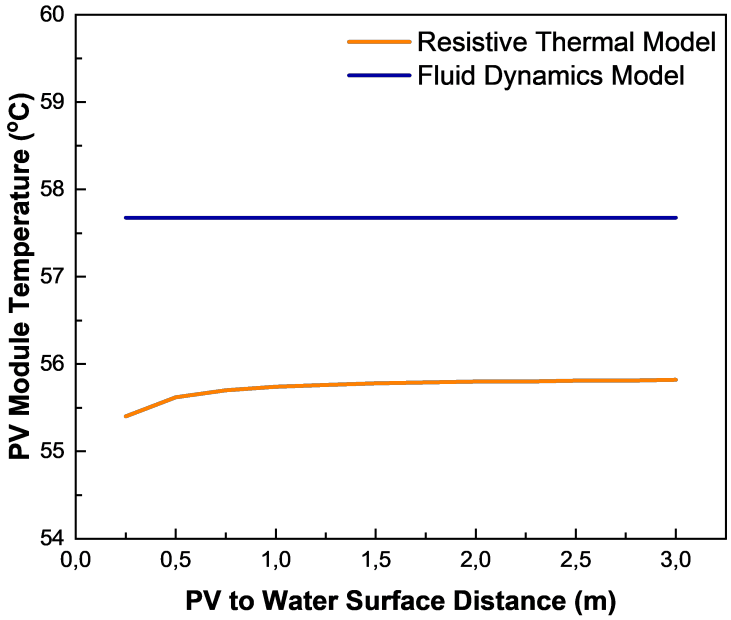


**Figure 2.28:** Sensitivity Analysis Result for PV Module to Water Surface Distance on PV Module temperature

mechanisms, as seen in the shallow slope of the resistive thermal model curve.

For the fluid dynamics model, the insensitivity to L is expected because the fluid dynamics approach does not account for conduction through the floating structure. Instead, it primarily considers convective and radiative heat transfer, which remain unaffected by module elevation relative to the water surface. As a result, PV module temperature remains unchanged in this model, regardless of variations in L.

To quantify the influence of water proximity, the normalized sensitivity index is used. For the resistive thermal model, the average sensitivity index is 0.001, with a peak sensitivity index of 0.002, indicating a negligible effect on module temperature. In contrast, for the fluid dynamics model, L has no direct impact, as conduction is not included in the heat transfer mechanisms considered. This confirms that module elevation relative to the water surface is not a major determinant of PV module temperature unless conductive pathways play a significant role in the system design.

**Table 2.3:** Sensitivity Analysis Summary

| Parameter | Average Normalized Sensitivity Index | | Peak Normalized Sensitivity Index | |
|---|---|---|---|---|
| | Resistive Thermal Model | Fluid Dynamics Model | Resistive Thermal Model | Fluid Dynamics Model |
| Forced Convection Nusselt Number | 0.271 | 0.245 | 0.322 | 0.274 |
| PV Module Backside View Factor | 0.044 | 0.109 | 0.071 | 0.160 |
| Distance from PV Module to Water | 0.001 | 0 | 0.002 | 0 |

The sensitivity analysis summary, as presented in Table 2.3, highlights the influence of the forced convection Nusselt number, backside view factor, and PV module distance from the water surface on the module temperature. Among these parameters, the forced convection Nusselt number exhibits the highest normalized sensitivity index for both the Resistive Thermal <odel and the Fuentes Thermal odel. This indicates that **convective heat transfer plays a dominant role in determining the thermal behavior of floating PV systems**. The backside view factor also influences module temperature, particularly in the Fuentes Thermal Model, where radiative heat transfer interactions with the water surface are considered. However, the impact of PV module elevation (L) is found to be negligible, as conductive heat transfer through the floating structure is minimal or absent in the FD model.

Given the strong influence of the Nusselt number on PV module temperature, it is crucial to improve

its estimation by updating the Nusselt number correlation to comprehensively incorporate heat transfer mechanisms and accurately represent the thermal behavior of different FPV designs. A suitable approach for refining the Nusselt number correlation is through Computational Fluid Dynamics (CFD) simulations. CFD allows for a detailed analysis of fluid flow and heat transfer around the PV module, capturing the effects of different floating PV configurations, wind speeds, and turbulence characteristics.

Using CFD method will enable the ability to model complex convective heat transfer interactions that cannot be easily represented by empirical correlations alone. CFD provides spatially resolved temperature and velocity fields, enabling the derivation of more accurate Nusselt number correlations specific to different floating PV archetypes. This approach ensures that convective cooling mechanisms are well understood, leading to improved thermal modeling accuracy.

Therefore, in Chapter 3, the Nusselt number values for floating PV system will be studied using CFD simulations performed in ANSYS Fluent. This will provide a refined understanding of convective heat transfer mechanisms, by proposing an updated Nusselt number or convective heat transfer coefficient value for floating PV application.

## 2.4. Summary of the Key Findings in Chapter 2

In summary, this Chapter's objective is to address the first research question, that is to analyse how do analytical thermal models perform in predicting PV module temperatures for both floating and land-based PV systems. A systematic approach has been done to answer this research question. Firstly, the existing Fuentes Thermal Model is applied to both land-based and floating PV system. Next, an alternative model is developed, named Resistive Thermal Model. This newly-developed model is applied to the same floating PV installations and the predictive accuracy is compared for Fuentes Thermal Model and Resistive Thermal Model. Lastly, a sensitivity analysis is done to identify key parameters that is necessary to be modified, specific to floating PV conditions.

In this chapter, it is revealed that the Fuentes Thermal Model predicts the PV module temperatures of land-based system with good accuracy. However, for floating PV system, applying Fuentes Thermal Model to floating PV systems result in a relatively low accuracy, with RMSE value of $2.30^oC$ for the base case study.

Resistive Thermal Model has been successfully developed for diverse floating PV configurations, namely Horizontal Pontoon with Truss (HPOT), Horizontal Pipe with Truss (HPIT), and Membrane Ring floating PV. Applying the Resistive Thermal Model to these floating PV archetypes revealed that relative to Fuentes Thermal Model, Resistive Thermal Model results in a better accuracy across all assessed floating PV configurations. For the base case study, the RMSE of Resistive Thermal Model decreases further to $1.70^oC$. These findings shows a notable improvement of the prediction accuracy of analytical thermal models. However, relatively high RMSE values can still be observed even with Resistive Thermal Model, particularly in high water-exposure floating PV systems.

Three key heat transfer coefficients has been identified, which are the Nusselt number that represents convective heat transfer, PV module backside view factor that represents radiative heat transfer, and PV to water distance that represent conductive heat transfer. The sensitivity analysis for each of these parameters revealed that the forced convection Nusselt number exhibits the highest normalized sensitivity index for both the Resistive Thermal Model and the Fuentes Thermal Model. This indicates that convective heat transfer plays a dominant role in determining the thermal behavior of floating PV systems.

Given the strong influence of the Nusselt number on PV module temperature, it is crucial to improve its estimation by updating the Nusselt number correlation to comprehensively incorporate heat transfer mechanisms and accurately represent the thermal behavior of different FPV designs. A suitable approach for refining the Nusselt number correlation is through Computational Fluid Dynamics (CFD) simulations. CFD allows for a detailed analysis of fluid flow and heat transfer around the PV module, capturing the effects of different floating PV configurations, wind speeds, and turbulence characteristics.

Therefore, in Chapter 3, the Nusselt number values for floating PV system will be studied using CFD

simulations performed in ANSYS Fluent. This will provide a refined understanding of convective heat transfer mechanisms, by proposing an updated Nusselt number or convective heat transfer coefficient value for floating PV application.

# 3

# Computational Fluid Dynamics (CFD) Thermal Modelling for Floating PV Application

Chapter 3 aims to address the second research question, that is to analyse how can analytical thermal models be improved to better represent heat transfer mechanisms specific to floating PV systems. This question focuses on investigating the role of Computational Fluid Dynamics (CFD) in capturing detailed convective, conductive, and radiative effects influenced by water proximity and ambient cooling.

This chapter is structured to first introduce the role of computational fluid dynamics, and how it can be applied for floating PV system study cases. Next, validation processes are done to ensure that the CFD simulations comprehensively represent practical and real world physics and thermal interactions. Finally, case studies are done based on practical scenario and real-world floating PV installation. After conducting the simulations, key heat transfer coefficients are extracted to finally be used as an updated input for the Resistive Thermal Model to increase its PV module temperature prediction accuracy.

## 3.1. Introduction to Computational Fluid Dynamics for Floating PV Application

Computational Fluid Dynamics (CFD) is a numerical technique for solving fluid flow and heat transfer problems based on the fundamental governing equations of fluid mechanics and thermodynamics. In the context of floating PV systems, CFD enables detailed modeling of heat transfer between the PV module, the surrounding air, and the water surface below the PV module, capturing 2D and 3D spatial variations that are not easily addressed by simplified analytical thermal models.

In this chapter, CFD is utilized to simulate conjugate heat transfer (CHT) across the PV module and its environment. The results will be used to validate and update existing analytical thermal model that predicts PV module surface temperature. The intended outcome of the CFD simulations presented in this chapter is to derive heat transfer coefficients and their associated Nusselt numbers for various floating PV configurations. These values are specific to different floating PV archetypes, namely, systems with large, medium, and small water footprints. These proposed values will then be used to improve the accuracy of analytical thermal models in predicting the PV module surface temperature values, consequently, improving the prediction accuracy of energy yield modelling of floating PV systems.

### 3.1.1. ANSYS Fluent Governing Equations

CFD simulations in this study are performed using ANSYS Fluent, a widely used commercial CFD solver capable of being implemented in fluid flow and heat transfer applications. ANSYS Fluent provides robust numerical methods for solving the continuity equations, turbulence models, and energy equations, making it suitable for CHT analysis where heat transfert occurs between solid and fluid interfaces.

The simulations are based on solving a set of coupled partial differential equations: the continuity, momentum, and energy equations. These equations govern the conservation of mass, momentum, and energy within the fluid and solid domains.

Firstly, the continuity equation expresses the principle of mass conservation [39]. This equation depicts that mass is neither created nor destroyed within the fluid domain. For a compressible fluid, the continuity equation is written as

$$\frac{\partial \rho}{\partial t} + \nabla \cdot (\rho \vec{v}) = 0 \tag{3.1}$$

where $\rho$ is fluid density [kg/$m^3$], $\vec{v}$ is the velocity vector, and $t$ is the time in seconds.

In the case of floating PV, the fluids involved are air around the PV module and water below the floating structure. While air is technically compressible, under low speed airflow and small temperature changes, the density variation is negligible. Water, on the other hand, is incompressible. Therefore, both fluids are modeled as incompressible in the simulation. Consequently, under this assumption, the density $\rho$ is considered constant.

The momentum equation, also known as the Navier-Stokes equation, governs the behavior of fluid flow as a function of pressure, viscous forces, gravity, and external forces [40]. The general form of the equation is

$$\frac{\partial (\rho \vec{v})}{\partial t} + \nabla \cdot (\rho \vec{v} \vec{v}) = -\nabla p + \nabla \cdot \left[ \mu \left( \nabla \vec{v} + (\nabla \vec{v})^T \right) \right] + \rho \vec{g} + \vec{F} \tag{3.2}$$

where $p$ is pressure [$Pa$], $\mu$ is dynamic viscosity [$Pa.s$], $\vec{g}$ is the gravitational acceleration vector [$m/s^2$] and $\vec{F}$ is the body forces, derived from turbulence model source terms.

In this floating PV case, the momentum equations are also applied to both air domain and the water domain. Since both natural convection and forced convection occurs, the flow regime can be considered mixed convection. To account for these effects, ANSYS Fluent uses the Reynold-Averaged Navier-Stokes (RANS) equations together with a two-equation turbulence model $k - \epsilon$ RNG. The reasoning behind choosing turbulencce model $k - \epsilon$ RNG is discussed in the following sub-chapter regarding model validation.

Thirdly, the energy equation describes the conservation of energy due to conduction, convection, and volumetric heat generation [41]. ANSYS Fluent uses entalphy form of the energy equation, which is written as:

$$\frac{\partial (\rho h)}{\partial t} + \nabla \cdot (\rho \vec{v} h) = \nabla \cdot (k \nabla T) + S_h \tag{3.3}$$

where $h$ is specific enthalpy [$J/kg$], $T$ is temperature [$K$], $k$ is thermal conductivity [$W/m.K$], $Sh$ is the volumetric heat source term [$W/m^3$].

In floating PV application, ANSYS Fluent solves the energy equation in both the solid and fluid domains. In the air and water domain, the equation models convective heat transfer as air and water flows over and beneath the PV module. In the PV module layer (solid domain), the equation models conduction through the PVmodule material, driven by the applied solar irradiance on the top surface and heat exchange with air and water on the top and bottom surfaces.

In ANSYS Fluent, solving these equations across solid and fluid zones and interfaces is referred to as a Conjugate Heat Transfer (CHT) simulation. CHT simulation allows continuity at the solid-fluid interfaces, which results in a accurate prediction of temperature gradients within the PV module's surfaces, especially the PV module backside, where temperature is commonly measured using temperature sensors such as PT100. These governing equations are all in accordance with the ANSYS Fluent software theory guide [42], and are the basis of the numerical calculation that is being done in this chapter.

### 3.1.2. ANSYS Fluent Workflow

To numerically simulate the thermal behaviour of floating PV systems, a structured workflow is implemented using ANSYS Fluent. This workflow is illustrated in figure 3.1. The workflow consists of four key stages, which are geometry creation, meshing, models setup and calculation, and post-processing. Each of these steps is critical for obtaining physically representative and accurate results.

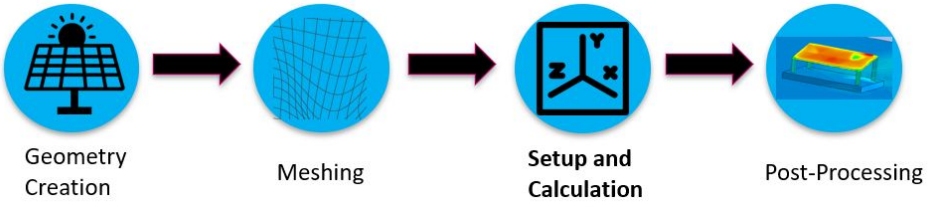


**Figure 3.1:** ANSYS Fluent Simulation Workflow

In the geometry creation stage, a 2D or 3D model of the floating PV system and its surrounding air and water domains is constructed. There are two main geometry creator in ANSYS version R1 2024, namely SpaceClaim and DesignModeler. The later is chosen within the scope of this research due to its straight-forward and more robust graphical user interface. The geometry is designed to capture the relevant physical boundaries affecting convective, conductive, and radiative heat transfer around the PV system, while maintaining a reasonable computational load.

The next stage is meshing. This step involves discretizing the fluid and solid domains into a finite number of control volumes or elements. The quality of the mesh plays an important role in the accuracy and stability of the CFD simulation, especially in capturing convective heat transfer and resolving temperature gradients around the PV module surfaces. To achieve balance between computational load and numerical acccuracy, a non-uniform mesh is applied with location-specific refinemen, which simply means having different mesh element sizes for different faces or volumes in the geometry. For example, having finer mesh near the solid-fluid interfaces of the PV module, air domain boundaries, and the water surface. This ensures that areas with expected high temperature gradients are resolved with higher mesh quality. Additionally, inflation layers are applied on solid boundaries to accurately capture near-wall flow behaviour and thermal boundaryl layer effects.

To assess and ensure mesh quality, two primary quality metrics are monitored, which are skewess and orthogonal quality. High skewness values (closer to 1) can lead to numerical instability, while low orthogonal quality (below 0.1) may cause poor convergence and inaccurate solutions. Throughout the simulations in this study, the mesh is designed to maintain a maximum skewness below 0.9 and a minimum orthogonal quality above 0.2, following ANSYS' user guidelines. These ranges ensure reliable calculation accuracy while keeping reasonable computational time.

During the models setup and calculation phase, the governing equations discussed in the previous section are chosen and numerically solved. This includes selecting appropriate models for energy and viscous flow or turbulence. In this step, critical simulation settings such as cell zone conditions, boundary conditions, material properties, and solver schemes are defined. It is also in this stage that **model validation** becomes essential, particularly for energy and turbulence, as they significantly influence heat transfer results in floating PV systems.

Finally, in the post-processing step, simulation results such as temperature distribution, velocity profile, and convective heat transfer coefficient are extracted and visualized. These outputs are analyzed to assess the PV module temperature distribution and compare it with analytical or measured values.

## 3.2. CFD Simulation Validation

Before proceeding to the case study of floating PV systems using CFD, it is essential to ensure that the selected physical models and simulation configurations can accurately represent the thermal and fluid dynamics behaviour relevant to this study. This validation process ensures the reliability of the simulation results and provides a good foundation for subsequent modelling steps.

In this study, three key components of the CFD model are validated individually. These include the energy equation model, the viscous (turbulence) flow model, and the air-water surface boundary layer development. For each of the first two components, a literature-based approach was done, in which a peer-reviewed study is selected that utilizes the same model under well-defined conditions and has been validated against real measurement data. The CFD setup described in the reference study is replicated as closely as possible in ANSYS Fluent, including geometry, mesh resolution, boundary conditions, and solver settings. The resulting output is then compared to the reported simulation and experimental results. If the results match with sufficient accuracy, the model is concluded to be valid for use in the current study.

The third aspect of the validation focuses on understanding the boundary layer development at the air-water interface. This analysis is crucial in determining the minimum distance required from the air inlet to the PV module to ensure a fully developed flow in the air domain before reaching the PV module surface. For this, a controlled simulation is conducted to evaluate the temperature boundary layer profiles across the air domain, allowing the identification of the appropriate placement region for the floating PV system to ensure realistic thermal and convective behaviour in subsequent simulations. Together, these three validation steps provide a foundation in the selection and application of the CFD models for floating PV scenarios.

### 3.2.1. Partial Validation for Energy Equation Model

To validate the energy model used in the CFD simulation, a benchmark case of laminar forced convection over a flat plate was selected, following the methodology and setup in the study by Prasad et al. [43]. In this validation case, a two-dimenstional horizontal plate of 23 cm in length and 2.5 cm in width is subjected to a uniform inlet air velocity, with the bottom surface heated at a constant temperature and the top surface set as symmetry to represent a far-field boundary, as illustrated in figure 3.2. The geometry, boundary conditions, and meshing setup in ANSYS Fluent were replicated in accordance with the reference case, including the use a no-slip condition on the heated wall and a pressure outlet on the downstream face. The inlet velocity was varied to generate different heat transfer coefficients, which were then extracted for comparison.

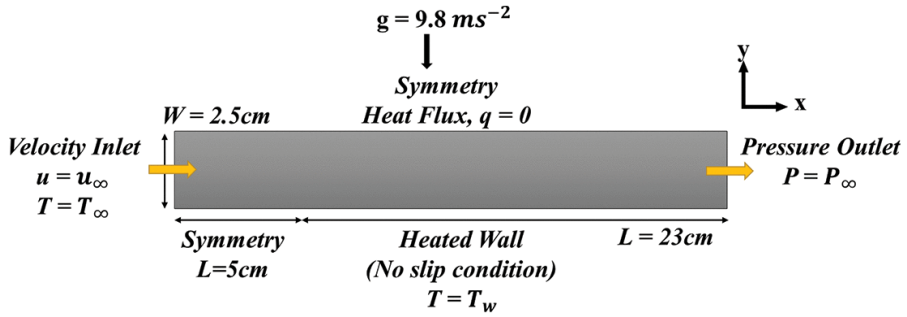


**Figure 3.2:** Energy Model Validation Illustration

To quantitatively assess the agreement between the simulation and experimental results, the extracted convective heat transfer coefficients were used to calculate the local Nusselt numbers. As mentioned in chapter 2, Nusselt number is a dimensionless quantity that represents the ratio of convective to conductive heat transfer across a boundary. The Nusselt number is plotted as a function of the Rayleigh number, which represents the ratio of bouyancy-driven free convective flow to diffusive transport. As the Rayleigh number increases, the thermal convection becomes more dominant relative to conduction.

The comparison between CFD simulation and experimentally-derived Nusselt numbers is shown in figure 3.3, plotted across a range of Rayleigh numbers. The black square markers represent experimentally derived Nusselt number values from the reference study, while the red circle markers indicate the results obtained from the ANSYS Fluent simulation. As shown in the graph, both results show the expected upward trend in Nusselt number with increasing Rayleigh number. This behaviour reflects the increase of convective heat transfer as bouyancy effects become more dominant. The alignment between the two datasets improves at higher Rayleigh numbers, which shows an improved stability and mesh independence in high-convection regions.

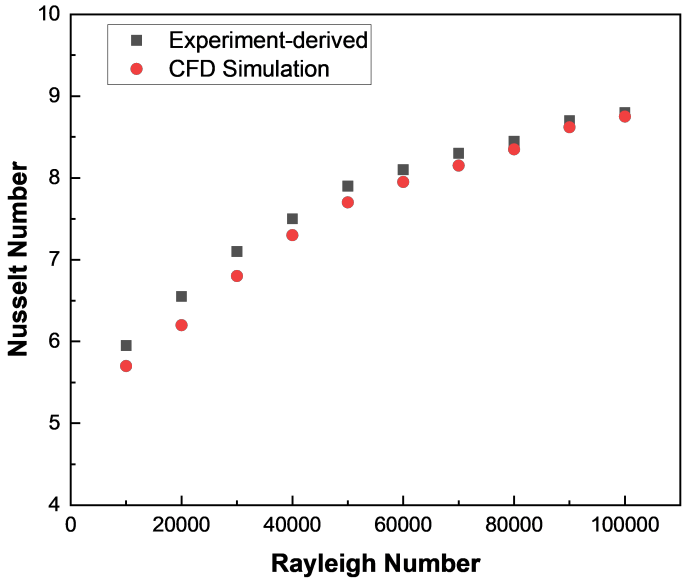


**Figure 3.3:** Comparison of Nusselt number vs Rayleigh number for experimental data and CFD simulation results.

Overall, the CFD simulation results in a close agreement with experimental data, with an average deviation of 2.53%. This demonstrates that the CFD energy model successfully captures the thermal response over a heated plate. Minor deviations at lower might be caused by mesh resolution limits or local numerical diffusion, but these differences remain within acceptable margins. In conclusion, these results indicate that the energy equation implementation in ANSYS Fluent yields reliable and accurate predictions for convective heat transfer, validating its use for thermal modelling in subsequent sections.

### 3.2.2. Partial Validation for Viscous (Turbulence) Model

Next, the partial validation for the turbulence model was done. To validate the turbulence model used, a benchmark case of forced convection over an inclined heated flat plate was selected. This case was adapted from the experimental and numerical study of Touzani et al.[44], in which the study of heat transfer behaviour of a plate with varying inclination angles under turbulent flow was done. The aim of this validation step is to assess whether the selected $k-\epsilon$ turbulence model can accurately replicate experimental observations and heat transfer characteristics, given the similarity to PV modules as an inclined and heated flat plate.

As shown in figure 3.4, the validation geometry consists of a rectangular domain with a centrally placed inclined heated plate subjected to airflow at different velocities. In the replicated CFD setup, boundary conditions, mesh density, and domain sizes were aligned with the reference case to maintain comparability. A uniform inlet velocity was applied, while the outlet was set to a pressure outlet condition. The no-slip and constant heat flux conditions were assigned for the plate surfaces. The resulting heat transfer coefficient $h$ was extracted at the heated surface, and the correspponding average Nusselt number was calculated.

Figure 3.5 presents the comparison between the CFD simulation results and the experimental data for turbulent airflow over an inclined heated plate. The horizontal axis represents Reynolds number, characterizing the flow regime based on inertia and viscous forces. The vertical axis, shows the corresponding Nusselt number, which quantifies the convective heat transfer relative to conduction heat transfer. As discussed in Chapter 2, Nusselt number has been revealed to become a key metric that affects the thermal model's PV module temperature prediction accuracy by directly affecting the amount of heat dissipated through convection. As shown in the graph, both the experimental and simulated data follow the expected trend, where Nusselt number increases as the Reynold number increases,

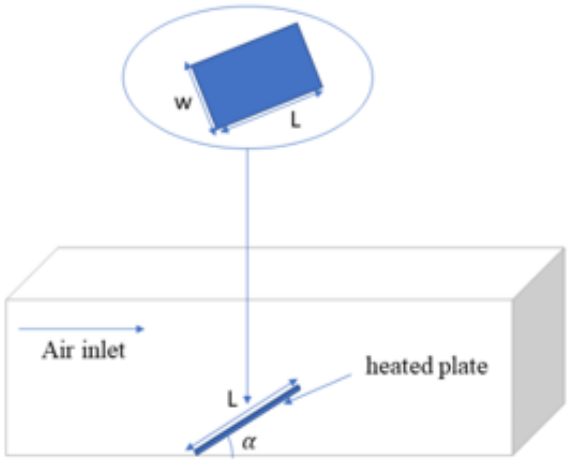


**Figure 3.4:** Validation case setup for RNG k-e turbulence model

indicating a more dominant convective heat transfer at higher flow velocities. The CFD results (red circles) closely follows experimental values (black squares), particularly in the low to medium Reynolds number range, demonstrating the $k-\epsilon$ model capability to accurately capture the convective behaviour in turbulent flow regime.

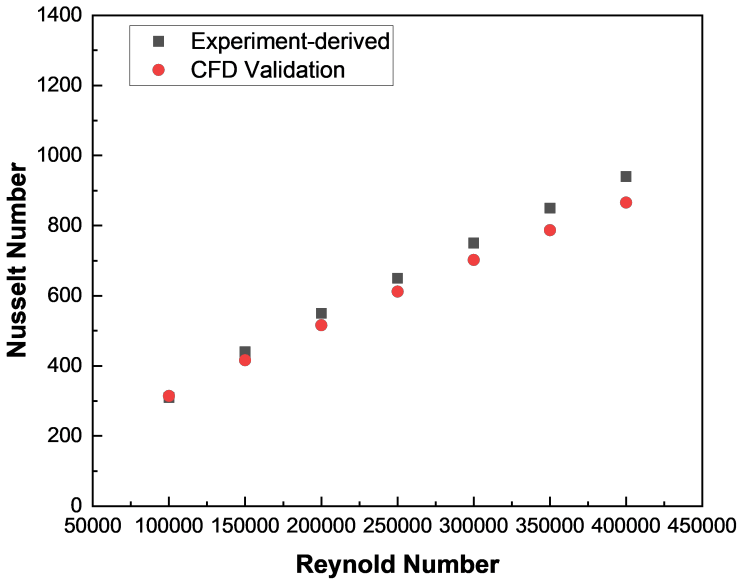


**Figure 3.5:** Comparison of Nusselt number between CFD and experiment across Reynolds number range

At higher Reynolds numbers, some slight deviation can be observed between CFD and experimental Nusselt number values. This increasing deviation at higher Reynolds numbers might be due to the limitations of the turbulence model in resolving near-wall turbulence which become more apparent under high flow momentum. Despite these deviations, the overall agreement remains strong, with an average deviation of 5.80% across the full range of the tested Reynolds numbers. This indicates that the $k-\epsilon$ RNG turbulence model provides a sufficiently accurate approximation of turbulent heat transfer behavior for the simulation conditions. Therefore, this turbulence model van be considered validated for use in floating PV thermal modelling.

### 3.2.3. Air-Water Interface Boundary Layer Analysis

To complement the validation of the energy and turbulence models, and additional assessment was done to analyze the development of the thermal boundary layer at the air-water interface. This analysis is important in understanding convective heat transfer behaviour from the water surface, which plays a key role in cooling mechanisms for floating PV systems. The objective is to determine the required distance from the air inlet for the boundary layer to be fully developed. This required flow development region is then become the basis of subsequent modelling and geometry domain design for the case studies.

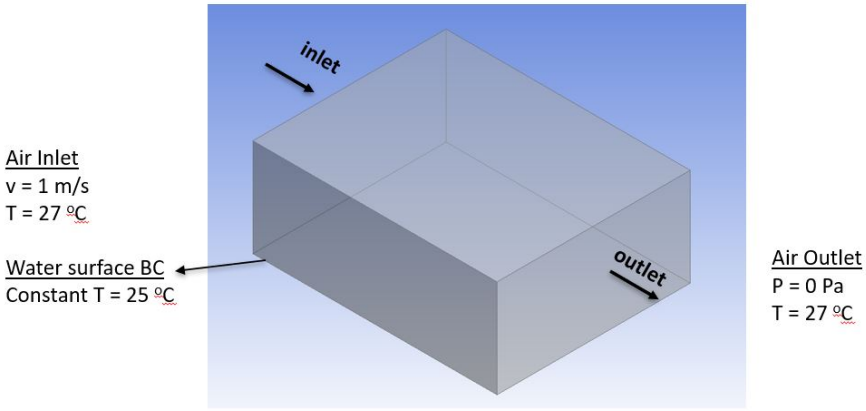


**Figure 3.6:** CFD setup for air–water boundary layer simulation

The simulation domain, as illustrated in figure 3.6 consists of a rectangular box that represents the air domain. The front surface of the air domain is acting as a velocity inlet with inlet temperature of $27^oC$ and wind speed of 1 m/s, while the bottom of the air domain represents the water surface that maintains a constant temperature of $25^oC$. These chosen boundary conditions were selected to reflect typical environmental conditions for floating PV systems deployed in tropical or subtropical climates. An air speed of 1 m/s represents a mild wind condition that is common during daytime in calm weather scenarios. The $2^oC$ temperature difference between air and water creates a realistic and measurable thermal gradient that allows the development of a convective boudnary layer without triggering an overly high bouyancy-dominated effects that might complicate the baseline simulation. Additionally, these values are aligned with the measured environmental inputs used in the subsequent case studies, ensuring realistic consistency across simulations.

The air outlet was set at zero gauge pressure and the same temperature as the inlet, assuming negligible thermal gain across the flow region. The air flows over the constant temperature water surface, inducing a thermal boundary layer to form and grow downstream. Temperature contours and thermal gradients near the air-water interface is then monitored to observe the boundary layer behavior.

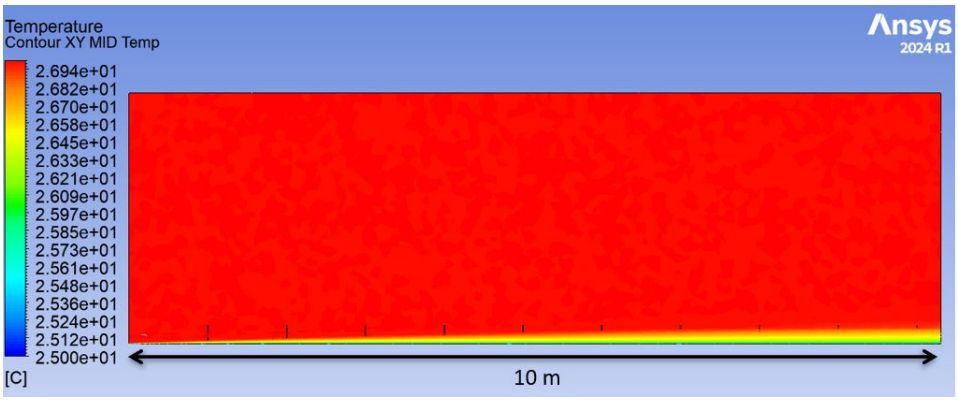


**Figure 3.7:** Temperature contour across air–water interface

Temperature data were extracted along vertical lines at 1 meter intervals along the domain length. The thermal boundary layer thickness at each location was calculated as the veritcal distance from the water surface at which the temperature reached 99% of the bulk air temperature. Figure 3.7 depicts the temperature contour profile, showing the thermal gradient across the verticalal direction near the surface, especially within the first few meters downstream of the inlet.

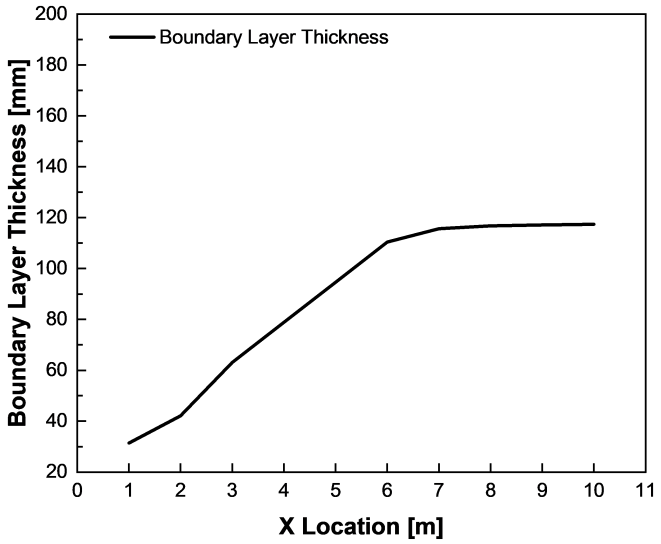


**Figure 3.8:** Thermal boundary layer thickness development along the air–water interface

**Table 3.1:** Boundary Layer Thickness and Percentage Increase Along X-Direction

| Location X [m] | BL Thickness [mm] | % Increase |
|---|---|---|
| 10.0 | 117.39 | 0.21% |
| 9.0 | 117.14 | 0.30% |
| 8.0 | 116.80 | 1.00% |
| 7.0 | 115.64 | 4.74% |
| 6.0 | 110.40 | 16.66% |
| 5.0 | 94.64 | 20.00% |
| 4.0 | 78.86 | 25.03% |
| 3.0 | 63.07 | 49.80% |
| 2.0 | 42.11 | 34.07% |
| 1.0 | 31.41 | - |

As visualized in figure 3.8, the boundary layer thickness increases significantly within the first 6 meters, after which the rate of boundary layer growth decreases. From the detailed results in 3.1, it is observed that after distance of 6 meters from the inlet, the boundary layer thickness increases by less than 5%, indicating that it has reached a fully developed state. At this point, the boundary layer thickness stabilizes around 117 mm. This implies that for the subsequent case studies, a minimum of 6 meters upstream length is needed to ensure that a fully developed thermal boundary layer effects are captured for accurate convection behavior representation above the water surface. This boundary layer analysis provides a foundation for positioning the floating PV system in the case studies. Ensuring a fully developed flow condition improves the reliability of the convective heat transfer, and consequently, PV module temperature predictions.

In summary, the validation steps carried out for both energy and turbulence models have demonstrated good agreement with experimental benchmarks, confirming that the selected CFD setups and physical models are appropriate for simulating heat transfer dynamics relevant to floating PV systems. Further-

more, the air-water boundary layer analysis provided insights into the fully developed thermal behavior over the water surface, supporting the basis of the applicable boundary condition selection for floating PV scenarios. With these models and setups now validated, the following section aims to apply them to a practical case study involving a single-module floating PV system to evaluate thermal behavior under real-world conditions

## 3.3. CFD Study Case for Single-Module Floating PV System

Following the validation of key CFD models, the next step is to implement a study case that reflects a practical floating PV system setup. This sub-chapter focuses on the simulation of a single-module floating PV configuration. This serves as a real-world representation to assess the prediction accuracy of CFD in replicating the thermal behavior of floating PV systems. By isolating a single PV module within a simplified domain, this section allows for an analysis of heat transfer interactions between te PV module, ambient air, and the water surface. Additionally, the results obtained from this step will be adapted to the previously developed resistive thermal model to improve its accuracy for floating PV applications.

### 3.3.1. CFD Simulation Setup

To investigate the thermal behavior of a single-module floating PV system, a computational domain was constructed in ANSYS Fluent based on site-specific conditions reference from the study of Rahaman et al. [28]. This domain geometry is depicted in figure 3.9.

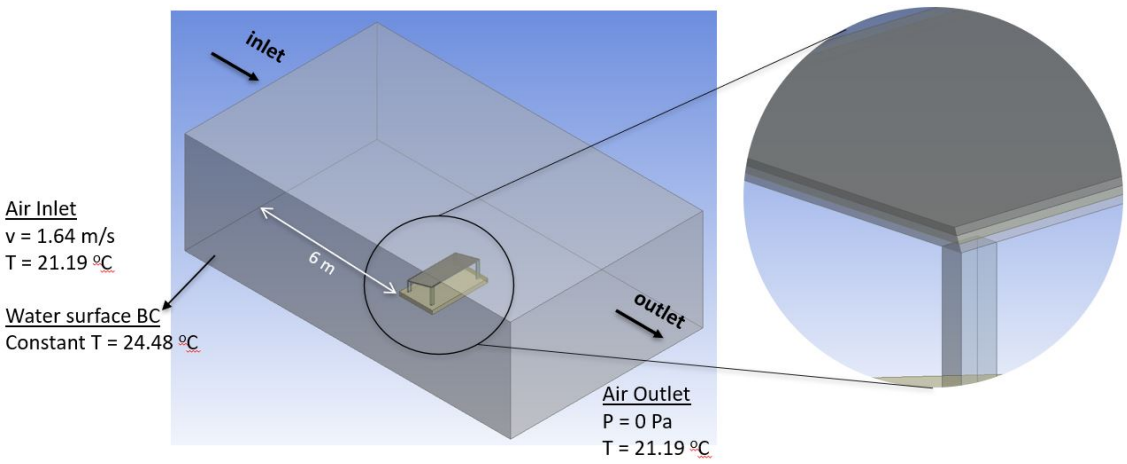


**Figure 3.9:** CFD domain and boundary conditions for single-module floating PV simulation. Environmental input values adopted from Rahaman et al. [3].

Based on reference on-site measurement data, the inlet boundary was assigned a uniform air velocity of 1.64 m/s and temperature of $21.19^oC$, while the outlet was set to a pressure outlet with zero gauge pressure and the same air temperature. At the base of the air domain, the water surface was modeled as a constant-temperature boundary condition at $24.48^oC$. These environmental values were adopted directly from Rahaman et al. [28], ensuring the simulation input reflects realistic operating conditions.

To ensure accurate thermal representation of the PV module, a three-layer structure is modeled in the simulation geometry, as shown in 3.9. These layers consist of the top layer made of glass, which serves as the transparent cover allowing solar irradiance to pass through. The middle layer represents the PV cell layer, which is the primary heat-generating region due to solar energy absorption. Heat generation within this layer is modeled using a volumetric heat source implemented via ANSYS Fluent's Cell Zone Condition setup. The value of the volumetric heat source assigned to the PV cell layer corresponds to the irradiance level that is received by the PV module. Finally, the back layer corresponds to the backsheet layer of the PV module which provides structural support and electrical insulation. The material properties for all three layers which include density, specific heat capacity, and thermal conductivity was taken from the reference study to maintain consistency with the reference dataset used

for comparison.

The CFD simulation is performed under steady-state conditions, which is appropriate for analyzing temperature distribution under a constant environmental setup. For the numerical setup, the pressure-based solver is used with the second-order upwind discretization scheme for momentum and energy equations to improve spatial accuracy. The energy equation model and $k-\epsilon$ RNG turbulence model employed in this simulation have been previously validated, ensuring reliable prediction of the heat transfer mechanisms in the simulation. The numerical calculation is ran iteratively until the solution converges.

### 3.3.2. PV Module Temperature Results and Comparison

The temperature distribution contour obtained from the CFD simulation provides a insightful view of the heat dissipation behaviour around the single-module floating PV system. The temperature profile distribution is visualized in two contour plots, with insights on the conduction pathways through the PV structure as well as the convective heat dissipation to the surrounding air.

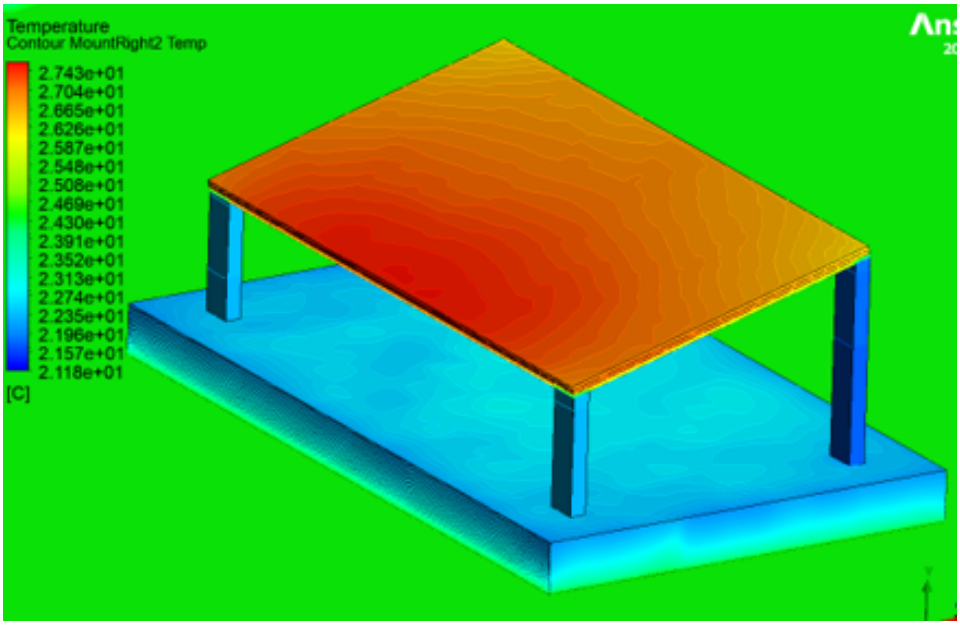


**Figure 3.10:** Top View Temperature Contour Result for Single-Module Floating PV

Figure 3.10 presents a top view contour of the temperature across the PV module and the floating structure. It can be observed that the highest temperature is clearly located in the middle layer, corresponding to the PV cell zone where heat generation occurs. From this region, heat conducts both upward into the glass layer and downward into the backsheet. As expected, the glass layer shows lower temperature than the PV cell due to its exposure to ambient air and the resulting radiative and convective cooling. Similarly, the backsheet layer conducts heat both via convection to the backside air and via conduction into the mounting structure and eventually into the floater. The temperature gradient observed reflects this conduction pathway, with temperatures gradually declining as the heat moves downward. This downward conduction toward the water boundary confirms the effectiveness of water as a thermal sink, supporting the understanding that floating PV systems benefit from enhanced thermal dissipation through conduction to the water surface.

Figure 3.11 shows a vertical cross-sectional contour, emphasizing convective heat transfer from the PV module to the ambient air. The temperature gradient observed in the air illustrates how heat is dissipated away from the system. This gradient is most pronounced especially near the backsheet, indicating that natural and forced convection plays a significant role in dissipating heat from the PV module. As the distance from the PV module increases, the air temperature approaches the ambient inlet condition, indicating a drop in thermal influence of the PV module. This gradient confirms the thermal boundary layer above and around the PV module.

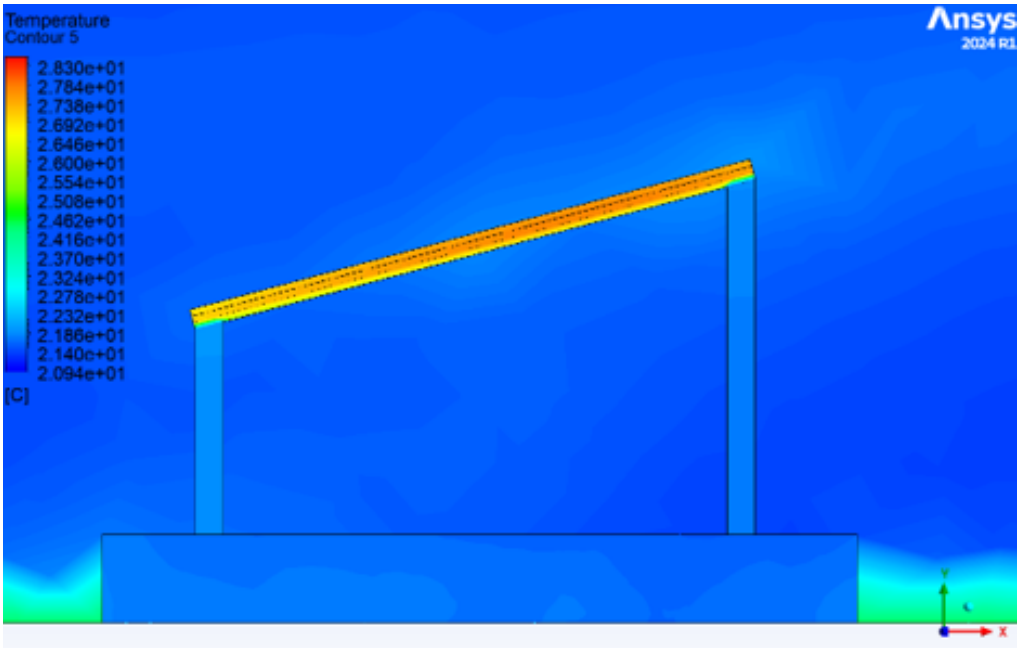


**Figure 3.11:** Cross Section View Temperature Contour Result for Single-Module Floating PV

Quantitatively, the CFD simulation yielded an area-weighted average backsheet temperature of $25.957^oC$, which shows a very close match with the measured backsheet temperature of $25.95^oC$ as measured on-site by the reference study. To further compare the CFD simulation result and the measured data, the simulation was extended to cover all twelve month data point cases based on the reference study. The boundary conditions for each simulation were adjusted based on the measured monthly values of wind speed, ambient temperature, and water surface temperature, and the resulting PV module temperature was extracted for comparison.

Figure 3.12 presents the comparison between CFD-extracted PV module temperatures and corresponding monthly measurement data. From the graph, it can be observed that the CFD model demonstrates very strong agreement with the measurements across the entire data points. The maximum temperature occurs in February at approximately $28^oC$ while the lowest is in July around $14.5^oC$. In both cases, the simulation accurately tracks the seasonal variation and thermal patterns.

To assess the accuracy, the error metrics root mean square error (RMSE) and mean absolute error (MAE) is calculated. The RMSE and MAE was calculated to be $0.23^oC$ and $0.18^oC$, respectively. These low error values reinforces the confidence in the CFD model's predictive capability. The CFD method, eventhough has a very high accuracy as shown by the results, also comes with a reasonably high computational costs and time. To adapt these results to the previously developed resistive thermal model, key thermal parameters, most notably the convective heat transfer coefficient $h$ and its corresponding Nusselt number $Nu$ can be extracted. This approach bridges the high-accuracy numerical modelling with the faster and less computationally demanding analytical modelling, and will be discussed in the next section.

### 3.3.3. Key Parameters Extraction to Update the Resistive Thermal Model

To integrate the results from the validated CFD simulations into the analytical resistive thermal model, it is crucial to extract key thermal parameters, which are the convective heat transfer coefficient $h$ and Nusselt number $Nu$. PV module temperatures and $h$ can be directly recorded from ANSYS Fluent, while $Nu$ can be calculated from the corresponding convective heat transfer coefficient using the simple correlation:

$$Nu = \frac{h \cdot L}{k} \tag{3.4}$$

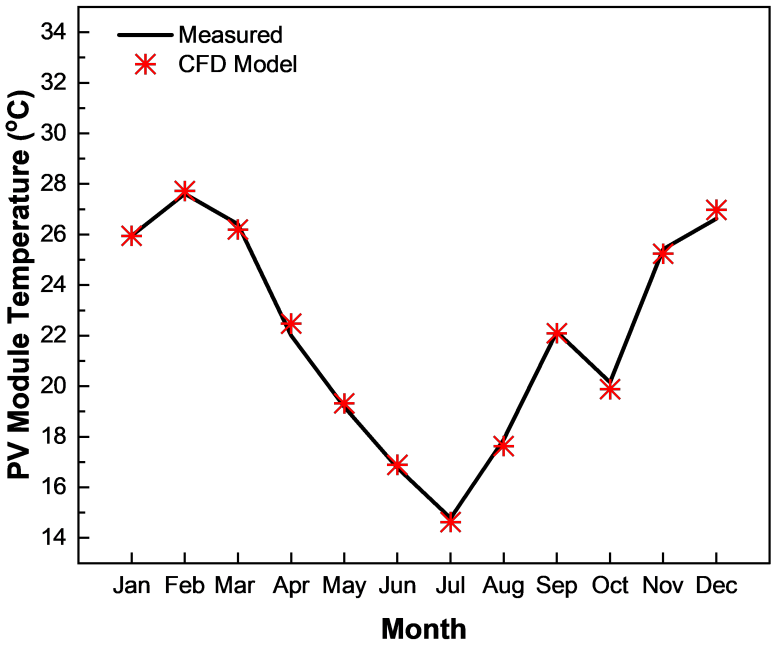


**Figure 3.12:** CFD vs Measured Backsheet Temperature Comparison

where $L$ is the PV module length and $k$ is the thermal conductivity of air, both values are constant. These $Nu$ values represent a non-dimensional expression of convective heat transfer behavior and are directly used as updated inputs for the RT model to improve its accuracy under varying environmental conditions.

**Table 3.2:** Monthly Convective Heat Transfer Coefficient and Corresponding Nusselt Number

| Month | CFD Backsheet Temp [°C] | CFD Backsheet $h$ [W/m$^2$K] | Calculated $Nu$ |
|---|---|---|---|
| Jan | 25.96 | 12.737 | 822.0 |
| Feb | 26.14 | 15.048 | 971.2 |
| Mar | 25.00 | 16.257 | 1049.2 |
| Apr | 21.82 | 14.234 | 918.6 |
| May | 19.25 | 14.064 | 907.7 |
| Jun | 16.17 | 16.017 | 1033.7 |
| Jul | 13.55 | 17.147 | 1106.6 |
| Aug | 17.87 | 15.365 | 991.6 |
| Sep | 22.09 | 17.035 | 1099.4 |
| Oct | 19.88 | 16.842 | 1087.0 |
| Nov | 25.24 | 17.437 | 1125.4 |
| Dec | 26.98 | 16.219 | 1046.7 |

As shown in table 3.2, the extracted Nusselt numbers vary monthly in response to changes in wind speed, ambient conditions, and temperature gradients. Following the extraction of monthly convective heat transfer coefficients from the CFD model and corresponding calculation of the Nusselt numbers, the resistive thermal model was updated by incorporating these refined Nu values. The resulting PV module temperature from this updated resistive thermal model are shown in figure 3.13, alongside the original resistive thermal model results and the measured PV module temperatures reported by the same reference study of Rahaman et al. [28].

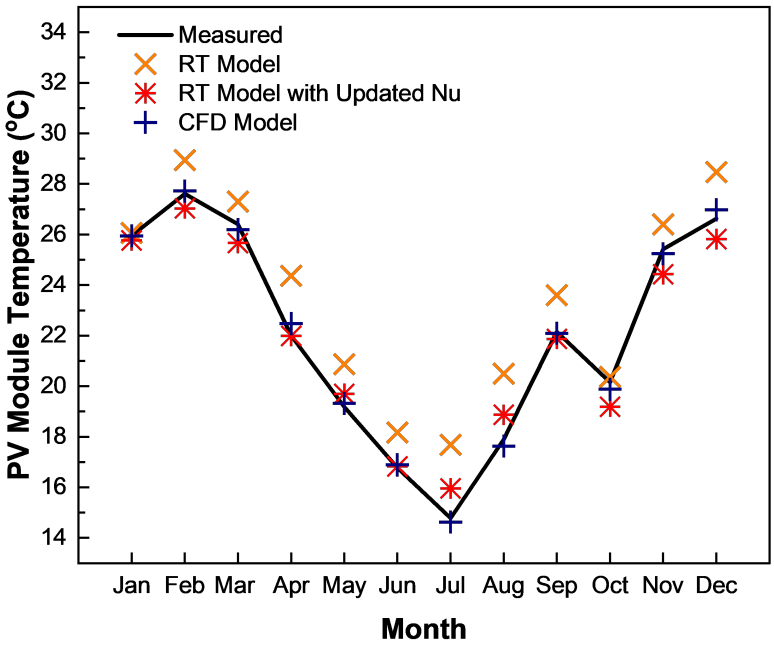


**Figure 3.13:** Comparison of measured PV module temperature, RT model prediction, andRT model with Updated Nu

From the graph, it can be observed that the original resitive thermal model (orange cross signs) consistently slightly overpredicts the PV module temperatures. This is reflected in the RMSE value of $1.70^oC$ and MAE of $1.37^oC$. After updating the resistive thermal model using CFD-derived Nusselt numbers, the updated prediction (red asterisk signs) aligns much more closely with the measured data throughout the year. The updated model achieves a lower RMSE of $0.72^oC$ and MAE of $0.56^oC$, indicating a substantial increase in accuracy. This improvement strongly supports the benefit of incorporating detailed CFD-derived thermal parameters into simplified resistive thermal models. It demonstrates that by calibrating key heat transfer parameters such as the convective coefficient, the analytical thermal model's accuracy can be greatly improved.

This section succesfully validated and integrated CFD results into the resistive thermal model for a single-module floating PV system. This highlight the capability of CFD to capture detailed heat transfer behavior and improve the accuracy of analytical models. However, real-world floating PV installations consist of multiple interconnected PV modules, where aiflow obstructions influence the thermal behaviour. To extend the insights gained, the next sub-chapter extends the CFD analysis to a multiple-module floating PV system layout. This expanded study aims to analyze how spatial arrangement, particulary row spacing, affects the temperature distribution and cooling performance across the PV array.

## 3.4. Summary of Key Findings in Chapter 3

In summary, this Chapter's objective is to address the second research question, that is to analyse how can analytical thermal models be improved to better represent heat transfer mechanisms specific to floating PV systems. This question focuses on investigating the role of Computational Fluid Dynamics in capturing detailed convective, conductive, and radiative effects influenced by water proximity and ambient cooling. This chapter is structured to first introduce the role of computational fluid dynamics, and how it can be applied for floating PV system study cases. Next, validation processes are done to ensure that the CFD simulations comprehensively represent practical and real world physics and thermal interactions. Finally, case studies are done based on practical scenario and real-world floating

PV installation. After conducting the simulations, key heat transfer coefficients are extracted to finally be used as an updated input for the Resistive Thermal Model to increase its PV module temperature prediction accuracy.

The ANSYS Fluent simulation setup has been successfully validated.These validated model that are used include the energy model, turbulence model, as well as the thermal boundary layer for air-water interface. The validated model are used to conduct CFD simulations for the base case study, to finally extract the convective heat transfer coefficient and its corresponding Nusselt number values. The findings revealed that by incorporating the updated Nu values specific to floating PV application into the Resistive Thermal Model, the thermal model's accuracy can significantly be improved. The PV module temperature prediction accuracy is quantified by the RMSE value for the CFD-Updated Resistive Thermal Model of $0.72^oC$, which shows significant improvement from the initial Resistive Thermal Model RMSE for the base case study of $1.70^oC$. This approach answers the second research question, showing that integrating the insights of CFD into analytical approach, in this case the Resistive Thermal Model results in a further improvement in PV module temperature prediction accuracy. This method effectively combines the computational-cost effectiveness of the Resistive Thermal Model and the robustness of computational fluid dynamics approaches.

# 4

# Energy Yield Analysis of Floating PV Systems based on CFD-Updated Resistive Thermal Model

Building upon the CFD-Updated Resistive Thermal Model and validation works in previous chapters, this chapter focuses on translating the updated PV module temperature predictions into electrical energy performance metrics. This Chapter aims to address the third research question, that is to analyse how does the CFD-Updated Resistive Thermal Model affect the accuracy of energy yield simulations. The main objective is to assess how the improved thermal models, particularly the resistive thermal model updated with CFD-derived convective heat transfer coefficients impact the accuracy of energy yield estimations for floating PV systems. To achieve this, two different simulation platforms are used, which are the PVMD Toolbox developed by TU Delft and the commercial energy yield simulation software PVsyst. Both tools are utilized to simulate the energy yield based on the PV module temperature results of the CFD-Updated Resistive Thermal Model, enabling a comparative evaluation of the model's prediction accuracy. Through this analysis, this chapter aims to underline the significance of previse thermal modelling in enchancing the reliability of energy yield and electrical performance predictions for floating PV applications.

For consistency with the previously done thermal model assessment in Chapter 2 and Chapter 3, the energy yield analysis in this chapter will be based on the thermal model results of study case of Rahaman et al. [28] for a floating PV system located in Passauna, Brazil. This approach is done to have a fair and consistent comparison with the previously obtained findings, to consequently be able to draw correlation from the results of thermal modelling to the accuracy of energy yield simulations.

## 4.1. Energy Yield Analysis Using PVsyst

PVsyst is one of the most widely used commercial software tools for PV system design and energy yield prediction, especially within the solar industry. It provides a detailed environment to design and analyze PV systems where it is possible to incorporate various system losses such as shading effects, temperature effects, cable losses, and other system losses. This software has been extensively validated for land-based systems such as rooftop and ground-mounted installations, making it a preferred and reliable choice for energy yield estimation across different project sizes.

However, despite its robustness, the default thermal model in PVsyst, which is based on the Faiman empirical thermal model, is primarily validated for land-based PV systems. The default assumptions may not accurately capture the unique thermal behaviour of floating PV systems, which are, as concluded in Chapter 2 and Chapter 3, significantly influenced by proximity to water bodies that results in an enhanced convective cooling effect. Therefore, this section aims to adjust PVsyst's specific thermal parameters based on the results of the thermal modelling. By doing so, the goal is not only to evaluate

how different thermal models impact energy yield predictions but also to explore how PVsyst can be adapted to more accurately reflect floating PV-specific thermal dynamics.

As mentioned, PVsyst thermal model is based on Faiman empirical thermal model. Therefore, unlike PVMD Toolbox which directly uses hourly PV module temperatures from the output of the thermal models, PVsyst requires the thermal results to be represented through empirical heat loss coefficients $U_c$ (constant convective loss factor) and $U_v$ (wind-dependent convective loss factor). These U-values are used in PVsyst's thermal simulation to estimate PV module temperature based on ambient conditions and wind speed. Due to this, an additional step is required in this study to convert the module temperature predictions from the Fuentes fluid dynamics model, the resistive thermal model, and the updated resistive thermal model into U-values before they can be used as inputs to PVsyst. The workflow of this subsection follows figure 4.1.

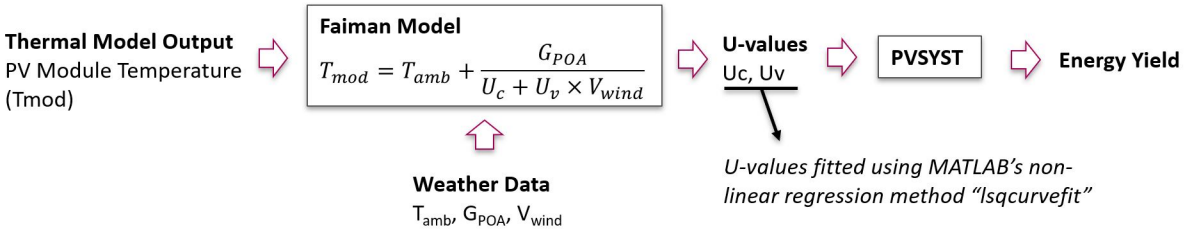


**Figure 4.1:** PVsyst Toolbox Energy Yield Analysis Workflow

The workflow begins with the PV module temperature output ($T_{mod}$) from the three assessed thermal models. These simulated $T_{mod}$ values are used together with the corresponding hourly weather data, in accordance to the Faiman model, which are the ambient temperature $T_{amb}$, plane-of-array irradiance $G_{POA}$, and wind speed $V_{wind}$, in order to calculate the heat loss coefficients required by PVsyst. Since PVsyst requires two distinct U-values ($U_c$ and $U_v$), these can not be solved linearly.

To detemine these coefficients, the equation is re-arranged and figged to the known $T_{mod}$ using MATLAB's non-linear least squares regression algorithm, $lsqcurvefit$. This method minimizes the error between the predicted $T_{mod}$ values from the Faiman model and the actual simulated values from each thermal model. This process results in a best fit estimation of $U_c$ and $U_v$ for each case. For the resistive thermal model, the fitted $U_c$ and $U_v$ values are given in table 4.1.

**Table 4.1:** U-values fitting for resistive thermal model

| Month | Ambient Temp [°C] | Gpoa [W/m$^2$] | Wind Speed [m/s] | PV Module Temp [°C] | Fitted Uc [W/m$^2$K] | Fitted Uv [W/m$^3$sK] |
|---|---|---|---|---|---|---|
| Jan | 21.19 | 173.84 | 1.64 | 26.06 | 27.01 | 5.30 |
| Feb | 20.89 | 252.99 | 1.43 | 28.95 | 26.17 | 3.67 |
| Mar | 21.10 | 202.33 | 1.50 | 27.30 | 26.42 | 4.13 |
| Apr | 17.63 | 175.19 | 0.96 | 24.37 | 24.52 | 1.54 |
| May | 15.60 | 168.87 | 1.35 | 20.87 | 26.54 | 4.08 |
| Jun | 14.04 | 137.07 | 1.27 | 18.17 | 27.18 | 4.77 |
| Jul | 11.70 | 201.47 | 1.56 | 17.68 | 26.62 | 4.53 |
| Aug | 15.23 | 172.04 | 1.24 | 20.49 | 27.05 | 4.54 |
| Sep | 17.75 | 199.16 | 1.50 | 23.60 | 26.86 | 4.79 |
| Oct | 16.47 | 139.73 | 1.45 | 20.37 | 27.56 | 5.71 |
| Nov | 19.39 | 236.11 | 1.61 | 26.41 | 26.51 | 4.44 |
| Dec | 20.17 | 242.33 | 1.33 | 28.47 | 25.55 | 2.74 |

Table 4.1 presents the monthly fitting results for thermal loss coefficients $U_c$ and $U_v$ for the resistive thermal model, derived by applying the Faiman model to the simulated PV module temperatures. The fitted $U_c$ values, representing the constant heat loss coefficients, range from $24.52 W/m^2K$ in April to $27.18 W/m^2K$ in June. On the other hand, $U_v$, which represents the wind-dependent convective losses, shows more variation from a minimum of $1.54 W/m^3sK$ in April to a maximum of $5.71 W/m^3sK$ in October.

To simplify the model input into PVsyst, where a single set of thermal loss parameters is used for the entire yeat, the average of the monthly fitted values are calculated. This results in average $U_c$

**of** $26.5W/m^2K$ **and** $U_v$ **of** $4.19W/m^3sK$. These U-values are then input into PVsyst to represent the thermal behaviour of the resistive thermal model. This approach allows a representative U-values for the corresponding thermal model that balances accuracy and usability within PVsyst's software framework.

Similarly, the same approach is taken for the Fuentes fluid dynamics thermal model. Table 4.2 represents the U-values fitting for the Fuentes fluid dynamics thermal model.

**Table 4.2:** U-values fitting for Fuentes FD thermal model

| Month | Ambient Temp [°C] | Gpoa [W/m$^2$] | Wind Speed [m/s] | PV Module Temp [°C] | Fitted Uc [W/m$^2$K] | Fitted Uv [W/m$^3$sK] |
|---|---|---|---|---|---|---|
| Jan | 21.19 | 173.84 | 1.64 | 26.96 | 25.51 | 2.83 |
| Feb | 20.89 | 252.99 | 1.43 | 29.23 | 25.81 | 3.16 |
| Mar | 21.10 | 202.33 | 1.50 | 28.41 | 24.90 | 1.84 |
| Apr | 17.63 | 175.19 | 0.96 | 23.82 | 25.71 | 2.68 |
| May | 15.60 | 168.87 | 1.35 | 21.55 | 25.25 | 2.34 |
| Jun | 14.04 | 137.07 | 1.27 | 18.46 | 26.33 | 3.69 |
| Jul | 11.70 | 201.47 | 1.56 | 17.73 | 26.54 | 4.40 |
| Aug | 15.23 | 172.04 | 1.24 | 19.77 | 29.09 | 7.07 |
| Sep | 17.75 | 199.16 | 1.50 | 24.44 | 25.54 | 2.81 |
| Oct | 16.47 | 139.73 | 1.45 | 21.79 | 24.47 | 1.20 |
| Nov | 19.39 | 236.11 | 1.61 | 27.73 | 25.02 | 2.03 |
| Dec | 20.17 | 242.33 | 1.33 | 28.75 | 25.22 | 2.29 |

The resulting fitted $U_c$ values for the Fuentes fluid dynamics model show relatively less variation across the year, ranging from $24.46\,W/m^2K$ to $29.09\,W/m^2K$, indicating a relatively consistent constant loss coefficient. In contrast, $U_v$ values has higher fluctuation, from as low as $1.20\,W/m^3sK$ in October to $7.07\,W/m^3sK$ in August. By calculating the average of these monthly values, a single representative set of U-values was obtained. The $U_c$ is calculated to be $25.78\,W/m^2K$ while the $U_v$ is $3.03\,W/m^3sK$. These values are subsequently used as the thermal input for energy yield simulations in PVsyst.

Lastly, the same approach is also done for the updated resistive thermal model. Table **??** represents the U-values fitting for the Fuentes fluid dynamics thermal model.

**Table 4.3:** U-values fitting for updated resistive thermal model

| Month | Ambient Temp [°C] | Gpoa [W/m$^2$] | Wind Speed [m/s] | PV Module Temp [°C] | Fitted Uc [W/m$^2$K] | Fitted Uv [W/m$^3$sK] |
|---|---|---|---|---|---|---|
| Jan | 21.19 | 173.84 | 1.64 | 25.77 | 27.62 | 6.30 |
| Feb | 20.89 | 252.99 | 1.43 | 27.03 | 29.38 | 8.27 |
| Mar | 21.10 | 202.33 | 1.50 | 25.66 | 30.04 | 9.56 |
| Apr | 17.63 | 175.19 | 0.96 | 21.99 | 31.90 | 8.63 |
| May | 15.60 | 168.87 | 1.35 | 19.70 | 29.78 | 8.45 |
| Jun | 14.04 | 137.07 | 1.27 | 16.83 | 36.43 | 10.00 |
| Jul | 11.70 | 201.47 | 1.56 | 15.96 | 31.69 | 10.00 |
| Aug | 15.23 | 172.04 | 1.24 | 18.87 | 34.86 | 10.00 |
| Sep | 17.75 | 199.16 | 1.50 | 21.87 | 33.34 | 10.00 |
| Oct | 16.47 | 139.73 | 1.45 | 19.19 | 36.37 | 10.00 |
| Nov | 19.39 | 236.11 | 1.61 | 24.43 | 30.75 | 10.00 |
| Dec | 20.17 | 242.33 | 1.33 | 25.82 | 25.55 | 2.74 |

The monthly $U_c$ values for the updated resistive thermal model range from $25.55\,W/m^2K$ to $36.47\,W/m^2K$, while the $U_v$ values range from $2.74\,W/m^3sK$ to $10.00\,W/m^3sK$. For this model, a notable difference is observed in the $U_v$ values, where in several cooler months such as June to October, the regression converges at the upper boundary constraint for $U_v$, suggesting a higher sensitivity of the model to wind-induced cooling effects. These $U_v$ value cap is implemented to follow PVsyst's requirement for maximum value of wind-dependent convective heat loss coefficient. These higher coefficient values reflect the stronger convective behaviour capture through CFD, which is particularly important in floating PV installations where water surface cooling enhance heat loss from the PV module.

Taking the average monthly value results results in a $U_c$ value of $31.48\,W/m^2K$ and $U_v$ of $8.66\,W/m^3sK$. Compared to the previous results, these values are the highest among the three thermal models assessed. This outcome is consistent with the thermal model's findings, where the lowest PV module temperature is yielded by the updated resistive thermal model, which also exhibits the highest accuracy compared to the measured PV module temperature.

The Fuentes fluid dynamics model, representing existing analytical approach, yields the lowest U-values. Consistent with the findings in Chapter 2, this shows that this model underestimates the convec-

tive heat transfer for floating PV applications. The initial resistive thermal model improves slightly but still remains limited to the generalized heat transfer coefficient assumptions. On the other hand, the updated resistive thermal model significantly increases both coefficients. This highlights the significance of incorporating CFD in the resistive thermal model to increase the model's capability of representing the real-world physics and thermal dynamics between the PV module and the ambient conditions.

These fitted U-values serve as the final thermal inputs for PVsyst. This enables energy yield simulations that reflect each thermal model's interpretation of PV module temperature behaviour. By doing so, the influence of thermal modelling accuracy on electrical performance can be consistently compared and systematically evaluated.

The resulting U-values derived from each thermal model are implemented directly in PVsyst through PVsyst's "detailed losses" interface, specifically under the "thermal parameter" tab. This section of the software allows users to define the thermal behaviour of the PV system more precisely by entering, either default values or customized values for the contant thermal loss factor $U_c$ and the wind-dependent thermal loss factor $U_v$. By default, PVsyst provide several typical values for these parameters. However, these values are limited to land-based system only, the default options that can be chosen are free mounted modules, semi-integrated with air duct behind, and integration with fully insulated backside that has its corresponding U-values the highest, lower, and lowest, consecutively.

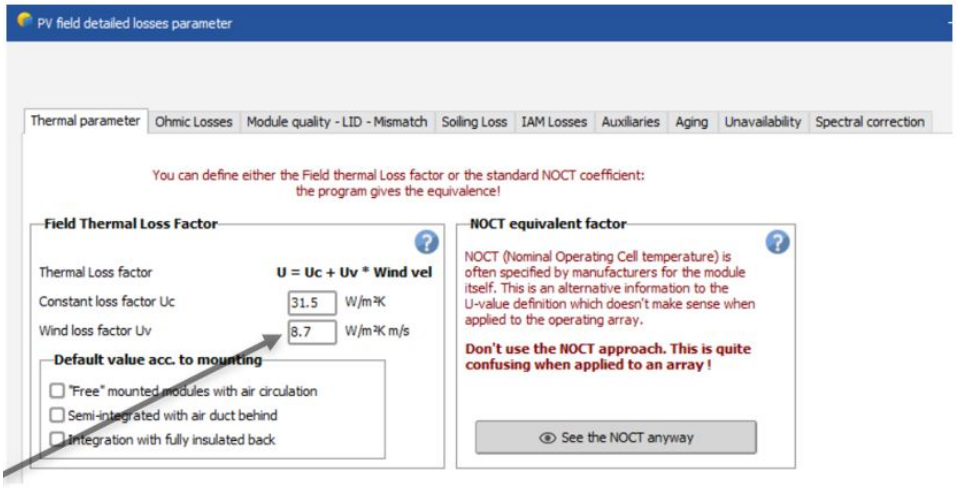


**Figure 4.2:** PVsyst Thermal Parameters Interface

Alternative to using the default values, as shown in figure 4.2, PVsyst provides an option to manually input these two coefficients. This bypasses the default assumptions commonly used for land-based systems, as discussed previously. This enables the integration of external thermal models to reflect a more realistic or applicaiton-specific behaviour, such as, in the context of this study, the enhanced convective cooling present in floating PV systems.

The simulation results obtained from PVsyst shows clear difference in the predicted specific energy yield depending on the applied thermal model, as depicted in figure 4.3. Specific energy yield, measured in $[kWh/kWp/year]$ is used as the comparative metric as it normalizes the energy output relative to the installed capacity. This allows for a fair comparison across different thermal models, independent of total system size or varying solar irradiance. This approach is efficient in isolating the impact of temperature prediction accuracy on energy performance.

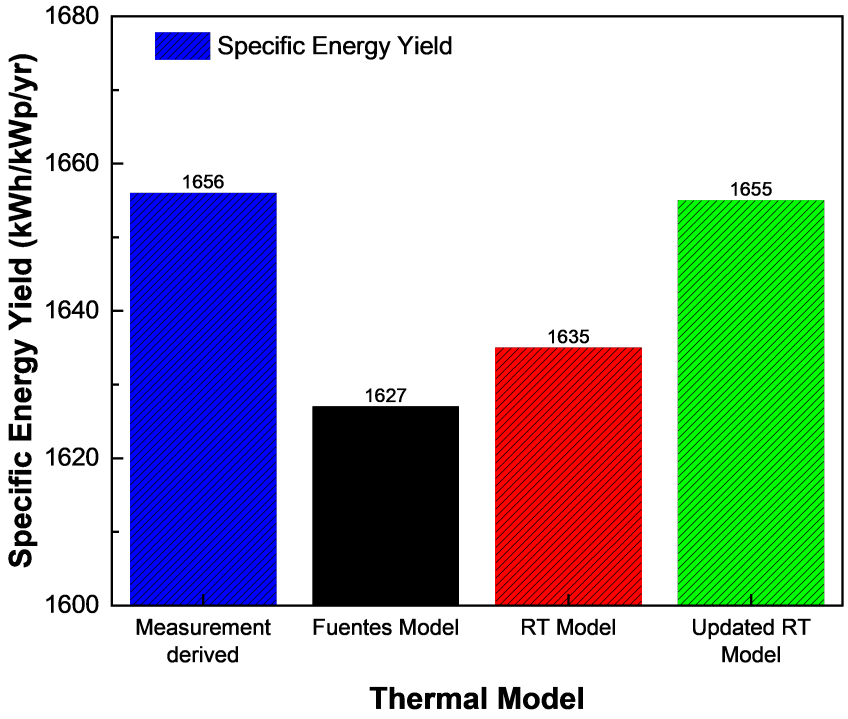


**Figure 4.3:** PVsyst Energy Yield Comparison for Different Thermal Models

The measurement-derived specific energy yield is used as a benchmark value for this comparison, which is 1656 kWh/kWp/year. This serves as the reference value for evaluating the accuracy of the three thermal models. The Fuentes fluid dynamics model, which is implemented in the PVMD Toolbox, resulted in a yield of 1627 kWh/kWp/year, underestimating the energy output by 1.75% relative to the measured value. Consistent with the assessment on the thermal model, this discrepancy is likely caused by the model's inability to capture the increased cooling effect experienced by floating PV systems

The Resistive Thermal Model results in a more accurate estimation of 1635 kWh/kwp/year, corresponding to an error value of 1.27% compared to the measured yield. This decrease in deviation once again consistent with the findings in Chapter 2 that resistive thermal model offers an increased accuracy due to a more specific physics-based thermal representation. However, the most accurate result was achieved using the Updated Resistive Thermal Model, which integrates convective heat transfer coefficients derived from CFD simulations. This model predicted a yield of 1655 kWh/kWp/year, nearly identical to the measured value with an error of 0.10%.

These findings re-emphasize the importance of refining thermal models when evaluating the energy performance of floating PV systems. By incorporating insights from CFD simulations, the Updated Resistive Thermal Model demonstrates its capability to closely replicate real world thermal behaviour, which consequently leads to significantly improved accuracy in energy yield predictions.

## 4.2. Energy Yield Analysis Using PVMD Toolbox

The second energy yield analysis is done using the PVMD Toolbox. PVMD Toolbox is an open-souce MATLAB-based simulation platform developed by TU Delft, and is a comprehensive PV system simulation tool which includes multiple simulation levels. PVMD Toolbox has the capability to simulate physical behaviour from as small as PV cell level to a full-size multiple-module PV systems. Each step's simulation is done at an hourly basis, and the simulation duration can be specified in the PVMD Toolbox's input creator.

At the smallest level, the cell simulation models the behaviour of an individual solar cell, taking into account the PV cell technology and material properties. These cells are then combined in the module simulation layer. In this step, in addition to combining the cells based its defined numbers and configuration, the PV module view factor is also calculated based on the given system coordinate. This results in an hourly view factor values, which will affect the amount of irradiance received by the PV module.

Next, the weather simulation layer processes environmental inputs. These environmental inputs, which include irradiance components, ambient temperature, wind speed, and other meteorological variables, are fed into the toolbox in a .csv format, and typically are obtained from meteorological databases such as Meteonorm. Following the weather data compilation, the thermal simulation is done. The thermal simulation's goal is to calculate the PV module temperature from on the given weather data, based on a specifically chosen thermal models. The default thermal model that is used in the Toolbox is the Fuentes fluid dynamics model. In this step, it is also possible to override and directly replace the PV module temperature values with results from other thermal modelling methods. This step is crucial in this chapter's analysis, as the results of the assessed thermal models will be the input in this step. Lastly, the PVMD Toolbox calculates the DC-side energy yield in the electrical simulation layer to produce the hourly DC energy output. From these hourly values, the total annual energy yield is calculated and compared between each thermal models. From the general workflow of the PVMD toolbox, the workflow of the energy yield analysis in this sub-chapter is given in figure 4.4.

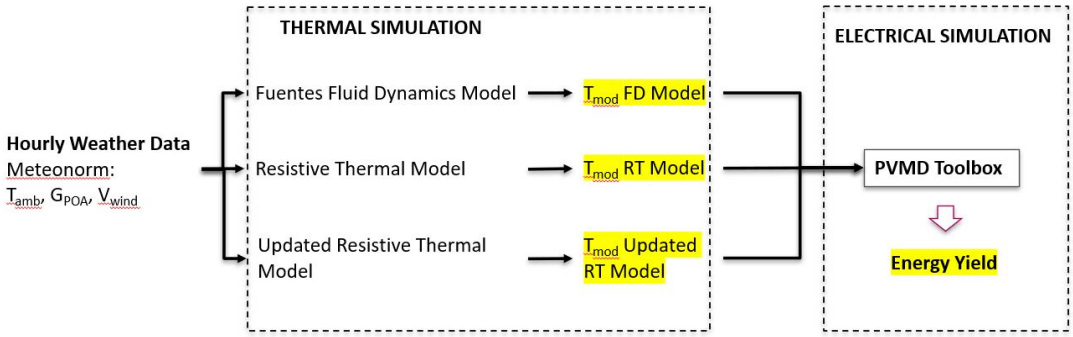


**Figure 4.4:** PVMD Toolbox Energy Yield Analysis Workflow

The workflow for energy yield analysis using the PVMD Toolbox begins with hourly weather data, which serves as the input for all thermal simulations. This dataset, obtained from Meteonorm database, includes key meteorological parameters such as ambient temperature, plane-of-array irradiance, and wind speed. These variables are then used as input of three thermal models, as analyzed in Chapter 2 and Chapter 3 to calculate the corresponding PV module temperatures. The first thermal model is the Fuentes fluid dynamics (FD) model, which is the default thermal model implemented in the PVMD Toolbox. The second model is the resistive thermal (RT) model, which has been developed in Chapter 2. The third is referred to as the Updated RT model, that increases accuracy of RT model using Nusselt number values from CFD simulations, providing a more physically representative estimation of the PV module temperature values ($T_{mod}$).

Each of these thermal models outputs an hourly $T_{mod}$, which is then fed into the electrical simulation layer of the PVMD Toolbox. As mentioned, this stage calculates the electrical output of the PV module under varying environmental conditions, enabling a direct comparison of energy yields resulting from the three thermal modelling approaches. This workflow allows for assessing the influence of thermal model accuracy on the predicted energy yield of floating PV systems under realistic weather conditions.

For the analysis in this chapter, once again, the base case study of [28] as done in Chapter 2 and Chapter 3 is used for consistency. To run the PVMD Toolbox, an hourly resolution of PV module temperature is required to calculate the hourly energy yield values. However, the reference case study by Rahaman et al. only provides measured weather data in monthly averages, which results also in a monthly averaged PV module temperatures. Due to this data resolution mismatch, an external hourly weather data

input is necessary to be used to produce the corresponding hourly PV module temperature values.

To bridge this limitation, Meteonorm, an established and widely-used meteorological database was utilized to obtain hourly environmental parameters. In order to ensure the compatibility of Meteonorm data with the context of this study, the monthly-averaged values derived from Meteonorm were compared with the monthly measured values from Rahaman et al. The Meteonorm data is taken in the exact same location from the study case of Rahaman et al. in Passuna region in Brazil, and the aim to get the weather data that is representative, and matches, to some extent to the actual measured weather data as observed in the reference paper. This comparison provides a validation step to assess the extent to which Meteonorm data can approximate actual local environmental conditions. The comparison of the monthly average environmental data such as the ambient temperature, plane-of-array irradiance, and wind speed is given in figure 4.5, 4.6, and 4.7.

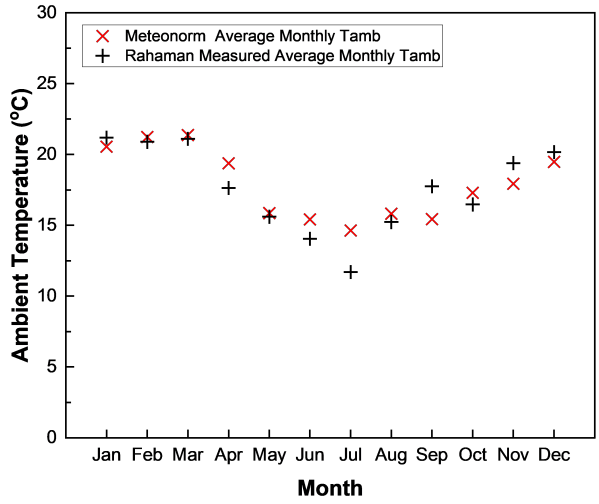


**Figure 4.5:** Comparison of Ambient Temperature between Meteonorm and Measured Values

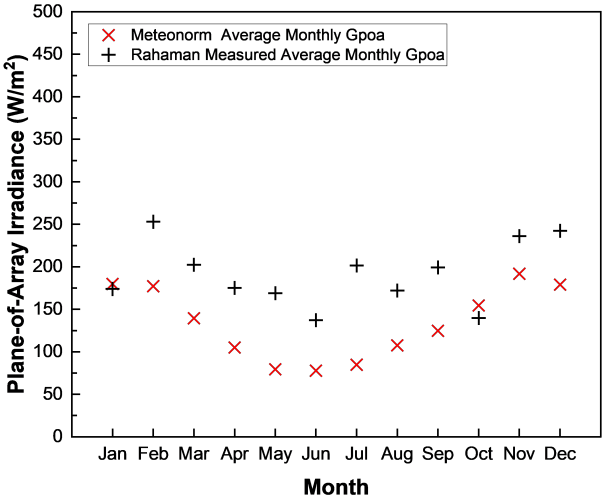


**Figure 4.6:** Comparison of Plane-of-Array Irradiance between Meteonorm and Measured Values

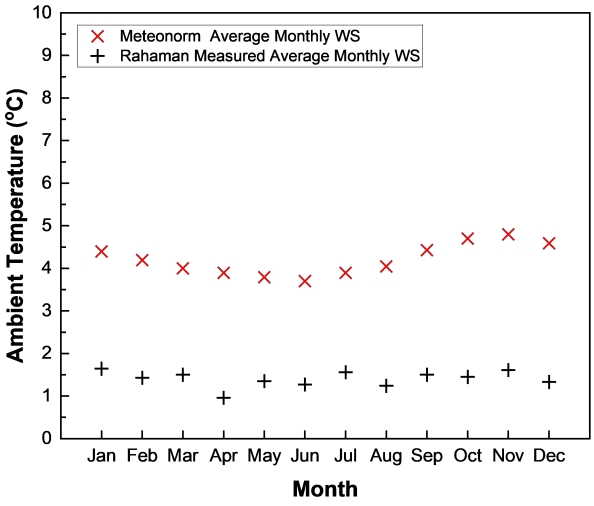


**Figure 4.7:** Comparison of Wind Speed between Meteonorm and Measured Values

As shown in the figures, the ambient temperatures $T_{amb}$ values from Meteonorm follow a seasonal pattern that aligns closely with the Rahaman measured dataset. The observed deviations also within an acceptable range, suggesting a reasonable match between the database and measured data. For the plane-of-array irradiace $G_{POA}$. Meteonorm underestimates the measured values across most months. This discrepancy can be caused by how irradiance is captured or modeled within the Meteonorm system against the field measurement techniques used in the reference study from Rahaman et al. Despite this, the general trend of seasonal fluctuation is still consistent between the two datasets. Wind speed data also experiences a similar trend, where it is showing a consistent overestimation in the Meteonorm dataset compared to Rahaman et al. measured values. This might be due to the difference in measurement height or regional averaging that is being implemented by Meteonorm model.

Although Meteonorm does not perfectly replicate local measurements, its consistent seasonal trends and availability at an hourly time increment make it suitable for this study's purpose. Since the primary objective is to simulate PV module temperature and corresponding energy yield based on relative seasonal variation in a yearly time range, the Meteonorm dataset offers a practical and justifiable substitute, in the non-existent of measured hourly data. Therefore, the derived weather parameters from Meteonorm are used as input to the PVMD Toolbox to carry out the hourly energy yield simulations.

From these environmental inputs, the results of the PV module temperatures from the 3 assessed thermal models are given in figure 4.8.

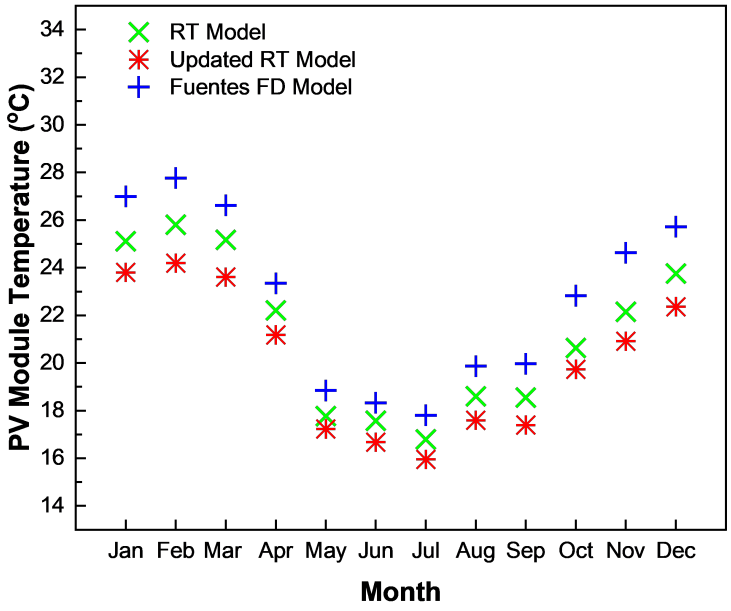


**Figure 4.8:** Simulated PV Module Temperature Comparison for of Rahaman et al. [28] Study Case

The monthly average PV module temperature values shown in figure 4.8 represent the output from the three thermal models assessed in Chapter 2 and Chapter 3. These temperature profiles are derived from the hourly thermal simulations using the same weather inputs. To re-summarize, the Fuentes FD model consistently yields the highest module temperatures across all months, while the Updated RT model, which incorporates CFD-refined heat transfer coefficients, predicts the lowest values.

These temperature datasets serve as key inputs for the PVMD Toolbox simulation, directly replacing the results from the thermal layer in the PVMD Toolbox, which requires PV module temperature values at each hourly timestep to simulate electrical performance and compute energy yield. This enables a direct comparison of how each thermal model influences the electrical output and energy yield predictions of floating PV systems. This integrated approach allows to quantify the impact of thermal behaviour on floating PV system performance, and strengthens the case for applying refined thermal models in energy yield analysis. The energy yield simulation is done for each thermal model in the PVMD Toolbox, and the resulting specific energy yield comparison is given in figure 4.9.

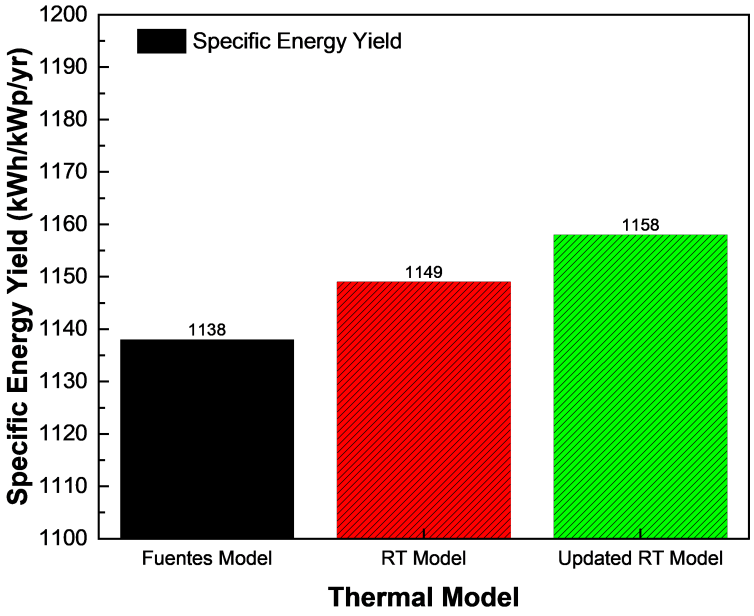


**Figure 4.9:** Specific Energy Yield Comparison Results using PVMD Toolbox

The simulation results obtained from the PVMD Toolbox using hourly PV module tempertaure inputs generated by each assessed thermal model shows consistent trends with the PVsyst simulations discussed in the previous sub-chapter. As illustrated figure 4.9m the Fuentes Fluid Dynamics Model simulated the lowest specific energy yield of 1138 kWh/kWp/year, followed by the Resistive Thermal Model with 1149 kWh/kWp/year, and finallt the Updated Resistive Thermal Model which yielded the highest value of 1158 kWh/kWp/year. This trend is consistent with the observation of energy yield using PVsyst, where the Fuentes Fluid Dynamics Model similarly udnerestimated the PV module cooling effect and resulted in the lowest energy output. On contrary, the Updated RT model captured the cooling effects more effectively and simulated the highest specific energy yield.

Unlike the PVsyst simulations, the PVMD Toolbox simulations in this section utilized hourly weather inputs from Meteonorm database instead of the measured weather data from Rahaman et al. Consequently, direct validation against the measured specific energy yield is not possible. Nonetheless, the relative comparison among thermal models remains valid. The lower yield of the Fuentes Fluid Dynamics Model is attributed to its tendency to overestimate PV module operating temperatures due to its lack of adaptaion to floating PV configurations. The RT model, which incorporates an adjusted thermal resistances due to the presence of water surface shows improved accuracy. The Updated Resistive Thermal Model, which incorporates CFD-derived convective heat loss coefficient demonstrates the best performance by reflecting a more accurate heat transfer dynamics for floating PV application, which results in a highest specific energy yield value.

These consistent findings across both PVsyst and PVMD Toolbox simulations reinforces the conclusion that the Updated Resistive Thermal Model provides the most realistic estimation of PV module temperatures and its corresponding electrical performance, in the form of its specific energy yield. It also highlights the importance of model calibration and adjustments when analyzing non-conventional PV systems such as floating PV configurations. Despite differences in the weather data sources, the agreement in model performance trends once again shows the Updated Thermal Model's robustness and suitability as an improved thermal model, and can also improve energy yield estimation, specific to floating PV applications.

## 4.3. Summary of Key Findings in Chapter 4

In summary, this Chapter's objective is to address the third research question, that is to analyse how does the CFD-Updated Resistive Thermal Model affect the accuracy of energy yield simulations. To achieve this, two different simulation platforms are used, which are the PVMD Toolbox developed by TU Delft and the commercial energy yield simulation software PVsyst. Both tools are utilized to simulate the energy yield based on the PV module temperature results of the CFD-Updated Resistive Thermal Model, enabling a comparative evaluation of the model's prediction accuracy.

The energy yield results show that the CFD-updated Resistive Thermal Model achieves the closest match to the measured specific energy yield, with an error of just 0.10%, compared to 1.75% and 1.27% for the Fuentes FD Model and the initial Resistive Thermal Model, respectively. For the PVMD Toolbox, hourly PV module temperature values are derived using Meteonorm weather data due to the lack of measured hourly data. Although direct comparison with measured energy yield is not possible, a similar performance trend is observed, where the Updated Resistive Thermal Model yields the highest specific energy yield, followed by the initial Resistive Thermal Model and Fuentes FD Model. This consistency between both energy simulation tools reinforces the value of refining analytical thermal models through insight from CFD simulations. These results clearly show that the increase in thermal model accuracy is directly related to a higher accuracy in energy yield simulation, where the energy yield simulation based on the improved thermal model results in a very close agreement with measured values.

# 5

# Computational Fluid Dynamics Study on Multi-Row Floating PV System

This chapter aims to address the fourth research question, that is to analyse how does practical installation scenario, namely differing PV array row spacing, affect the thermal dynamics of floating PV systems. Using the foundation of the analysis on single-module floating PV system in Chapter 3, a broader system-level simulation is done in this chapter to capture thermal interactions between multiple row of PV modules array.

In actual floating PV installations, PV modules are arranged in arrays where thermal behavior can be influenced by flow blockage and heat accumulation. These effects are not captured in isolated single-module CFD simulations, highlighting the importance of extending the simulation scope to a multi-module layout. This chapter is structured to first explore a case study of a 3×3 floating PV matrix with 1 meter row-spacing to investigate how airflow and temperature patterns evolve across a small-scale floating PV farm. Next, the row-spacing are varied to a distance of 1.5 meter and 0.5 meter so that the effect of varying row-spacing to PV module temperature and heat transfer coefficient distribution can be observed.

## 5.1. Base Case of Scenario of 1 meter PV Array Row-Spacing

To systematically assess the thermal characteristics of the PV array, a base case configuration is first established. Figure 5.1 illustrates the geometric setup of the 3x3 floating PV array used in this simulation. This base case consists of nine PV modules arranged in a 3-row by 3-column matrix, each mounted on identical floating platforms and spaced evenly. The tilt angle of the PV modules is set to $15^o$ and the row spacing is fixed at 1 meter, which is representative of common floating PV installation practices. The row spacing is defined as the horizontal distance from the trailing edge of one row to the leading edge of the next row. The airflow enters from the inlet boundary, progresses through the array, and exits at the outlet boundary, allowing analysis of upstream and downstream thermal differences across the farm.

In this simulation, all nine PV modules in the 3×3 matrix are subjected to uniform irradiance input, ensuring that any variation in module temperature across the array can be attributed solely to aerodynamic and thermal flow effects, rather than differences in solar input. This assumption enables a focused analysis on the impact of row position and convective interaction between modules. The boundary conditions for wind speed, air temperature, and water surface temperature are adopted from the January dataset presented in the study by Rahaman et al. [3], which has been previously validated in the previous section. Specifically, the inlet wind velocity is set as 1.64 m/s, the ambient temperature is $21.19^oC$, and the water surface boundary condition is fixed at $24.48^oC$. These environmental parameters serve as the foundation for this base case analysis, enabling consistent comparison with the earlier single-module results.

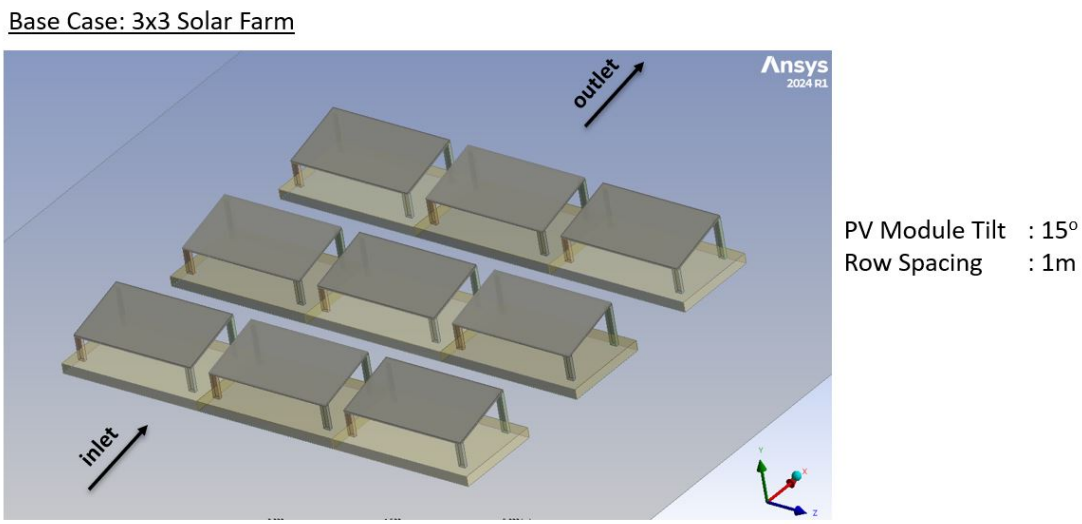


**Figure 5.1:** Multi-Module Simulation Base Case Setup

Figure 5.2 shows the temperature distribution across the nine PV modules in the base case 3×3 floating PV farm configuration. Each module receives equal irradiance input and is exposed to the same environmental boundary conditions. However, a clear temperature gradient is observed across the three rows. PV modules in Row 1 exhibit the lowest average temperature (around 25.8–$25.9^oC$), while modules in Row 3 show the highest temperatures (up to $26.5^oC$). This pattern suggests that PV module position within the farm significantly affects thermal performance, despite identical input conditions.

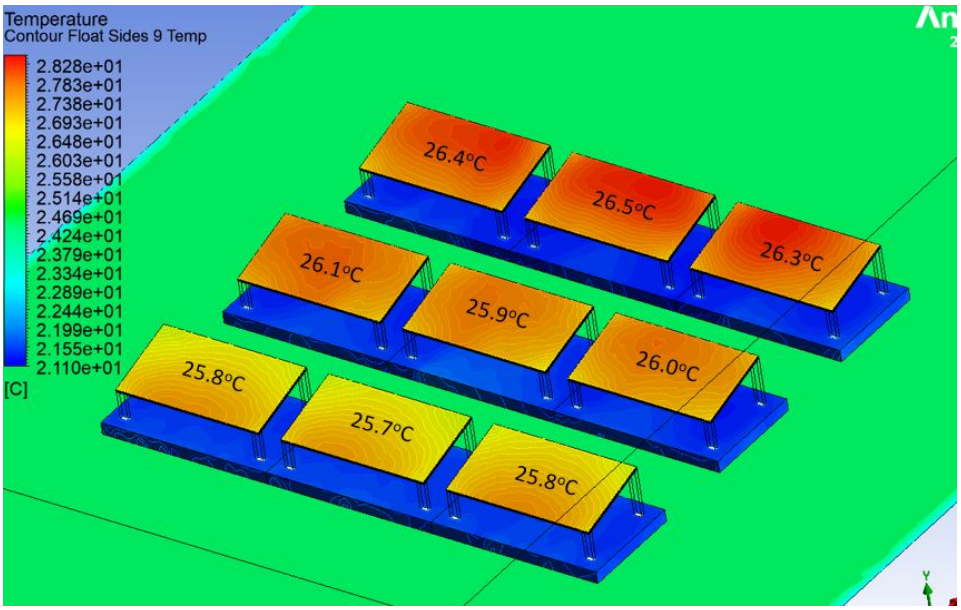


**Figure 5.2:** Temperature Contour Distribution of Base Case Floating PV System

This temperature difference is explained by the airflow behavior illustrated in Figure 5.3. The wind velocity profile, captured from the cross-section, shows that the incoming wind cools Row 1 effectively, but its speed and momentum decrease downstream due to obstruction and dissipation from Row 1. As a result, the wind reaching Rows 2 and 3 is significantly slower, reducing convective cooling effectiveness. This phenomenon leads to a less efficient heat dissipation from these modules, contributing to the higher surface temperatures observed.

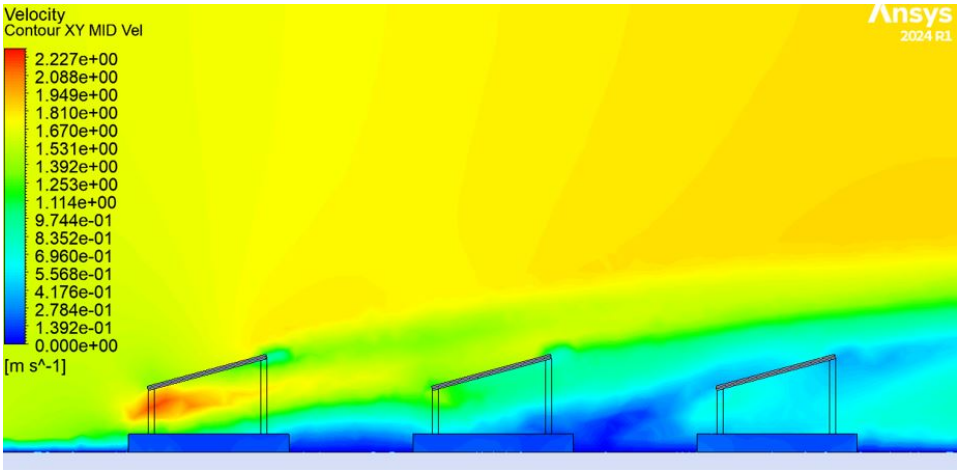


**Figure 5.3:** Wind velocity profile along the rows of the 3×3 floating PV array

Figure 5.4 supports this analysis through the distribution of convective heat transfer coefficient ($h$) values on each PV module. PV modules in Row 1 demonstrate higher $h$ values (approximately 12.9–13.0 W/$m^2K$), while those in Row 3 show lower values (as low as 12.6 W/$m^2K$). This gradient reflects the direct relationship between wind speed and convective cooling performance. Since $h$ is a key parameter in thermal modeling, the decrease in $h$ values further shows the reduced cooling observed in downstream rows.

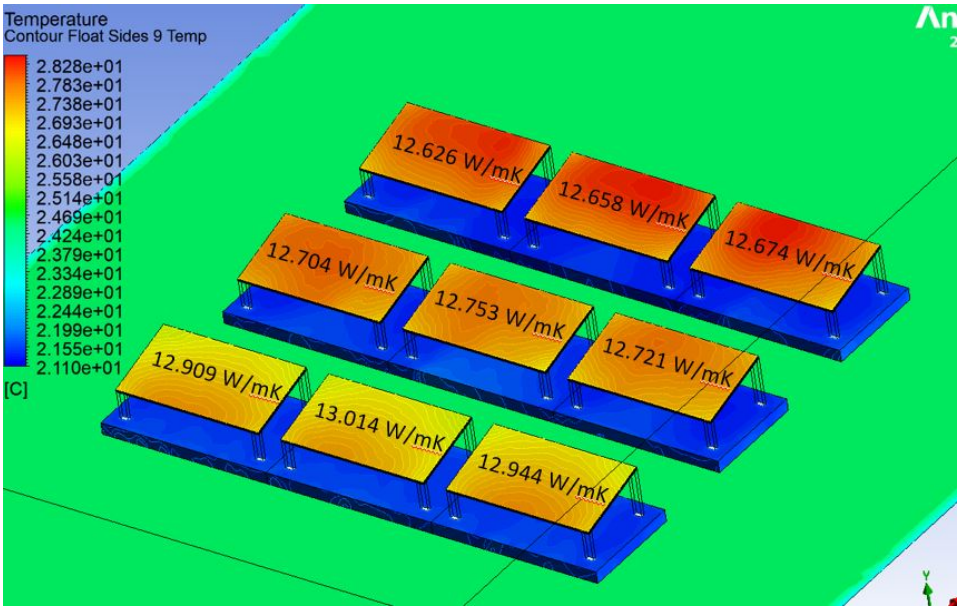


**Figure 5.4:** Convective heat transfer coefficient ($h$) distribution on the surface of each PV module. A clear trend of decreasing $h$ from Row 1 to Row 3 is observed.

These findings highlight the importance of considering inter-row airflow effects in floating PV farms, as temperature gradients caused by airflow obstruction can influence performance, degradation rates, and energy yield across the array.

## 5.2. Analysis of PV Module Array Row-Spacing to PV Module Temperature Distribution

In a floating PV system composed of multiple rows of modules, the spacing between rows plays a significant role in determining the thermal behavior of the modules. As shown in the previous section, as

airflow moves across the array, upstream rows can create wake regions that obstruct airflow to downstream modules, reducing convective heat transfer and leading to elevated operating temperatures in the rear rows. Consequently, optimizing the row spacing becomes a key factor in achieving better thermal uniformity and minimizing performance loss due to temperature gradients.

To investigate this effect, the row spacing is varied around the base case configuration (1.0 m) in this section. Two scenarios are studied: (i) increased spacing to 1.5,m, which is expected to enhance ventilation and reduce thermal buildup in downstream modules, and (ii) decreased spacing to 0.5,m, which may intensify flow blockage and increase module temperatures in rows 2 and 3. The results of these cases are analyzed to assess the impact of row spacing on airflow distribution and module temperature uniformity.

To assess the influence of row spacing on thermal behavior in a floating PV array, the first variation study increases the inter-row distance from 1.0 m (base case) to 1.5 m, while maintaining the same module tilt angle of $15^o$. The tilt angle of the PV modules and all boundary conditions were kept identical to the base case, in order to isolate the effect of row spacing variation on the airflow interaction and heat transfer mechanisms. The simulation setup is shown in Figure 5.5. This adjustment is expected to impact airflow behavior across the PV array, particularly by reducing flow obstruction and wake interference between rows.

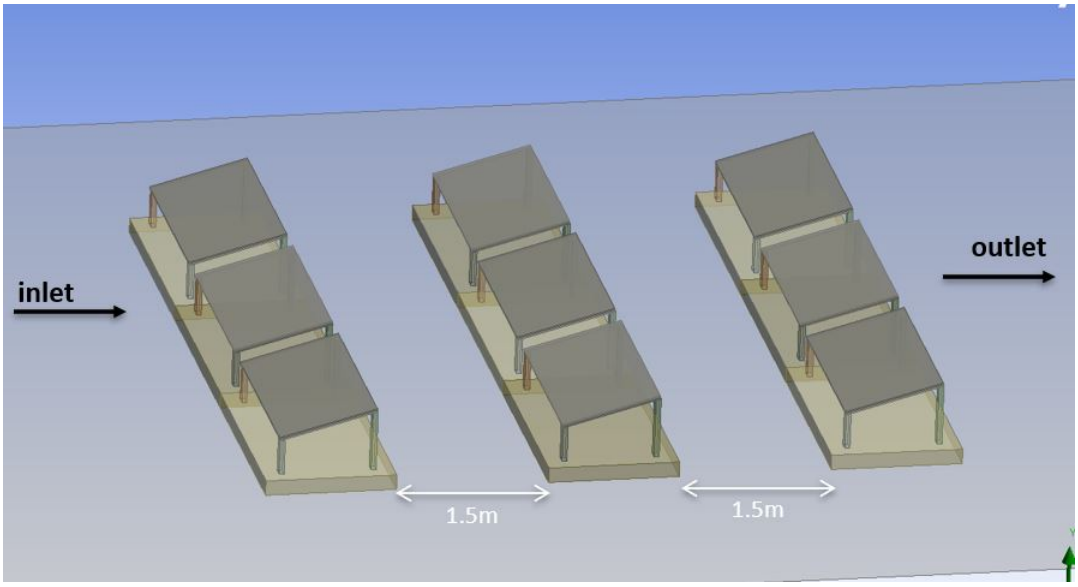


**Figure 5.5:** CFD model setup for 3×3 floating PV array with increased row spacing (1.5m)

Figure 5.6 presents the temperature distribution of the PV modules under the 1.5 m spacing configuration. A similar trend to the base case is observed, where the temperature increases from front to rear rows. However, the temperature difference between Row 1 and Row 2 becomes much smaller, with Row 2 average temperatures nearly matching those of Row 1 (25.7–$25.9^oC$ compared to $25.8^oC$), indicating a more uniform airflow distribution between the first two rows.

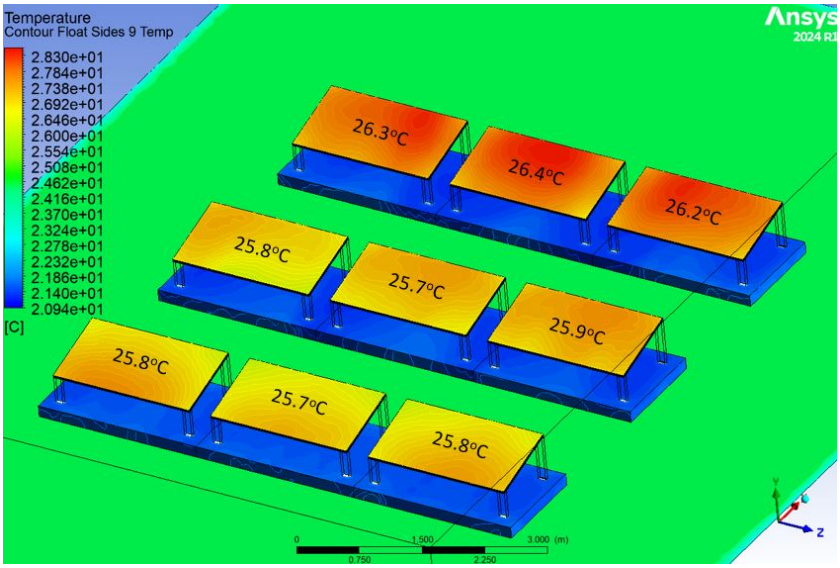


**Figure 5.6:** Temperature contour distribution for row spacing of 1.5 meters

This behavior is better explained through the wind velocity profile shown in Figure 5.7. With increased spacing, Row 2 now receives more wind exposure, as indicated by the larger yellow region of higher air velocity reaching this row. In contrast, Row 3 still remains in a relatively low-velocity zone, hence experiencing reduced convective cooling.

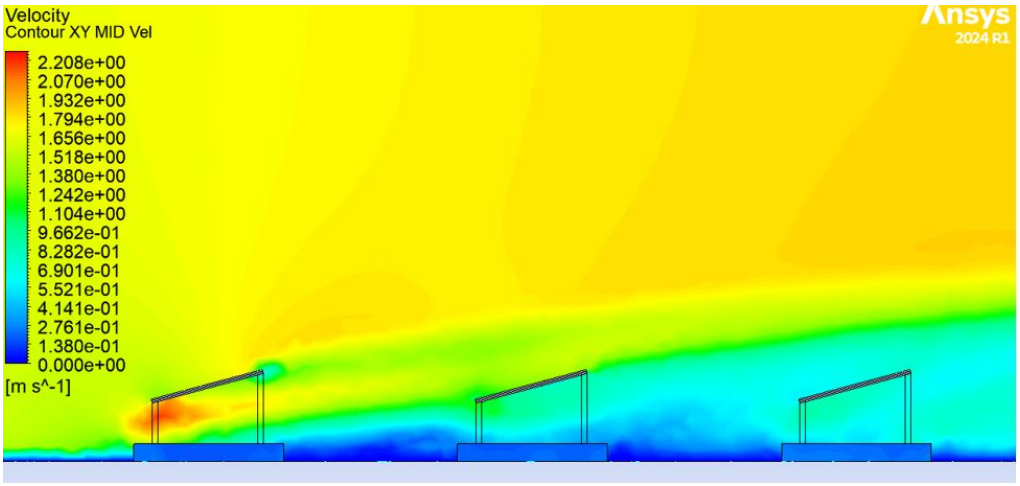


**Figure 5.7:** Wind velocity profile along cross-section of module rows for 1.5 m spacing

The effect of the enhanced airflow is clearly reflected in the distribution of convective heat transfer coefficient h, as shown in Figure 5.8. While Row 1 still exhibits the highest h values (around 12.9–13.0 $W/m^2K$), Row 2 now has significantly higher h values (12.8 $W/m^2K$) compared to the base case ( 12.7 $W/m^2K$). This is consistent with its reduced module temperature and improved convective cooling. Row 3, however, remains with relatively low h values ( 12.6 $W/m^2K$), confirming the continuing wind shadowing effect from the upstream rows.

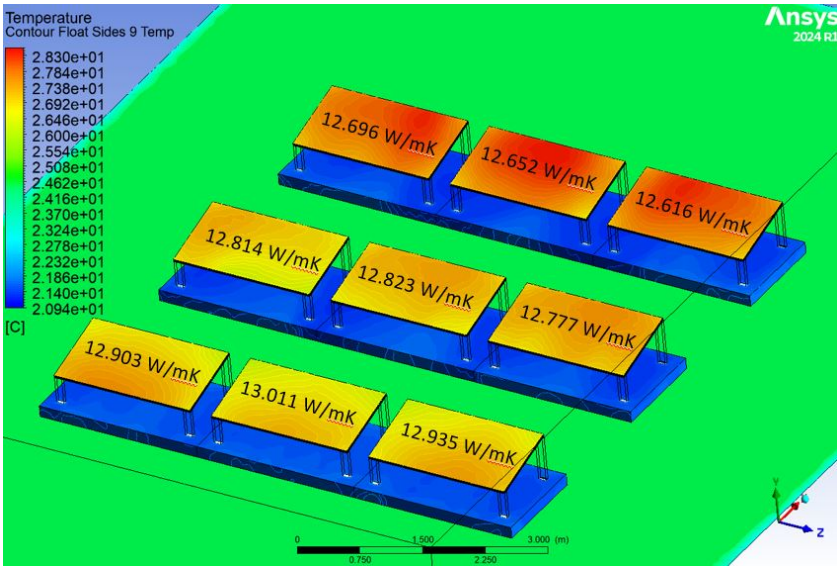


**Figure 5.8:** Convective heat transfer coefficient h distribution for 1.5 meter spacing scenario

In conclusion, increasing the row spacing from 1 meter to 1.5 meters improves airflow penetration to the second row, thereby reducing its temperature and increasing convective heat transfer.

In contrast to the previous variation, this next simulation investigates the impact of reducing the row spacing from 1.0 meter (base case) to 0.5 meter, as illutrated in figure 5.9. The aim is to observe how tighter module arrangements affect airflow dynamics and convective heat dissipation in a floating PV setup. All boundary conditions remain consistent with the base case to isolate the effect of row spacing.

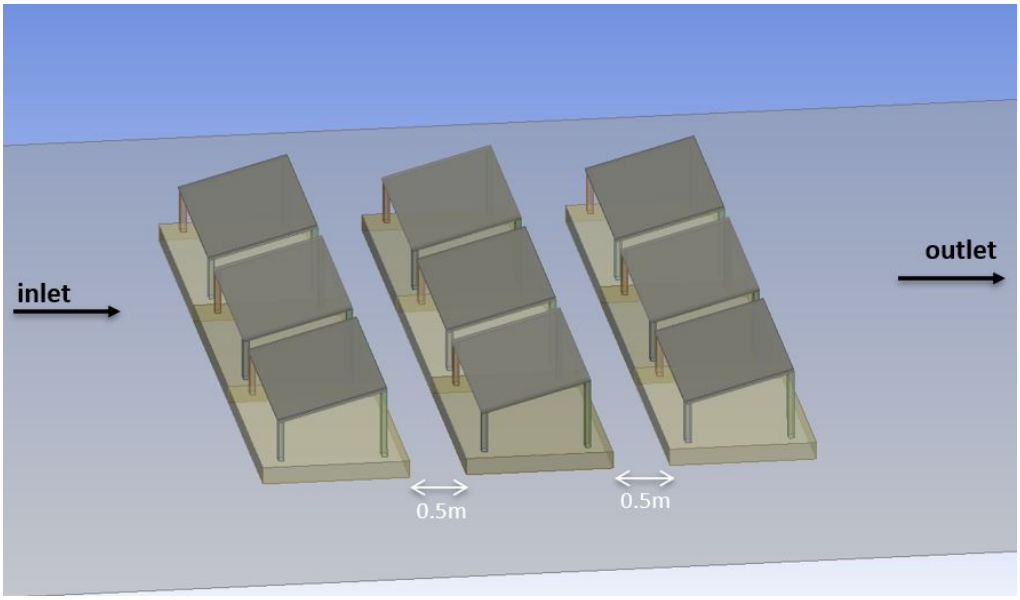


**Figure 5.9:** Simulation setup for row spacing variation case: 0.5 m inter-row distance

The temperature contour result for this configuration is shown in Figure 5.10. Compared to the base case, the upstream row (Row 1) maintains the lowest temperature, while Row 2 shows a temperature increase, nearly matching Row 3, which again records the highest module temperature. The increase in temperature for Row 2 highlights the worsening cooling performance due to wind blockage from the upstream row.

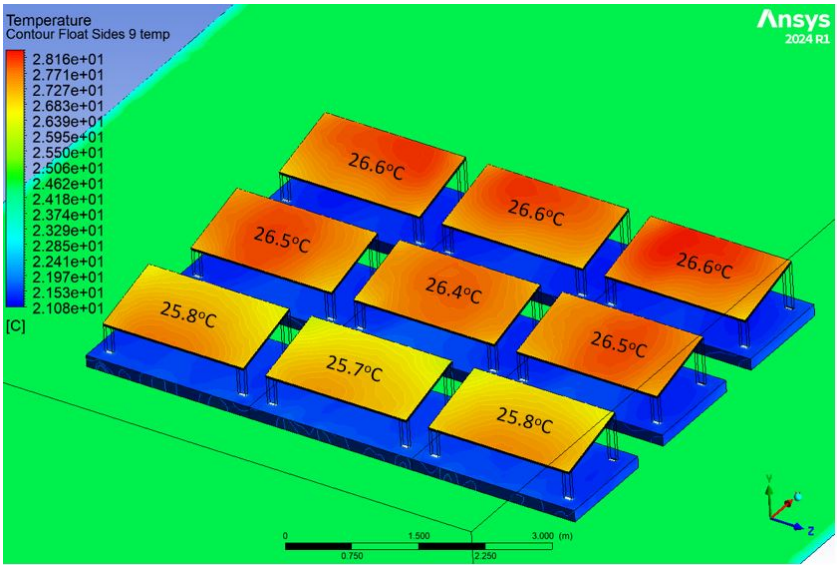


**Figure 5.10:** Temperature distribution across the 3x3 PV system for 0.5 m spacing

The velocity contour in the vertical cross-section, shown in Figure 5.11, provides a clear explanation for the observed temperature rise in downstream modules. The reduced spacing severely limits airflow penetration between rows, resulting in significantly lower wind velocities reaching both Row 2 and Row 3. As a consequence, convective cooling is suppressed for downstream modules, explaining their elevated temperatures.

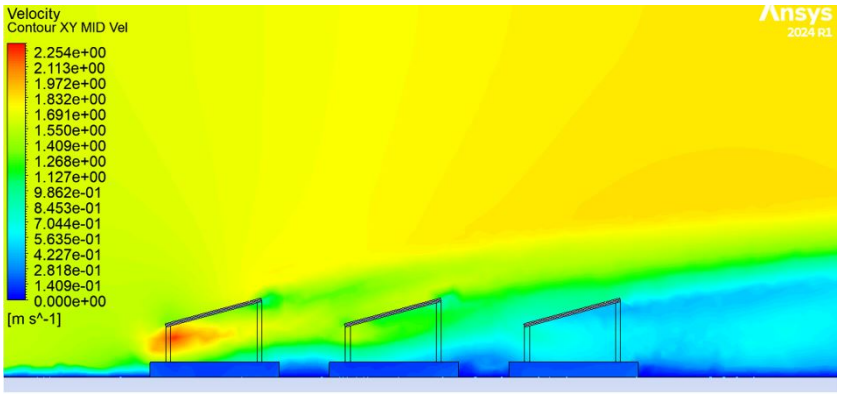


**Figure 5.11:** Wind velocity profile for 0.5 m spacing

The impact of limited airflow is directly reflected in the distribution of convective heat transfer coefficients h, visualized in Figure 5.12. Row 1, exposed to unimpeded wind flow, maintains the highest h values. Meanwhile, Row 2 and Row 3 show reduced h values, indicating weakened convective heat exchange with ambient air. This clearly corresponds to their higher module temperatures.

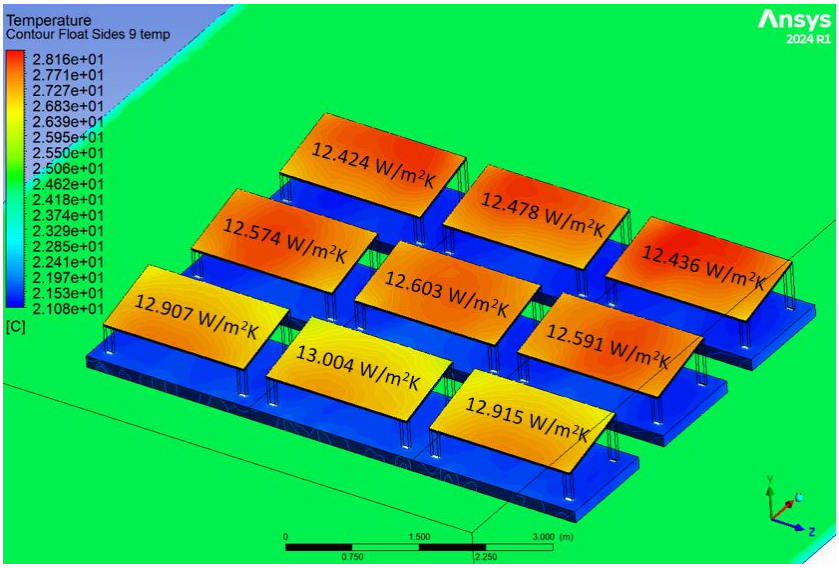


**Figure 5.12:** Distribution of convective heat transfer coefficient h across 3x3 PV array for 0.5 m spacing

The summary of the findings in this secion is summarized by figure 5.13. The graph highlights the relationship between row spacing and the resulting PV module temperatures for each row in a 3x3 floating PV array. It clearly shows that the front row (Row 1), which is directly exposed to the wind, maintains a relatively consistent and low temperature across all spacing scenarios. This is expected, as Row 1 always benefits from unobstructed convective cooling, regardless of how closely spaced the downstream modules are.

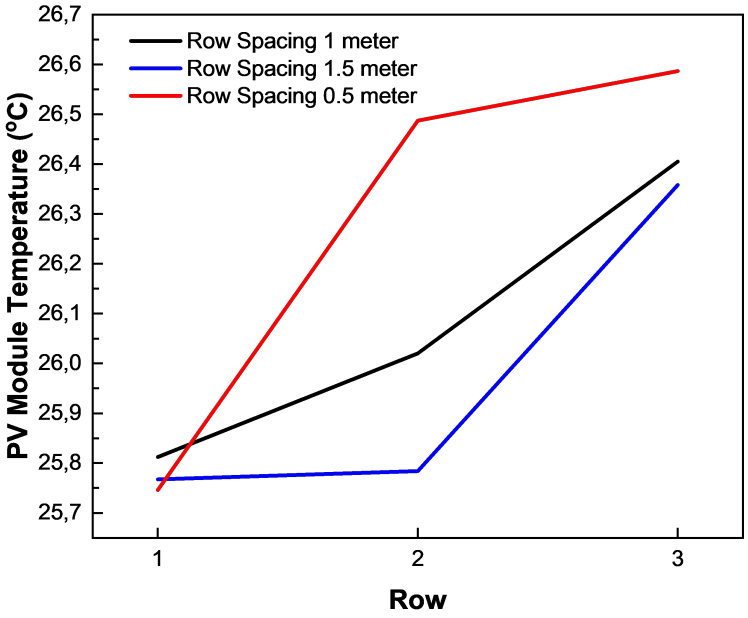


**Figure 5.13:** Summary of PV module temperature distribution across rows for different row spacings

However, the effect of row spacing becomes significantly more pronounced in Row 2 and Row 3. When the row spacing is increased to 1.5 meters, the temperature of Row 2 is nearly the same as Row 1,

indicating strong wind penetration and effective convective heat dissipation. In contrast, reducing the spacing to 0.5 meters leads to a substantial rise in temperature for both Row 2 and Row 3. These findings indicate that tighter spacing restricts airflow between rows, resulting in diminished convective cooling and higher operational temperatures for downstream modules.

In conclusion, the results demonstrate that row spacing is a critical parameter influencing the thermal performance of floating PV systems. While close-proximity PV arrays may offer higher power density per unit area, it comes at the cost of increased module temperatures and potentially reduced energy yield. Therefore, optimizing row spacing is essential to balance land or water surface use efficiency with thermal and consequently, electrical performance.

This chapter demonstrated that the use CFD methods, such as the application of ANSYS Fluent, can provide comprehensive insights in regard to the thermal behaviour in floating PV systems. The single-module simulation study case showed that it is possible to extract specific heat transfer coefficient $h$ from the air-side boundary layer. These values were then used to calculate the corresponding Nusselt numbers, which allows the resistive thermal model to be updated, to better reflect the actual convective heat dissipation surrounding the floating PV modules. The results show that the approach of integrating CFD-derived parameters significantly improved the accuracy of the analytical model for PV module.

In addition to single-module study case, the analysis for multi-row case study also shows valuable insight into the thermal behaviour across PV modules positioned at varying spacing within a PV array. It was observed that reduced wind exposure in downstream rows leads to lower local $h$ values, in which consequently results in higher PV module temperatures. By varying the row spacing, the analysis depicts how airflow blockage and recirculation zones affect cooling performance. These effects establish a relationship between row spacing, convective heat transfer, and PV module temperature distribution. These findings highlight the limitations of uniform parameter assumptions in analytical models and underline the need for row-specific thermal assessment in large-scale floating PV arrays.

The CFD analysis results in this chapter provided detailed thermal insights and enabled an improved thermal models accuracy of the resistive thermal model. However, the key end goal of having a more accurate thermal model is to achieve a higher accuracy in floating PV energy yield simulation. By integrating these updated thermal parameters into energy yield simulations, the analysis in Chapter 4 aims to demonstrate how improved temperature predictions directly affect the accuracy of electrical output estimation.

## 5.3. Summary of Key Findings in Chapter 5

In summary, this Chapter's objective is to address the fourth research question, that is to analyse how does practical installation scenario, specifically differing PV array row spacing, affect the thermal dynamics of floating PV systems. This chapter is structured to first explore a case study of a 3×3 floating PV matrix with 1 meter row-spacing to investigate how airflow and temperature patterns evolve across a small-scale floating PV farm. Next, the row-spacing are varied to a distance of 1.5 meter and 0.5 meter so that the effect of varying row-spacing to PV module temperature and heat transfer coefficient distribution can be observed.

From the the base case study of 1 meter row-spacing, it is revealed that PV modules in Row 1 exhibit the lowest average temperature (around 25.8 to $25.9^oC$), while modules in Row 3 show the highest temperatures (up to $26.5^oC$). This pattern suggests that PV module position within the farm significantly affects thermal performance, despite identical input conditions. This temperature difference is explained by the airflow behavior observed from the wind velocity profile. The wind velocity profile, captured from the cross-section, shows that the incoming wind cools Row 1 effectively, but its speed and momentum decrease downstream due to obstruction and dissipation from Row 1. As a result, the wind reaching Rows 2 and 3 is significantly slower, reducing convective cooling effectiveness. This phenomenon leads to a less efficient heat dissipation from these modules, contributing to the higher surface temperatures observed.

Furthermore, varying the row spacing to 1.5 meter and 0.5 meter revealed that when the row spacing is increased to 1.5 meters, the temperature of Row 2 is nearly the same as Row 1, indicating strong wind penetration and effective convective heat dissipation. In contrast, reducing the spacing to 0.5

meters leads to a substantial rise in temperature for both Row 2 and Row 3. These findings indicate that tighter spacing restricts airflow between rows, resulting in decreased convective cooling and higher operational temperatures for downstream modules.

In conclusion, the results demonstrate that row spacing is a critical parameter influencing the thermal performance of floating PV systems. While close-proximity PV arrays may offer higher power density per unit area, it comes at the cost of increased module temperatures and potentially reduced energy yield. Therefore, optimizing row spacing could be one of the possible future works to balance land or water surface use efficiency with thermal and consequently, electrical performance.

# 6

# Conclusion, Research Limitation, and Recommendation

## 6.1. Conclusion

This study aims to investigate the influence of thermal modelling accuracy on the PV module temperature prediction and energy yield estimation of floating PV systems, with a specific focus on improving the resistive thermal model through insights obtained from Computational Fluid Dynamics (CFD). The research was motivated by the limited applicability and accuracy of conventional land-based PV thermal model such as Fuentes Thermal Model when applied to floating PV applications, which are affected by distinct and unique thermal behaviours due to the presence of water bodies and different convective heat transfer mechanism environments.

To address the main research objective, four main research questions were explored throughout this thesis project. Firstly, this research delved into How do analytical thermal models perform in predicting PV module temperatures for both floating and land-based PV systems. Secondly, analysis was done to discuss How can analytical thermal models be improved to better represent heat transfer mechanisms specific to floating PV systems. Thirdly, How does the CFD-Updated Resistive Thermal Model affect the accuracy of energy yield simulations. Lastly, an extended computational fluid dynamics study is done to analyse how does practical installation scenario, specifically differing PV array row spacing, affect the thermal dynamics of floating PV systems

In response to the first research question, Chapter 2 evaluated two physics-based analytical thermal models, which are the existing Fuentes Thermal Model that is used by default in the PVMD Toolbox and the newly-developed alternative analytical model which is the Resistive Thermal Model. The results showed that **while the Fuentes Fluid Dynamics could predict land-based PV module temperatures with reasonably good accuracy, it exhibited significant deviations relative to the measured PV module temperature values when applied to floating PV systems**. For floating PV system, applying Fuentes Thermal Model to floating PV systems result in a relatively low accuracy, with RMSE value of $2.30^oC$ for the base case study. This discrepancy was attributed to the unique convective environment of floating PV systems, particularly the air-water interaction and wind behaviour near the water surface. Resistive Thermal Model has been successfully developed for diverse floating PV configurations, namely Horizontal Pontoon with Truss (HPOT), Horizontal Pipe with Truss (HPIT), and Membrane Ring floating PV. The results of the newly-developed **Resistive Thermal Model, on the other hand, shows a notable increase in accuracy compared with the Fuentes Thermal Model, shown by the relatively lower root mean square error (RMSE) value calculated relative to the measured PV module temperatures across all assessed floating PV configurations**. For the base case study, the RMSE of Resistive Thermal Model decreases further to $1.70^oC$. These findings shows a notable improvement of the prediction accuracy of analytical thermal models. However, relatively high RMSE values can still be observed even with Resistive Thermal Model, particularly in high water-exposure floating PV systems.

To improve upon these models, Chapter 3 aims to address the second research question, that is to analyse how can analytical thermal models be improved to better represent heat transfer mechanisms specific to floating PV systems. This question focuses on investigating the role of Computational Fluid Dynamics (CFD) tool such as ANSYS Fluent in capturing detailed convective, conductive, and radiative effects influenced by water proximity and ambient cooling. The CFD simulation setup has been successfully validated. These validated model that are used include the energy model, turbulence model, as well as the thermal boundary layer for air-water interface.**The findings revealed that by incorporating the updated Nu values specific to floating PV application into the Resistive Thermal Model, the thermal model's accuracy can significantly be improved. The PV module temperature prediction accuracy is quantified by the RMSE value for the CFD-Updated Resistive Thermal Model of $0.72^oC$, which shows significant improvement from the initial Resistive Thermal Model RMSE for the base case study of $1.70^oC$.** This approach answers the second research question, showing that integrating the insights of CFD into analytical approach, in this case the Resistive Thermal Model results in a further improvement in PV module temperature prediction accuracy. This method effectively combines the computational-cost effectiveness of the Resistive Thermal Model and the robustness of computational fluid dynamics approaches.

These combined thermal modelling approach provided a solid foundation for energy yield modelling, as presented in Chapter 4. Chapter 4 aims to address the third research question, that is to analyse how does the CFD-Updated Resistive Thermal Model affect the accuracy of energy yield simulations. The energy yield results show that the CFD-updated Resistive Thermal Model achieves the closest match to the measured specific energy yield, with an error of just 0.10%, compared to 1.75% and 1.27% for the Fuentes FD Model and the initial Resistive Thermal Model, respectively. These findings are further reinforced by the results from energy yield simulation using PVMD Toolbox, that re-affirms that the **CFD-Updated Resistive Thermal Model shows an significant increase in energy yield prediction accuracy, compared to Fuentes Thermal Model and the Initial Resistive Thermal Model**. These results clearly show that the increase in thermal model accuracy is directly related to a higher accuracy in energy yield simulation, where the energy yield simulation based on the improved thermal model results in a very close agreement with measured values.

In Chapter 5, the objective is to address the fourth research question, that is to analyse how does practical installation scenario, specifically differing PV array row spacing, affect the thermal dynamics of floating PV systems. From the the base case study of 1 meter row-spacing, it is revealed that PV modules in Row 1 exhibit the lowest average temperature (around 25.8 to $25.9^oC$), while modules in Row 3 show the highest temperatures (up to $26.5^oC$). varying the row spacing to 1.5 meter and 0.5 meter revealed that when the row spacing is increased to 1.5 meters, the temperature of Row 2 is nearly the same as Row 1, indicating strong wind penetration and effective convective heat dissipation. In contrast, reducing the spacing to 0.5 meters leads to a substantial rise in temperature for both Row 2 and Row 3. These findings indicate that tighter spacing restricts airflow between rows, resulting in decreased convective cooling and higher operational temperatures for downstream modules. In conclusion, the results demonstrate that **while close-proximity PV arrays with small row-spacing may offer higher power density per unit area, it comes at the cost of increased PV module temperatures and potentially reduced energy yield. On the contrary, large-proximity PV arrays with large row-spacing results in a lower overall PV module temperatures that potentially increase energy yield of the floating PV system**. Therefore, optimizing row spacing could be one of the possible future works to balance land or water surface use efficiency with thermal and consequently, electrical performance.

Overall, this study successfully addresses the main research objective, which is to develop, validate, and apply improved thermal models that accurately capture the temperature behaviour of floating PV systems in comparison to land-based PV systems, thereby enabling more accurate energy yield simulations. Chapter 2 demonstrated how the newly-developed Resistive Thermal Model results in an increased PV module temperature prediction accuracy relative to the existing Fuentes Thermal Model. Chapter 3 further improved the Resistive Thermal Model's accuracy by integrating key heat transfer parameters extracted from the CFD simulation of floating PV systems, effectively combining the robustness of CFD approach with the computational cost-effectiveness of Resistive Thermal Model. Chapter 4 shows that the higher thermal model accuracy is directly reflected by the higher accuracy of energy yield modelling. Finally, Chapter 5 completes the research with extended CFD study on practical-scale

PV farm with multiple PV module, showing the significance of row-spacing designs to the PV module temperature distribution.

## 6.2. Research Limitations and Recommendations for Future Works

While this study has demonstrated the value of improving the thermal models in increasing PV module temperature prediction accuracy, as well as the energy yield estimation for floating PV system, several limitations should be acknoweledged. This sub-section will discuss and identify the limitations of this thesis research, and also the possible pathways for future research.

Firstly, this research faced challenges with regard to the limited validation with measured data. The validation process of the assesses thermal models relied on a relatively limited dataset of real-world measurement of PV module temperatures. These measurements were only available for specific time increments and a constrained time range. Consequently, this limits the extent to which the models could be statistically verified and validated. For the future recommendation, expanding the validation to include more extensive and continous field measurements across different months of the year and operating conditions would improve the robustness, credibility, and generalizability of the findings in the future research.

In conjunction with the limited measurement scope, the number of data points used fo CFD simulations and model fitting was also limited. As a result, the statistical certainty of the observed trends, such as accuracy improvments of the Updated Resistive Thermal Model, may not fully reflect real-world variability and uncertainty. In line with previous recommendation, future research works could increase the number of analyzed data points across wider time-scales, for example different seasons or multiple years. This would not only enhance the reliability of the conclusions, but also allow better tuning of thermal model parameters.

Moreover, in Chapter 3, CFD simulations consequently led to the extraction of specific convective heat transfer coefficient $h$ and their corresponding Nusselt number $Nu$ values. However, due to the limited number of case studies it was not possible to formulate a general Nusselt number correlation. Conducting additional CFD simulations across varying wind speeds, PV module configurations, and ambient conditions could enable the development of an empirical or semi-empirical Nusselt number correlation. These Nusselt number correlation would significantly enhance the generalizability and reusability of the Updated Resistive Thermal Model for different floating PV scenarios.

Next, although Chapter 2 introduced multiple floating PV archetypes based on floating structure and configuration, the CFD simulations and energy yield assessments were only conducted on a single archetype. Therefore, the derived conclusions may not be representative of all floating PV design variants. Extending the CFD modelling and its corresponding thermal analysis to other floating PV archetypes as listed in Chapter 2 would allow comparison of their respective thermal behaviours and help in optimizing each configuration individually.

Furthermore, the simulations and validation were conducted under a specific set of weather conditions, based on the reference study's site and climate. While this establishes a solid baseline, the thermal dynamics of floating PV systems may vary under different climatic conditions. For example, comparisons between tropical against temperate, or humid against arid climatic conditions would be insightful for an extended scope of study. Performing similar thermal modelling and energy yield assessments under diverse climate scenarios would provide insight into how weather patterns influence PV module temperature and performance, supporting the development of more adaptive thermal models.

Lastly, in Chapter 4, energy yield simulations that was done using PVMD Toolbox are lacking measured PV module temperature and its subsequent specific energy yield to serve as a reference point. As a result, it was not possible to calculate and evaluate the absolute specific energy yield accuracy of the PVMD Toolbox results, as well as making a fully consistent comparison withe PVsyst-based simulations. Integrating a dataset that includes both hourly measured PV module temperatures and actual energy yield data would allow a more rigorous validation of the PVMD Toolbox workflow and ebale a direct comparison with the PVsyst modelling approach.

# References


[1] International Renewable Energy Agency. *Renewable Energy Capacity Statistics 2023*. IRENA, 2023.

[2] Intergovernmental Panel for Climate Change. *Synthesis Report. Contribution of Working Groups I, II, and III to the Sixth Assessment Report of the Intergovernmental Panel on Climate Change*. IPCC, 2023.

[3] International Renewable Energy Agency. *Renewable Power Generation Costs in 2022*. IRENA, 2023.

[4] International Energy Agency. *Renewables 2023: Analysis and Forecast to 2028*. IEA, 2023.

[5] et.al. A. Brown. "The Land Use Challenge of Solar PV". In: *Energy Policy* 89 (2019), pp. 29–35.

[6] et.al. J Smith. "Overview of Photovoltaic Systems". In: *Journal of Renewable Energy Technology* 5.2 (2020), pp. 112–122.

[7] National Renewable Energy Laboratory. *The Renewable Energy Potential Model: A Geospatial Platform for Technical Potential and Supply Curve Modelling*. NREL, 2021.

[8] World Economic Forum. *How Much of Earth's Surface is Covered by Each Country*. WEF, 2021.

[9] et.al. P Green. "Innovations in Building-Integrated Photovoltaics". In: *Building Science Review* 10.3 (2021), pp. 211–223.

[10] van Sark W. Golroodbari S.Z. "Simulation of performance differences between offshore and land-based photovoltaic systems". In: *Prog. Photovoltaics Res. Appl.* 28 (2020), pp. 873–886.

[11] W.G. Hurley S. Armstrong. "A thermal model for photovoltaic panels under varying atmospheric conditions". In: *Applied Thermal Engineering* 30 (2010), pp. 1488–1495.

[12] H. Lina H. Lib Q. Suna R. Wennersten L. Liu Q. Wang. "Power generation efficiency and prospects of floating photovoltaic systems". In: *Energy Production* 105 (2017), pp. 1136–1142.

[13] A. H. Ibrahim. "Temperature Effects on Solar Panel Efficiency". In: *Solar Energy Engineering* 40 (2019), pp. 123–130.

[14] K. Trapani and M. Santafé. "Floating Solar Panels: A Review of the Benefits and Potential Applications". In: *Solar Energy* 120 (2020), pp. 95–107.

[15] Y. Lin and R. Wang. "Dust Mitigation in PV Systems: A Comparative Study". In: *Clean Energy Technology Review* 12 (2022), pp. 60–71.

[16] J. A. Duffie and W. A. Beckman. *Solar Engineering of Thermal Processes*. 4th. NJ USA: Wiley, 2013.

[17] M. W. Beckman. "Thermal Modelling for PV System Efficiency". In: *Solar Energy Research Journal* 60 (2018), pp. 87–94.

[18] J. A. Duffie and W. A. Beckman. "Advanced Empirical Thermal Models for PV Performance". In: *Journal of Solar Engineering* 42.3 (2020), pp. 145–152.

[19] Sandia National Laboratories. *Sandia temperature model for photovoltaic modules and arrays*. SNL, 2006.

[20] D. Faiman. "Assessing the Outdoor Operating Temperature of Photovoltaic Modules". In: *Progress in Photovoltaics: Research and Applications* 6.2 (2020).

[21] et.al S. Dorenkamper. "Evaluation of Thermal Performance for PV Systems in Diverse Climates". In: *Renewable Energy* 150 (2020), pp. 673–683.

[22] et.al A. Kjeldstad. "Statistical Analysis of U-values for PV Systems in Sri Lanka, Netherlands, and Singapore". In: *Journal of Solar Energy Engineering* 142.6 (2020).

[23] et.al N. Elminshawy. “Thermal Behavior of Floating and Partially Submerged PV Systems”. In: *Applied Energy* 239 (2019), pp. 342–354.

[24] Olindo Isabella Rene ACMM Van Swaaij Miro Zeman Arno HM Smets Klaus Jager. *Solar Energy: The Physics and Engineering of Photovoltaic Conversion Technologies and Systems*. UIT Cambridge, England, 2015.

[25] M.K. Fuentes. *A simplified thermal model for flat-plate photovoltaic arrrays*. Sandia National Laboratories, 1987.

[26] A. M. Alharbi et al. “A Review of Thermal Models for Photovoltaic Systems”. In: *Renewable and Sustainable Energy Reviews* 127 (2020).

[27] Palyvos J. A. Skoplaki E. “Temperature dependence of photovoltaic module electrical performance: A review of efficiency/power correlations”. In: *Solar Energy* 83.5 (2009), pp. 614–624.

[28] et al. A. Rahaman. “Thermal Management in Floating Photovoltaic Systems”. In: *Renewable Energy Journal* 145 (2020), pp. 1883–1891.

[29] R. Santbergen O.Isabella S.S. Vasuki L.Jack. “A Technical Review on the Energy Yield Estimation of Offshore Floating Photovoltaics Systems”. In: (2024).

[30] Yadav N. Sudhakar K. Sahu A. “Floating photovoltaic power plant: A review”. In: *Renewable and Sustainable Energy Reviews* 66 (2016), pp. 815–824.

[31] et al. B. Willemse. “A Comparative Evaluation of Heat Dissipation Factors for open-rack and floating solar pv installations”. In: (2024).

[32] Cicu M. Rosa-Clot M. Rosa-Clot P. Tina G. M. Scandura P. F. Cazzaniga R. “Floating photovoltaic plants: Performance analysis and design solutions”. In: *Renewable and Sustainable Energy Reviews* 81 (2018), pp. 1730–1741.

[33] Yoon S. Choi Y. K. Lee J. “Design and performance evaluation of a floating photovoltaic system with a flexible membrane structure”. In: *Energies* 13.3 (2020), p. 702.

[34] Rosa-Clot M. Rosa-Clot P.- Tina G. M. Cazzaniga R. “Integration of PV floating with hydroelectric power plants”. In: *Heliyon* 2.5 (2018), e01918.

[35] Y. K. Choi. “A study on power generation analysis of floating PV system considering environmental impact”. In: *International Journal of Software Engineering and Its Applications* 8.1 (2014), pp. 75–84.

[36] Ghajar A. J. Çengel Y. A. *Heat and Mass Transfer: Fundamentals and Applications*. 5th. McGraw-Hill Education, 2015.

[37] Beven K. Freer J. Hall J. W. Rougier J. Stephenson D. B. Wagener T. Pianosi F. “Sensitivity analysis of environmental models: A systematic review with practical workflow”. In: *Environmental Modelling Software* 79 (2016), pp. 214–232.

[38] Yoshida H. Mian A. “Optimization of solar PV system for various load profiles and locations using sensitivity analysis”. In: *Solar Energy* 83.4 (2009), pp. 603–612.

[39] H. K. Veersteg W. Malalasekera. *An Introduction to Computational Fluid Dynamics*. 2nd ed. Pearson Prentice Hall, 2007.

[40] F.M. White. *Viscous Fluid Flow*. 3rd ed. 2006.

[41] David P. Dewitt Frank P. Incropera. *Fundamentals of Heat and Mass Transfer*. 6th ed. John Wiley Sons, 2011.

[42] ANSYS Inc. *ANSYS Fluent User’s Guide*. R1. ANSYS Inc., 2024.

[43] Seetharam Rajendra Prasad Sathya Sai and Adithya Garimella. “Numerical Predictions of Laminar Forced Convection Heat Transfer with and without Buoyancy Effects from an Isothermal Horizontal Flat Plate to Supercritical Nitrogen”. In: *Frontiers in Heat and Mass Transfer* (2024).

[44] Yousouf Alhendal Sara Touzani. “Forced Convection over an Inclined Heated Plate with Varying Aspect Ratios: 3D Numerical and Experimental Investigations”. In: *International Journal of Heat and Technology* 42.4 (2014), pp. 1111–1119.

# A

# Measured Environmental Input Data From Reference Studies

**1. Ground Mounted PV System Located in the Netherlands [21]**

**Table A.1:** Ground Mounted PV System Located in the Netherlands

| Date | Time | Ambient Temp. [°C] | Wind Velocity [m/s] | Irradiance [W/m$^2$] | Module Temp. [°C] |
|---|---|---|---|---|---|
| 21-Jun | 06:00 | 9.87 | 3.30 | 280.33 | 16.68 |
| | 07:00 | 10.94 | 4.30 | 428.03 | 19.79 |
| | 08:00 | 12.17 | 4.80 | 594.81 | 23.64 |
| | 09:00 | 13.32 | 5.30 | 667.87 | 25.38 |
| | 10:00 | 14.36 | 4.60 | 713.52 | 28.56 |
| | 11:00 | 15.30 | 3.60 | 750.98 | 32.80 |
| | 12:00 | 16.19 | 3.10 | 756.08 | 35.44 |
| | 13:00 | 16.91 | 2.80 | 713.54 | 36.14 |
| | 14:00 | 17.50 | 1.60 | 647.38 | 40.24 |
| | 15:00 | 17.80 | 1.90 | 504.55 | 34.22 |
| | 16:00 | 17.78 | 2.20 | 331.25 | 27.83 |
| | 17:00 | 17.44 | 1.70 | 191.01 | 23.94 |
| | 18:00 | 16.80 | 1.70 | 86.56 | 19.76 |

**2. Rooftop PV System Located in the Netherlands [21]**

**3. Floating PV System Located in Brazil[28]**

**4. HPOT Large Floater Footprint Floating PV System Located in the Netherlands [21]**

**5. HPOT Medium Floater Footprint Floating PV System Located in South Africa [31]**

**6. HPOT Small Floater Footprint Floating PV System Located in Singapore [21]**

**7. HPIT Small Floater Footprint Floating PV System Located in the Netherlands [21]**

**8. Membrane Ring Floating PV System Located in Norway [22]**

**Table A.2:** Rooftop PV System Located in the Netherlands

| Date | Time | Ambient Temp. [°C] | Wind Velocity [m/s] | Irradiance [W/m$^2$] | Module Temp. [°C] |
|---|---|---|---|---|---|
| 21-Jun | 06:00 | 9.87 | 3.30 | 280.33 | 11.49 |
| | 07:00 | 10.94 | 4.30 | 428.03 | 15.33 |
| | 08:00 | 12.17 | 4.80 | 594.81 | 20.05 |
| | 09:00 | 13.32 | 5.30 | 667.87 | 23.52 |
| | 10:00 | 14.36 | 4.60 | 713.52 | 27.73 |
| | 11:00 | 15.30 | 3.60 | 750.98 | 32.77 |
| | 12:00 | 16.19 | 3.10 | 756.08 | 36.58 |
| | 13:00 | 16.91 | 2.80 | 713.54 | 38.45 |
| | 14:00 | 17.50 | 1.60 | 647.38 | 43.63 |
| | 15:00 | 17.80 | 1.90 | 504.55 | 38.16 |
| | 16:00 | 17.78 | 2.20 | 331.25 | 31.04 |
| | 17:00 | 17.44 | 1.70 | 191.01 | 26.55 |
| | 18:00 | 16.80 | 1.70 | 86.56 | 20.65 |

**Table A.3:** Floating PV System Located in Brazil

| Year | Month | Ambient Temp. [°C] | Wind Velocity [m/s] | Irradiance [W/m$^2$] | Module Temp. [°C] |
|---|---|---|---|---|---|
| 2023 | January | 21.19 | 1.64 | 180.43 | 25.95 |
| | February | 20.89 | 1.43 | 256.36 | 27.61 |
| | March | 21.10 | 1.50 | 191.75 | 26.41 |
| | April | 17.63 | 0.96 | 157.45 | 22.00 |
| | May | 15.60 | 1.35 | 137.17 | 19.18 |
| | June | 14.04 | 1.27 | 108.24 | 16.77 |
| | July | 11.70 | 1.56 | 156.05 | 14.78 |
| | August | 15.23 | 1.24 | 143.92 | 17.89 |
| | September | 17.75 | 1.50 | 179.45 | 22.15 |
| | October | 16.47 | 1.45 | 138.34 | 20.15 |
| | November | 19.39 | 1.61 | 241.21 | 25.42 |
| | December | 20.17 | 1.33 | 253.66 | 26.63 |

**Table A.4:** HPOT Large Floater Footprint Floating PV System Located in the Netherlands

| Date | Time | Ambient Temp. [°C] | Wind Velocity [m/s] | Irradiance [W/m$^2$] | Module Temp. [°C] |
|---|---|---|---|---|---|
| 21-Jun | 06:00 | 9.87 | 3.30 | 280.33 | 15.48 |
| | 07:00 | 10.94 | 4.30 | 428.03 | 18.73 |
| | 08:00 | 12.17 | 4.80 | 594.81 | 22.55 |
| | 09:00 | 13.32 | 5.30 | 667.87 | 24.51 |
| | 10:00 | 14.36 | 4.60 | 713.52 | 27.08 |
| | 11:00 | 15.30 | 3.60 | 750.98 | 30.00 |
| | 12:00 | 16.19 | 3.10 | 756.08 | 31.76 |
| | 13:00 | 16.91 | 2.80 | 713.54 | 32.07 |
| | 14:00 | 17.50 | 1.60 | 647.38 | 33.23 |
| | 15:00 | 17.80 | 1.90 | 504.55 | 29.61 |
| | 16:00 | 17.78 | 2.20 | 331.25 | 25.26 |
| | 17:00 | 17.44 | 1.70 | 191.01 | 22.01 |
| | 18:00 | 16.80 | 1.70 | 86.56 | 18.89 |

**Table A.5:** HPOT Medium Floater Footprint Floating PV System Located in South Africa

| Date | Time | Ambient Temp. [°C] | Wind Velocity [m/s] | Irradiance [W/m$^2$] | Module Temp. [°C] |
|---|---|---|---|---|---|
| 31-Aug | 10:00 | 18.03 | 5.56 | 629.48 | 23.83 |
| | 10:30 | 18.87 | 5.68 | 719.12 | 26.43 |
| | 11:00 | 19.61 | 4.72 | 796.81 | 29.24 |
| | 11:30 | 20.24 | 5.22 | 862.55 | 30.60 |
| | 12:00 | 21.19 | 4.50 | 902.39 | 33.41 |
| | 12:30 | 21.92 | 3.59 | 930.28 | 35.91 |
| | 13:00 | 23.08 | 3.27 | 932.27 | 38.93 |
| | 13:30 | 23.30 | 4.12 | 918.33 | 36.67 |
| | 14:00 | 23.83 | 3.65 | 882.47 | 37.30 |

**Table A.6:** HPOT Small Floater Footprint Floating PV System Located in Singapore

| Date | Time | Ambient Temp. [°C] | Wind Velocity [m/s] | Irradiance [W/m$^2$] | Module Temp. [°C] |
|---|---|---|---|---|---|
| 21-Jun | 07:00 | 27.54 | 0.90 | 12.20 | 27.82 |
| | 08:00 | 28.03 | 0.50 | 83.10 | 29.84 |
| | 09:00 | 28.87 | 0.20 | 230.32 | 33.88 |
| | 10:00 | 29.63 | 0.10 | 331.35 | 36.85 |
| | 11:00 | 30.68 | 0.10 | 554.41 | 42.82 |
| | 12:00 | 31.20 | 0.10 | 467.62 | 41.41 |
| | 13:00 | 31.65 | 0.30 | 499.01 | 42.50 |
| | 14:00 | 31.64 | 0.50 | 392.97 | 40.14 |
| | 15:00 | 32.06 | 0.60 | 384.98 | 40.37 |
| | 16:00 | 31.80 | 0.90 | 285.20 | 37.91 |
| | 17:00 | 31.58 | 0.80 | 193.17 | 35.73 |
| | 18:00 | 31.09 | 1.60 | 55.03 | 32.27 |

**Table A.7:** HPOT Large Floater Fooprint Floating PV System Located in the Netherlands

| Date | Time | Ambient Temp. [°C] | Wind Velocity [m/s] | Irradiance [W/m$^2$] | Module Temp. [°C] |
|---|---|---|---|---|---|
| 21-Jun | 06:00 | 9.87 | 3.30 | 280.33 | 14.44 |
| | 07:00 | 10.94 | 4.30 | 428.03 | 17.05 |
| | 08:00 | 12.17 | 4.80 | 594.81 | 20.18 |
| | 09:00 | 13.32 | 5.30 | 667.87 | 21.82 |
| | 10:00 | 14.36 | 4.60 | 713.52 | 24.22 |
| | 11:00 | 15.30 | 3.60 | 750.98 | 27.12 |
| | 12:00 | 16.19 | 3.10 | 756.08 | 28.98 |
| | 13:00 | 16.91 | 2.80 | 713.54 | 29.54 |
| | 14:00 | 17.50 | 1.60 | 647.38 | 31.55 |
| | 15:00 | 17.80 | 1.90 | 504.55 | 28.14 |
| | 16:00 | 17.78 | 2.20 | 331.25 | 24.22 |
| | 17:00 | 17.44 | 1.70 | 191.01 | 21.50 |
| | 18:00 | 16.80 | 1.70 | 86.56 | 18.65 |

**Table A.8:** Membrane Ring Floating PV System Located in Norway

| Date | Time | Ambient Temp. [°C] | Wind Velocity [m/s] | Irradiance [W/m$^2$] | Module Temp. [°C] |
|---|---|---|---|---|---|
| 21-Jun | 06:00 | 10.09 | 1.00 | 49.15 | 10.18 |
| | 07:00 | 16.00 | 1.00 | 188.03 | 10.70 |
| | 08:00 | 15.02 | 1.00 | 267.09 | 11.68 |
| | 09:00 | 17.08 | 1.00 | 416.67 | 12.73 |
| | 10:00 | 12.05 | 1.00 | 532.05 | 13.92 |
| | 11:00 | 13.06 | 1.00 | 617.52 | 15.12 |
| | 12:00 | 14.04 | 1.00 | 675.21 | 16.25 |
| | 13:00 | 16.07 | 1.00 | 700.85 | 17.29 |
| | 14:00 | 17.02 | 1.00 | 696.58 | 19.86 |
| | 15:00 | 18.03 | 1.00 | 696.58 | 18.67 |
| | 16:00 | 19.04 | 1.00 | 215.81 | 15.97 |
| | 17:00 | 18.03 | 1.00 | 239.32 | 14.56 |
| | 18:00 | 14.99 | 1.00 | 153.85 | 16.53 |